Hydrogen storage capacity of the Ti-Pd multilayer systems

STEVEN MOTHIBAKGOMO
MAGOGODI

A thesis submitted in partial fulfilment of the requirements for the degree of Magister Scientiae.

UNIVERSITY OF THE WESTERN CAPE

&

iThemba LABS

Supervisors: **Dr Sylvain Halindintwali**

University of the Western Cape

Physics Department

Dr Christopher Mtshali

Material Research Division

iThemba LABS

August 2019

Declaration

Student Number: 3698184

I declare that **Hydrogen storage capacity of the Ti-Pd multilayer systems** is my work and that all sources that I have used or quoted have been indicated and acknowledged by means of complete references.

Signature:  **Date:** 19/08/2019

Steven Mothibakgomo Magogodi

Abstract

Hydrogen has high energy density and it is regarded as the future energy carrier. Hydrogen can be stored as a gas in high-pressure cylinders, as a liquid in cryogenic tanks and as a solid in metal hydrides. The storage of hydrogen in gas and liquid form has many limitations. Light metal hydrides show high energy density and are a promising and more practical mode of hydrogen storage. In particular, titanium and its alloys are promising metal hydrides for hydrogen storage due to their high affinity to hydrogen. The aim of this study is to investigate the effect of thermal annealing on hydrogen storage capacity of Ti-Pd multilayer systems. Ti-Pd multilayer films were prepared on CP-Ti (commercial pure Ti) and Ti6Al4V substrates using an electron beam evaporator equipped with a thickness monitor. The sequential deposition of layers Pd(50nm)/Ti(25nm)/Pd(50nm) was done at a constant deposition rate of 0.6 Å/s. The first batch of samples were thermally annealed at 550 °C in vacuum for two hours, the second batch of samples were annealed at 550 ^{o}C under H_2(15%)/Ar(85%) gas mixture for two hours and the third series of samples was annealed under pure H_2 gas at 550 ^{o}C for one hour. SEM showed relatively homogeneous and smooth topography of surfaces in as-deposited samples, while a rough textured surface was observed in both samples annealed under vacuum and under H_2/Ar gas mixture. The samples annealed under pure H_2 gas did not show any sign of crystallites grow but instead a relatively smooth surface with sign of etching. XRD revealed structural transformation as evidenced by the presence of $PdTi_2$ phase in samples annealed under vacuum; in samples annealed under the gas mixture Pd_2Ti was noted in addition to TiH_2 and TiO_2. While the TiH_2 phase is an indication of hydrogen absorption, the $TiPd_2$ phase suggests intermixing of the deposited layers and the presence of TiO_2 is evidence of oxidation. The samples annealed under pure H_2 gas showed only TiH_2 with no trace of structural transformation. RBS confirmed the intermixing of layers in the samples annealed under vacuum and H_2(15%)/Ar(85%) gas mixture, while samples annealed under pure H_2 gas did not show any intermixing of layers. ERDA revealed an average H content of ~ 3.5 at.% in CP-Ti and ~6.2 at.% in Ti6Al4V for samples annealed under H_2(15%)/Ar(85%) gas mixture. We recorded an hydrogen content of ~19.5 at.% in CP-Ti annealed under pure H_2 while ~25.5 at.% was found in Ti6Al4V annealed under the same conditions. When the thickness of the Pd catalyst layers was increased to 100 nm (i.e. Pd (100 nm)/Ti (25 nm)/Pd (100 nm)), only ~ 12.5 at.% and 11.2 at. % hydrogen content was recorded in samples prepared on CP-Ti and Ti6Al4V alloy respectively, both annealed under pure hydrogen for one hour as above.

Dedications

This work is dedicated to the following people:

My brother my hero Monamodi Magogodi, my aunt Sading Magogodi, my sister Portia Magogodi, my late grandmother Ditlhoriso Magogodi and lastly my late grandfather Setumo Steven Mothibakgomo Magogodi.

Acknowledgements

Ke rata go leboga Modimo le Badimo bo Magogodi ka go mpha maatla, bo pelotelele le kgotlhelelo gore kebo ke kgonne go konosetsa porojêkê eno.

This project have involved many people and it would not be possible without their help, I therefore would like to thank them for their contributions:

My former supervisor Dr Miroslava Topić (iThemba LABS) for granting me such great project, and for her guidance during the time we were working together.

My supervisor Dr Sylvain Halindintwali (UWC) for his suggestions, critical comments and patient guidance in thesis writings.

Dr Christopher Mtshali (iThemba LABS) for his supervision which taught me a lot in this project. The guidance on material preparations, analysis more especially the knowledge of Ion Beam Analysis from experiments to simulations. Writing guidance and correction as well as motivations for strength support.

My writing coaches from UWC, Mr Moses MAGOBA and Mr Alechine Ameh.

Mr Michael Adams (iThemba LABS) for always helping me with cutting of the materials.

Centre for Material Engineering at University of the Cape Town for allowing me to do grinding and polishing of the materials as well as the hydrogenation at their facility.

Materials Research Department (iThemba LABS) stuff and students for their help, courage, support and the laughter we all had throughout the journey.

Dr Remy Bucher (iThemba LABS) for his assistance with XRD technique.

Dr Nametso Mongwaketsi, Karen Cloete and Zakhele Khumalo (iThemba LABS) for their assistance with Ion Beam Analysis.

Mr Lindsey Davids (iThemba LABS) for always assisting with the transport when I was performing experiments at UWC and UCT.

Fellow students from Manus/Matsci for sharing their advice and experiences with me for the way forward on some obstacles.

Mr Earl Mc Donald (UWC) for assisting me with the Scanning Electron Microscopy technique.

Prof Christopher Arendse (Head of Department at physics Department UWC) for allowing us to perform hydrogenation experiments at his facility, and thank Mr Siphelo Ngqoloda for helping with the experiments.

Dr Mlungisi Nkosi (Head of Department at MRD iThemba LABS) for assisting with purchasing of the materials and top-up funding from iThemba LABS.

Ke rata go leboga ba gae-gaecho. Ke simolola ka mogolole Monamodi ka tshegetso yotlhe ye a mphileng yone go hitlha le motsi wa gompieno. Ke leboge gape bo rakgadi ka lerato le kemonokeng ye ba kileng bampha yone mo nakong tse dithata. Ke leboge bo kgaitsadiake, bo nkgonne, bo rrangwane, le ditsala tsame ka tshegetso le kgothatso e ba nnetseng yone ga bane bare “gotla siama tshwara ka thata”. Ke lebogela le lerato, thotloetso le kemonokeng yaga Nokuthula Chachi.

Ke heleletsa ka go leboga batsadi bame ka go nnela chono ya botshelo, ntle le bone diphitlhelelo tseno di kabo di seyo, Rre Moncho Magogodi ke leboga go menagane.

I will like to thank National Research Funding for their financial support on this project, and also Tandetron accelerator group at iThemba LABS Material Research Department for hydrogen storage analysis.

Abbreviations

Ti: Titanium

Pd: Palladium

Al: Aluminium

V: Vanadium

H: Hydrogen

SEM: Scanning Electron Microscopy

XRD: X-ray diffraction

RBS: Rutherford Backscattering Spectroscopy

ERDA: Elastic Recoil Detection Analysis

SCCM: Standard Cubic Centimetres per Minute

PEM: Proton Exchange Membrane

CO_2: Carbon dioxide

Keywords

Titanium

Ti6Al4V alloy

Electron beam evaporation

Thin film coatings

Multilayers

Palladium-Titanium

Hydrogenation

Hydrogen storage

Elastic Recoil Detection Analysis

Scanning Electron Microscopy

Rutherford Backscattering Spectroscopy

Phase transformation

List of Figures

List of Tables

Table of Contents

CHAPTER ONE

Introduction

1.1 Background

The need for energy provision is steeply rising with the high rate of human population growth. Human population has been on the rise since the beginning of the 20th century. According to the United Nations Population Fund [1.1, 1.2], the human population has increased from 1.6 billion in 1900 to 2.5 billion in 1950; 6.1 billion in 2000 and 7.0 billion in 2011. It is estimated to reach 9.5 billion by 2050. As human population grows fast, consumption of energy also increases at a rapid rate in order to meet basic and developmental needs in electricity as well as in other fuels required for transportation, cooking, powering of industries, residential and commercial sectors. According to the International Energy Outlook 2017, the world energy consumption rose from 124,848275 GWh in 2004 to an estimated 215,700317 GWh in 2040 [1.3], i.e. almost double the rate of consumption in less than 40 years. The global energy supply comes from different sources such as fossil fuels, nuclear and renewable energy; in 2015 fossil fuels accounted for 86.7%, nuclear energy for 4.4% and renewable energy for 8.9% [1.4]. Fossil fuels such as coal, oil and natural gas are able to meet today's global energy demand [1.5] but they are non-renewable and are being depleted at a fast rate due to exponential increase of energy demand globally. Moreover, they are not eco-friendly because they are major contributors to greenhouse gases. Since 1971, emission of carbon dioxide gas (CO_2) from combustion of fossil fuel has been on the rise and was approximated to be 30 billion tons per year in 2008 [1.6]. Other part of energy supply is sourced from nuclear energy sources by means of nuclear fission [1.7]. When a larger nucleus of an atom is bombarded with a neutron it gets unstable and split into smaller nuclei and release energy in form of heat which can be used for electricity generation [1.8]. Even

though nuclear energy is not renewable, it is a clean source of power. It does not produce any CO_2 emission but radioactive nuclear wastes are produced. The wastes produced from this method is highly radioactive and can cause cancer, genetic disorder and lead to death, if not well handled and well-disposed [1.9]. Thus highly proper handling and waste disposal is needed for radioactive waste. Above the occupational safety and waste disposal issues that are source of public resentment towards this technology [1.10], another challenge of nuclear energy source is that the fuel is not inexhaustible.

Therefore, there is a need for alternative source of energy which do not face depletion, have zero emission of greenhouse gasses and also that do not produce any traces of radioactive waste. Renewable sources of energy such as solar, wind, water and hydrogen are alternatives for sustainable and clean energy supply that can meet global energy demand. Research on development of efficient, clean and renewable energy sources as a substitute to fossil fuels has thus intensified [1.11]. Hydrogen has been viewed widely as an alternative energy source and it is considered to be an ideal energy carrier due to the fact that: (a) this element is abundant in the universe, (b) it is light weight (c) has high energy density per unit mass, (d) its combustion does not produce any trace or residue that would be harmful to the environment as the by-products are only energy and water. On top of the above, hydrogen is abundant and it is renewable. This study fits in the big scheme of hydrogen economy.

1.2 Renewable hydrogen cycle

The existence of molecular hydrogen (H_2) is not found in nature as a free form; it has to be produced from other hydride compounds such as natural gas and water. Most of hydrogen used today is produced from fossil fuel such as natural gas, by a process known as steam methane reforming [1.12, 1.13]. This process account to the production of 96% hydrogen

currently used [1.14]. However, the disadvantage of this process is that it produces CO_2 greenhouse gas as a by-product [1.15]. Clean method of producing hydrogen is by electrolysis of water as shown in figure 1.1 [1.16].

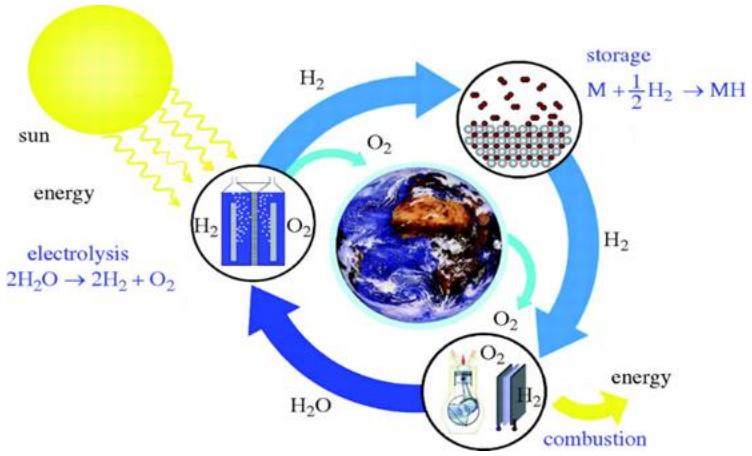

Figure 1.1: *Schematic of hydrogen cycle*

This process involves the use of a secondary energy source such as wind or the sun in order to split water molecules into two constituent elements of hydrogen and oxygen by means of electrolysis of water [1.17]. Hydrogen gas from the electrolysis can then be captured, stored and combusted in fuel cell to produce electrical energy and water as a by-product as in the typical schematic shown in figure 1.1, where solar energy is used.

1.3 The use of hydrogen as a fuel

Hydrogen is an energy carrier with more energy density than fossil fuel and its combustion process produces about 120 MJ/kg which is roughly three times to that of gasoline [1.18, 1.19]. Figure 1.2 shows a schematic of the working principle of a fuel cell which is basically made of three active parts sandwiched together; an anode electrode where the H_2 is split, the

cathode electrode where the oxygen gas is admitted and the proton exchange membrane (PEM).

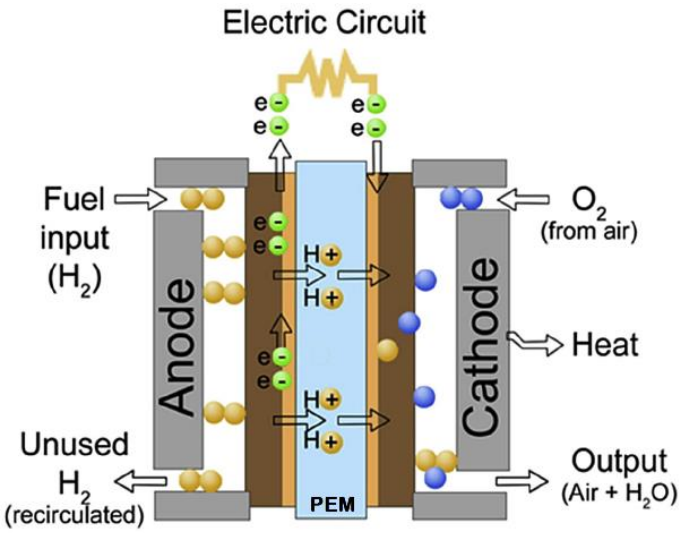

Figure 1.2: *Schematic of a PEM fuel cell [1.20].*

Molecular hydrogen is channelled to the anode side from its storage source, where it dissociates into positive ions (protons) and negatively charged electrons by a catalyst e.g. Platinum [1.21, 1.22]. PEM allows only the protons to pass through to the cathode while electrons are forced through an external circuit to the cathode thus producing electrical energy. At the cathode side, the protons from the PEM membranes recombine with the electrons arriving from the external circuit to form hydrogen that combine with the admitted oxygen to produce water and heat. Equations 1.1 to 1.3 summarise reactions occurring in the respective components of a PEM fuel cell.

Anode: oxidation reaction of hydrogen, $2\mathrm{H}_{2\,(\mathrm{g})} \rightarrow 4\mathrm{H}^{+}{}_{(aq)} + 4\mathrm{e}^{-}$ 1.1

Cathode: reduction reaction of oxygen, $\mathrm{O}_{2(\mathrm{g})} + 4\mathrm{H}^{+}{}_{(aq)} + 4\mathrm{e}^{-} \rightarrow \mathrm{H}_2\mathrm{O}_{(l)}$ 1.2

Overall reaction of hydrogen and oxygen in a Proton Exchange Membrane Fuel Cell

$$2\mathrm{H}_{2(\mathrm{g})} + \mathrm{O}_{2(\mathrm{g})} \rightarrow 2\mathrm{H}_2\mathrm{O}_{(l)} + electric\ energy + heat \qquad 1.3$$

1.4 Energy density and storage of hydrogen fuel

At standard pressure and room temperature, hydrogen exists in a gas phase and it is characterized by a low volumetric energy density. Therefore, in order to improve the energy density, storage materials and mechanisms to store large amount of hydrogen are required. Hydrogen can be stored as a compressed gas in a high pressure tank or as a liquid at a cryogenic temperature or as a hydride within the solid metals. The gas and liquid methods involve challenging and complex technologies.

Hydrogen can be found in the three states of matter: gas, liquid and solid. Figure 1.3 shows the pressure –temperature phase diagram of hydrogen [1.23]. From figure 1.3 hydrogen is found to be a solid at a temperature of -262 ^{o}C with a density of 70.6 kg/m^3 and to be a gas at a temperature of 0 ^{o}C and pressure of 1 bar with a density of 0.09 kg/m^3. Moreover, in the region ranging from the triple point to critical point, hydrogen at a temperature of -253 ^{o}C is found in the liquid state with a density of 70.8 kg/m^3 [1.23].

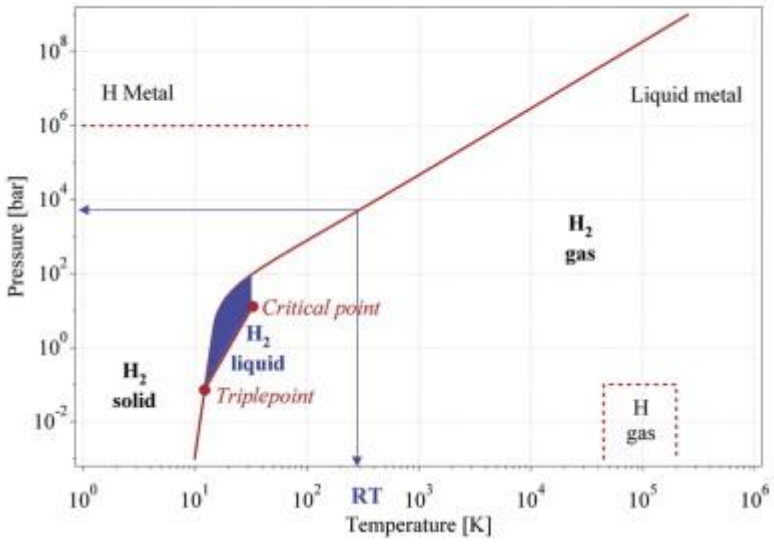

Figure 1.3: *Pressure – Temperature phase diagram of hydrogen [1.23].*

Current industrial storage methods for hydrogen are in as- compressed gas and in as- cryogenic liquid forms [1.24]. These storage methods have respective challenges and limitations [1.25]. These storage methods require the application of very high pressure for compressed gas or very low temperature for cryogenic liquid as can be seen on table 1.1. Hydrogen stored in solid metals is normally referred to as metal hydrides [1.26]; Table 1.1 shows that metal hydride method can store at RT / standard pressure, large amount of hydrogen per volume when compared to the other two storage methods.

Table 1.1: *Storage conditions and hydrogen density in three phases of matter [1.23].*

Storage method	**Volumetric density [kg H_2 / m^3]**	**Gravimetric density [weight %]**	**Temperature [^oC]**	**Pressure [bar]**
High pressure gas cylinder	<40	13	RT	800
Liquid hydrogen	70.8	Size dependent	−252	1
Metal hydrides	150	≈ 2	RT	1

1.4.1 High pressure hydrogen storage

Storing hydrogen as a gas is the most common and simple storage system which is currently used. With this method hydrogen is stored in a high pressure gas cylinder, generally at 200 bar. The pressure can however be increased to a maximum of 800 bar in the lightweight composite cylinders [1.23]. For instance, with 700 bar tank, 26.3 kg/m^3 can be achieved with a gravimetric density of 4.6 wt. % [1.27]. The increase of pressure enables the reduction of the tank volume by approximately 33 %, but high pressurized gas is a safety risk and higher

compression energy will be needed [1.28]. Even at this high pressure of 700 bar, the volumetric density still remains very low compared to those of other storage methods.

1.4.2 Hydrogen storage in liquid form

At standard pressure, hydrogen liquefies at a temperature of -253 ^{o}C, with the volumetric density of 70.8 kg/m^3. Liquid hydrogen is stored in a cryogenic tank to keep hydrogen below boiling point. Storing hydrogen as a liquid results in higher energy density than that achieved in gas storage systems. The requirements of cryogenic systems for H_2 storage in liquid phase makes this method expensive [1.29]. The heat input from the surroundings into the cryogenic tank lead to evaporation of hydrogen known as boiling off phenomenon [1.30, 1.31]. Typically a 100 m^3 storage tank experiences evaporation of 0.2% per day [1.23]. Hydrogen boils-off easily and most of it is lost during refuelling and transportation. Furthermore, about 30 to 35% of energy is used for liquefaction of hydrogen from compressed gas [1.27]. The energy cost in liquefaction and the loss in energy during boiling-off of liquid hydrogen are limiting factors of this mode of storage.

1.4.3 Hydrogen storage in metals

Hydrogen is a very reactive element which can react with most metals and their alloys to form metal hydrides [1.32]. During this storage process, hydrogen diffuses into the interstitial sites of a metal and/ or passivates dangling bonds in the metal. This type of storage system received attention since Thomas Graham [1.33] observed hydrogen diffusion into palladium, while studying diffusion of gases. Ever since, several metals have been researched for hydrogen storage. Table 1.2 gives examples of metals that have been used; their volumetric densities are compared to those H_2 in gas and liquid forms.

Table 1.2: *Volumetric and gravimetric content of hydrogen in gas and liquid phases along in metal hydrides [1.34].*

Storage system	Number of hydrogen atoms per $\mathbf{cm^3}(\times \mathbf{10^{22}})$	Hydrogen Wt. %
$\mathbf{H_2}$ gas (200 bar)	0.99	100
$\mathbf{H_2}$ liquid ($\mathbf{-253\ ^oC}$)	4.2	100
$\mathbf{H_2}$ solid ($\mathbf{-269\ ^oC}$)	5.3	100
$\mathbf{MgH_2}$	6.5	7.6
$\mathbf{Mg_2NiH_4}$	5.9	3.6
$\mathbf{FeTiH_{1.95}}$	6.0	1.89
$\mathbf{LaNi_5H_{6.7}}$	5.5	1.37
$\mathbf{ZrMn_2H_{3.6}}$	6.0	1.75
$\mathbf{VH_2}$	11.4	2.10

Hydrogen is mostly reactive to electropositive elements such as lanthanide, actinides and members of the titanium and vanadium group; these elements react with hydrogen to form hydrides. Metal hydrides are classified into binary and intermetallic hydrides. Binary metal hydrides consist of one metal and an addition of hydrogen and it can be described by equation 1.4, where M represents metal, H represents hydrogen and x, is an integer number. MH_x the formed hydride and Q, the heat exchanged during the process of hydride formation. TiH_2 and MgH_2 are examples of binary hydride.

$$M_{(s)} + \frac{x}{2} H_{2(g)} \rightarrow MH_{x(s)} + Q \qquad 1.4$$

Intermetallic hydrides are hydrides consisting of two or more metals and are described by equation 1.5, where A and B represent the metals, x, m, n are integer numbers and Q the heat during hydride formation. Examples of intermetallic compounds are AB_5 in $CaCu_5$ structure, AB_2 $in\ MoSi_2$ structure and AB in $CsCl$ structure. The metal labelled A has a stronger affinity for hydrogen and it is the one forming stable hydrides, while the ones labelled B form only unstable hydrides [1.34]. Several intermetallic hydrides of interest, for hydrogen storage, are listed in table 1.3.

$$A_m B_{n\,(s)} + \frac{x}{2} H_{2\,(g)} \rightarrow A_m B_n H_{x\,(s)} + Q \qquad 1.5$$

Table 1.3: *Intermetallic compounds with their hydride formation [1.24].*

Intermetallic compound	**Prototype**	**Hydride**
$\boldsymbol{AB_5}$	$LaNi_5$	$LaNi_5H_6$
$\boldsymbol{AB_2}$	$ZrV_2, ZrMn_2, TiMn_2$	$ZrV_2H_{5.5}$
$\boldsymbol{AB_3}$	$CeNi_3, YFe_3$	$CeNi_3H_4$
$\boldsymbol{A_2B_7}$	Y_2Ni_7, Th_2Fe_7	$Y_2Ni_7H_3$
$\boldsymbol{A_6B_{23}}$	Y_6Fe_{23}	$Y_6Fe_{23}H_{12}$
$\boldsymbol{AB}$	$TiFe, ZrNi$	$TiFe_2$
$\boldsymbol{A_2B}$	Mg_2Ni, Ti_2Ni	Mg_2NiH_4

When compared to other storage methods, metal hydrides have higher hydrogen storage density. For example, MgH_2 has 6.5 x 10^{22} hydrogen atoms/cm^3 as compared to gas and liquid with 0.99 x 10^{22} and 4.2 x 10^{22} atoms/cm^3 respectively. Furthermore, liquid hydrogen has a volumetric hydrogen density of 70.8 kg/m^3 while intermetallic hydride such as

Mg_2FeH_6 shows a higher volumetric hydrogen density of 150 kg/m^3, which is twice that of liquid hydrogen as shown in figure 1.4.

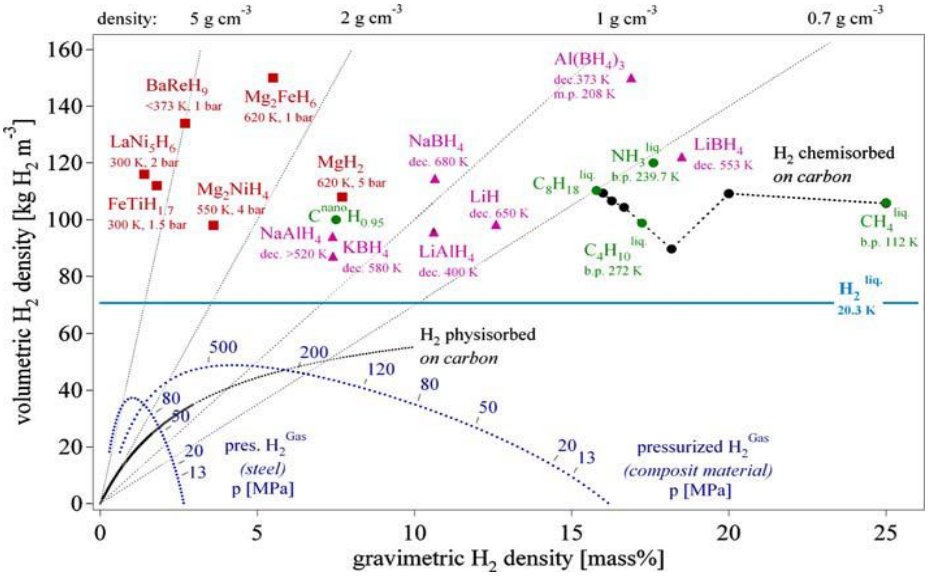

Figure 1.4: *Volumetric and gravimetric hydrogen density of selective hydrides [1.16].*

Hydrogen can be stored as gas in high pressure cylinders, liquid in cryogenic tanks and as a solid in metal hydrides. In the gas form it requires high pressure and it has low storage capacity [1.27, 1.28]. In liquid phase, it has more storage capacity but it requires cryogenic temperatures and it suffers from hydrogen boiling-off [1.30]. Also the maintenance of this system it is expensive [1.29]. Metal hydride storage system is efficient in storing high volume of hydrogen, and it is safe since the storage can be done at a standard pressure and room temperature [1.34]. However, the slow kinetics of hydrogen adsorption and desorption is a drawback in metal hydride storage. Advanced materials such as palladium coated metals are used in this investigation for possible hydrogen adsorption and desorption enhancement since palladium serves as an adsorption catalyst and improves the kinetics of hydrogen into metal interstitials.

1.5 Aims and outline of this thesis

The purpose of this study is to investigate the effect of thermal annealing on hydrogen storage capacity of the Ti-Pd multilayer systems. Ti/Pd multilayer thin films were deposited on bulk material of commercially pure titanium (CP-Ti) and Ti6Al4V-alloy and subsequently thermally annealed under vacuum, in Ar diluted hydrogen gas mixture and in pure hydrogen atmospheres. The samples were characterized by SEM in order to study the surface morphological changes, XRD for phase transformation, RBS for stoichiometry and structural change and ERDA for hydrogen profile and storage capacity. This thesis is arranged into four chapters. The background, motivation of the study and hydrogen storage technologies are given in chapter one. Chapter two discusses the fundamentals of hydrogenation in metals, the required activation temperature for hydrogenation in Ti-Pd system and the effect of annealing in various atmospheres on the Ti-Pd system. Chapter three describes the material and preparations of the samples used in this investigation. It also discusses the theoretical background on the analytical techniques as well as the measurement conditions and data collection. The results obtained from the investigations are presented and discussed in chapter four. Lastly, summary and conclusion, and future work are given at the end of this study.

1.6 References

[1.1] United Nations (UN). Overall Total World Population 1950 – 2050; (2009).

[1.2] UN World Population Prospects– The 2012 Revision Population Database; (2012).

[1.3] Energy, U.S., International Energy Outlook 2017 Overview. Int. Energy Outlook, vol. IEO2017, 143, (2017).

[1.4] P. Moriarty, S. J. Wang, Assessing global renewable energy forecasts, *Energy Procedia*, 75, 2523-2528, (2015).

[1.5] N. Abas, A. Kalair, N. Khan, Review of fossil fuels and future energy technologies, *Futures*, 69, 31-49, (2015).

[1.6] M. Hook, X. Tang, Depletion of fossil fuels and anthropogenic climate change, *A review Energy Policy*, 52, 797 – 809, (2003).

[1.7] W. C. Patterson, *Nuclear power*, Penguin, (1976).

[1.8] N. B. Power, Electricity Generation: *Nuclear Fission*, (2014).

[1.9] S. J. Adelstein, Radiation risk in nuclear medicine. *Seminars in nuclear medicine*, 44 (3), 187-192, (2014).

[1.10] H. Zhu, Y. Deng, R. Zhu, X. He, Fear of nuclear power? Evidence from Fukushima nuclear accident and land markets in China, *Regional Science and Urban Economics*, 60, 139-154, (2016).

[1.11] B.D. Solomon, A. Banerjee, A global survey of hydrogen energy research, development and policy, *Energy policy*, 34 (7), 781-792 (2006).

[1.12] D.A. Celzard, V. Fierro, E. Martin, F. Broust, A. Zoulalian, Catalytic decomposition of methane over a wood char concurrently activated by a pyrolysis gas, *Applied Catalysis A; General*, 346, 164-173, (2008).

[1.13] Y. Li, D. Li, G. Wang, Methane decomposition to CO_x-free hydrogen and Nano-carbon material on group 8–10 base metal catalysts: *A review Catalysis Today*, 162, 1-48, (2011).

[1.14] C. Gillan, M. Fowles, S. French, S.D. Jackson, Ethane steam reforming over a platinum/alumina catalyst: effect of sulfur poisoning, *Industrial & Engineering Chemistry Research*, 52, 13350-13356, (2013).

[1.15] J. Yoo, S. Park, J. H. Song, S. Yoo, I. K. Song, Hydrogen production by steam reforming of natural gas over butyric acid-assisted Nickle/alumina catalyst, *Internation journal of hydrogen Energy*, 42 (47), 28377 - 28385, (2017).

[1.16] A. Züttel, A. Remhof, A. Borgschulte, O. Friedrichs, Hydrogen: the future energy carrier, 368, 3329-3342, (2010).

[1.17] J. Chi, H. Yu, Water electrolysis based on renewable energy for hydrogen production. *Chinese Journal of Catalysis*, 39 (3), 390-394, (2018).

[1.18] T. Abbasi, S.A. Abbasi, Renewable hydrogen: Prospects and Challenges, *Renewable and Sustainable Energy Reviews*, 12, 3034 - 3040, (2011).

[1.19] G. Thomas, Overview of storage development DOE hydrogen program, *Sandia National Laboratories*, 9, (2000).

[1.20] A. Harrag, S. Messalti, How fuzzy logic can improve PEM fuel cell MPPT performances? *International journal of hydrogen energy*, 43 (1), 537 - 550, (2018).

[1.21] O.Z. Sharaf, M.F. Orhan, An overview of fuel cell technology: Fundamentals and applications, *Renewable Sustainable Energy Reviews*, 32, 810-853, (2014).

[1.22] O.T. Holton, J.W. Stevenson, The role of platinum in proton exchange membrane fuel cells, *Platinum Metals Review*, 57 (4), 259-271, (2013).

[1.23] A. Zuttel, Hydrogen storage and distribution systems, Mitigation and Adaptation Strategies for Global Change, 12, 243- 365, (2007).

[1.24] M. Reuß, T. Grube, M. Robinius, P. Preuster, P. Wasserscheid, D. Stolten, Seasonal storage and alternative carriers: A flexible hydrogen supply chain model, *Applied Energy*, 200, 290-302, (2017).

[1.25] S. Singh, S. Jain, P.S. Venkateswaran, A.K. Tiwari, M.R. Nouni, J.K. Pandey, S. Goel, Hydrogen: a sustainable fuel for future of the transport sector, *Renewable and Sustainable Energy Reviews*, 51, 623-633, (2015).

[1.26] B. Sakintuna, F. Lamari-Darkrim, M. Hirscher, Metal hydride materials for solid hydrogen storage: a review, *International journal of hydrogen energy*, 32 (9), 1121-1140, (2007).

[1.27] F. Zhang, P. Zhao, M. Niu, J. Maddy, The survey of key technologies in hydrogen energy storage, *International journal of hydrogen energy*, 41, 14535-14552, (2016).

[1.28] T.H. Motyka, W.A. Summers, R. Zidan,. Hydrogen storage: the key challenge facing a hydrogen economy. *United States Department of Energy*, (2004).

[1.29] M. Pudukudy, Z. Yaakob, M. Mohammadb, B. Narayanan, K. Sopian, Renewable hydrogen economy in Asia – opportunities and challenges: an overview, *Renew Sustain Energy Review*, 30, 743-757, (2014).

[1.30] H.T. Hwang, A. Varma, Hydrogen storage for fuel cell vehicles, Current Opinion Chemical Engineering, 5, 42-48, (2014).

[1.31] R.O. Stroman, M.W. Schuette, K. Swider-Lyons, J.A. Rodgers, D.J. Edwards, Liquid hydrogen fuel system design and demonstration in a small long endurance air vehicle. *International journal of hydrogen energy*, 39 (21), 11279-11290, (2014).

[1.32] N.A.A. Rusman, M. Dahari, A review on the current progress of metal hydrides material for solid-state hydrogen storage applications, *International Journal of Hydrogen Energy*, 41 (28), 12108-12126, (2016).

[1.33] J. Wisniak, Thomas Graham. II, Contributions to diffusion of gases and liquids, colloids, dialysis, and osmosis, Edu. Quim, 24, 506-515, (2013).

[1.34] I.P. Jain, C. Lal, A. Jian. Hydrogen storage in Mg: A most promising material, *International Journal of Hydrogen Energy*, 35, 5133-5144, (2010).

CHAPTER TWO

Literature review

2.1 Hydrogen interaction with the metal

Hydrogen is a very reactive element that reacts with most metals to form metal hydrides [2.1]. Formation of metal hydrides take place under processes such as physical absorption (physisorption) and chemical absorption (chemisorption) to allow the diffusion of hydrogen into the metal.

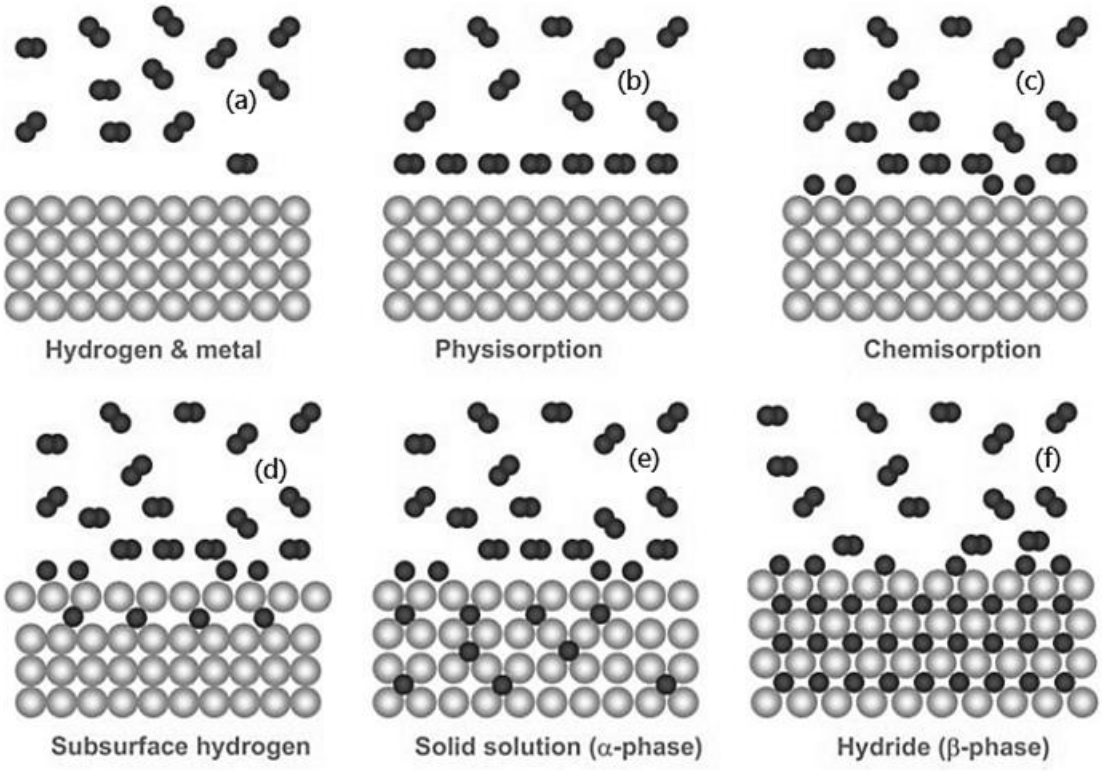

Figure 2.1: *Schematic representation of; (a) hydrogen adsorption on metal, (b) physisorption, (c) chemisorption, (d) subsurface hydrogen, (e) solid solution, (f) metal hydride [2.2].*

Figure 2.1 presents the diffusion chart of hydrogen into the metal. In the initial stage molecular hydrogen in gas phase approaches the metal surface (figure 2.1(a)); it has however to overcome the surface potential of the metal in order to be adsorbed through the

physisorption process (figure 2.1 (b)); this is followed by the chemisorption process (figure 2.1(c)) where molecular hydrogen (H_2) dissociates into atomic hydrogen (H). The H then diffuses into available sites in the subsurface (figure 2.1 (d)) and subsequently into the bulk through interstitial sites of the host-metal lattice (figure 2.1 (e)). This process happens exothermically as H is losing energy to the lattice. For low H absorption concentration where the hydrogen to metal ratio is small (H/M <0.1) [2.3], H is dissolved in a solid solution; this is α-phase. Further increase in H concentration, the interaction between H-H atoms is significant and more energy is deposited into the lattice that expands. When the expansion becomes important (H/M >0.1), a new phase nucleates and grows into metal hydride (figure 2.1 (f)), also known as β-phase [2.3, 2.4]. For instance in Nb hydride (NbH), the dissolution of H leads to an expansion window of 2 – 3 $Å^3$ per one H atom (from an initial atomic volume of 18 $Å^3$ to 20 - 21 $Å^3$ respectively) where α and β phases coexist. Higher H absorption resulting in NbH_2 e.g. a new phase (δ) is formed [2.4]. Fig. 2.2 [2.3 - 2.4] shows a schematic of the energy interaction at interface (H_2/Metal surface) during the physisorption and chemisorption processes.

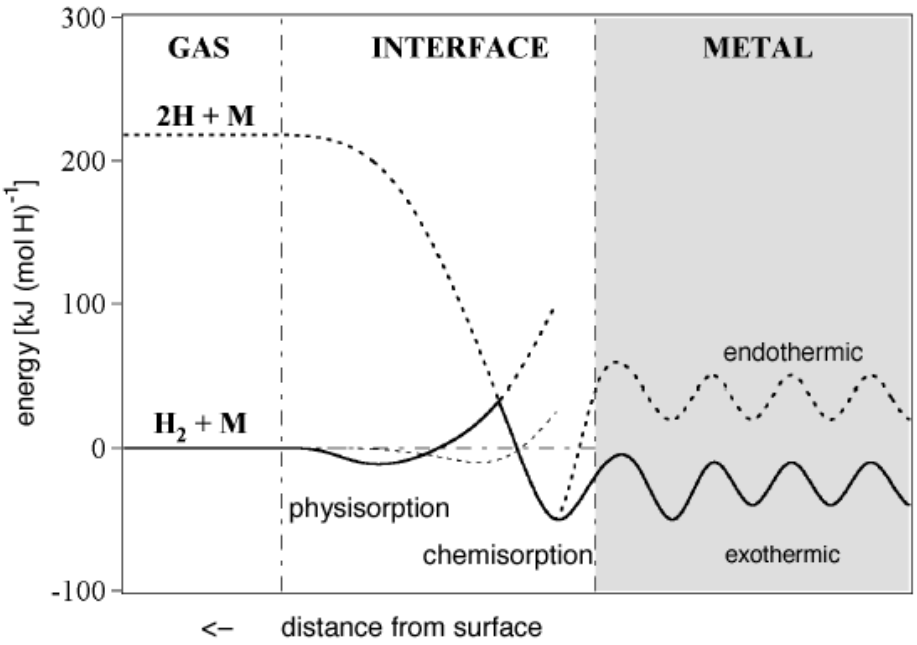

Figure 2.2: *One dimensional potential energy curve showing hydrogen absorption process [2.3, 2.4].*

2.2 Hydrogen interaction with pure titanium and Ti6Al4V alloy.

2.2.1 Physical and chemical properties of Ti and Ti6Al4V

Titanium is a group four transition metal with atomic number 22, molar mass of 47.87 g/mol and density of 4.51 g/cm^3. It has a hexagonal close packed (hcp) crystal structure, α phase at room temperature. The α-phase has most dense basal (0001), pyramidal $(10\bar{1}1)$ and prismatic $(10\bar{1}0)$ planes as shown in figure 2.3 (a). At a higher temperature of about 882 °C, it goes under an allotropic transformation into β-phase of body centered cubic (bcc) structure with lattice parameter $a = 0.332$ nm as shown in figure 2.3 (b). Ti6Al4V is a titanium alloyed with 6 wt.% of aluminium and 4 wt.% of vanadium and has two stable phases (α+β) at room temperature.

Titanium and its alloys (Ti6Al4V) find application in aerospace, marine, medicine due to their corrosion resistance and high strength to weight ratio [2.5, 2.6, and 2.7]. Lately they have also gained more attention in the field of hydrogen storage owing to their relatively high affinity to hydrogen [2.8, 2.9] and their ability to absorb and desorb hydrogen in a large quantity [2.10].

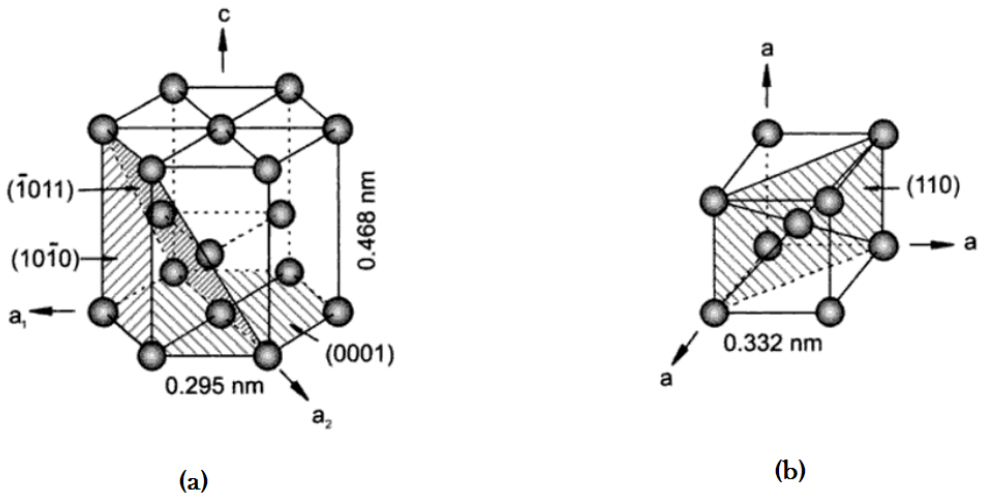

Figure 2.3: *Titanium crystal structure (a) the hcp, α-phase and (b) the bcc, β-phase [2.11].*

2.2.2 Ti-H and Ti6Al4V-H phase transformations

When hydrogen interacts with Ti at an elevated temperature, phase transformation starts to occur depending on absorbed hydrogen concentration as shown in the Ti-H phase diagram in figure. 2.4. At a low hydrogen concentration, individual hydrogen atoms prefer the octahedral sites in the α-phase and tetrahedral sites in the β-phase to form a solid solution. At high concentration, the formation of titanium hydride starts to occur.

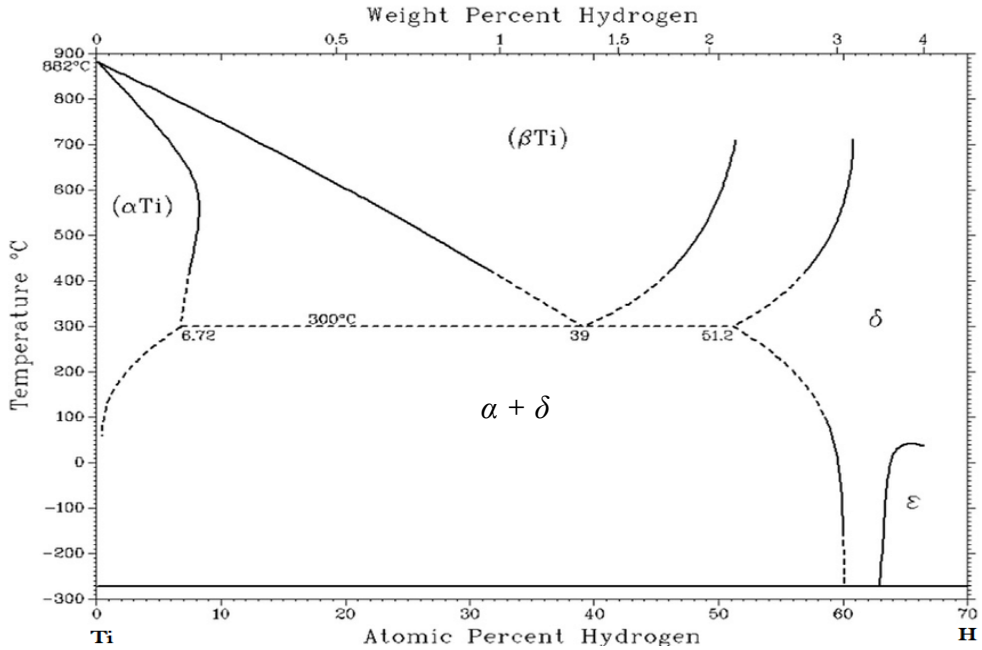

Figure 2.4: *Phase diagram of Ti-H system (at P = 0.1MPa) [2.12].*

According to the Ti-H phase diagram on figure 2.4, the α-phase at room temperature has the hydrogen solubility of 0.12 at.% and can accommodate up to 7 at.% below 600 ^{o}C [2.13-2.15]. At a temperature above 600 ^{o}C hydrogen solubility in α-phase decreases drastically up to 882 ^{o}C and hydrogen start to act as a β-stabilizing element reducing temperature from 882 ^{o}C to the eutectoid temperature of 300 ^{o}C. At the eutectoid temperature with hydrogen concentrations of 6.72, 39 and 51.9 at.% exist the phases of α-Ti, β-Ti and δ-TiH_2 respectively.

Three kinds of titanium hydrides phases (γ, δ, ε) have been observed at room temperature, corresponding to the available amount of hydrogen. At low hydrogen concentration range between 1-3 at.% the γ-TiH phase with fct precipitates in the α-Ti solid solution. The δ-TiHx (where x exist over a wide range of 1.5 -1.99) phase with fcc lattice exist at a hydrogen concentration of about 60 at.% [2.9]. The δ-hydride can also exist as a mixture in β+δ phase at a concentration between 39-51.2 ^{o}C at eutectoid temperature and below that exist in α+δ phase. When the absorbed amount of hydrogen is over 60 at.% the ε-TiH_2 with bct structure exist.

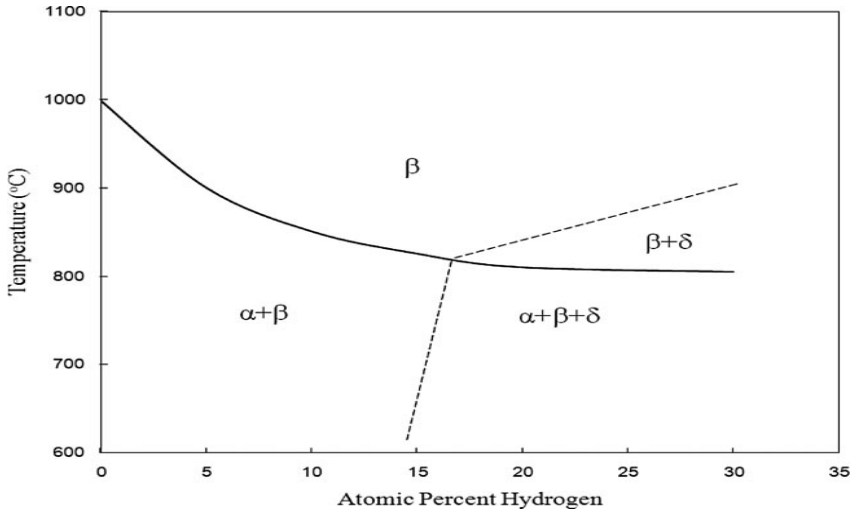

Figure 2.5: *Phase diagram of Ti6Al4V-Hydrogen system [2.17].*

Formation of hydride in Ti6Al4V was reported to exist at hydrogen concentration more than 15 at.% with temperature up to 800 ^{o}C [2.16, 2.57]. the effect of hydrogen on Ti6Al4V was also reported to be β stabilizing element, when hydrogen concentration is increased from 0 up to formation of hydrides it reduces β-transus temperature from 1000 to 800 ^{o}C [2.16, 2.17]. Figure 2.5 shows the Ti6Al4V – hydrogen phase diagram proposed by Qazi et al [2.17]. The diagram was in agreement with Kerr et al [2.16] showing that α+β+(δ) hydride exist at

hydrogen concentration above 15 at.% with temperature up to β-transus of 800 ^{o}C. Above β-transus temperature with more than 15 at. % the β+(δ) hydride was reported to exist [2.17].

2.2.3 Activation of hydrogen absorption on CP-Ti and Ti6Al4V

Titanium and its alloys are naturally covered with a thin oxide layer at room temperature which acts as a barrier for hydrogen diffusion on the surface [2.27]. Surface activation is thus an important aspect of hydrogenation in breaking down first this surface oxide layer; this can be achieved by hydrogenating the metal at elevated temperature. Absorption of hydrogen in titanium and Ti6Al4V alloy is influenced by varied factors such as hydrogenation temperature, pressure, flow rate and H_2 content in the gas mixture. Several authors have reported high volumetric quantity of absorbed hydrogen at the optimum temperature of 550 ^{o}C [2.18 - 2.25]. Lopez-Suarez et al [2.21] studied hydrogenation of Ti and Ti6Al4V alloy from 150-750 ^{o}C and reported activation temperature to be at 550 ^{o}C. Mazwi [2.23] investigated these materials at 450-650 ^{o}C, and detected no absorption at a temperature lower than 550 ^{o}C while above this temperature the hydrogen content decreased drastically. Baoguo et al [2.22] also reported that hydrogen concentration reaches its maximum absorption at 550 ^{o}C in Ti6Al4V, whereas below this temperature absorption was very low and decreases with increasing temperature. Topic et al. [2.24] hydrogenated Ti6Al4V and pure Ti at 550 ^{o}C using a gas mixture of 15 % hydrogen and 85 % argon and reported 31 at.% H and 41 at.% H absorption respectively. From the above reports, the optimum temperature for hydrogen absorption in CP-Ti and Ti6Al4V is thus found to be around 550 ^{o}C. At this temperature the passive oxide film is broken down creating a pathway for hydrogen to migrate through interstitials in the metals [2.26].

2.3 Titanium-noble metal system

Another way to avoid the built –up of the oxide layer, is to deposit a thin layer of a noble metal that is resistant to corrosion and oxidation on top of a cleaned, oxygen free Ti system. Palladium (Pd) would be a good candidate for such applications. Pd is one of the interesting material in the hydrogen economy as it is used in the variety of applications such as; hydrogen purification selective membranes, hydrogen sensors, hydrogen fuel cell electrode and catalyst for hydrogen absorption [2.47 -2.50]. Pd thin film has been extensively researched for their use as a catalyst in hydrogen absorption into Ti systems [2.51, 2.24]. It can easily absorb large volumetric quantity of hydrogen at room temperature and atmospheric pressure [2.28, 2.29], and also improve the mobility of the hydrogen into bulk titanium [2.48]. Ti-Pd system is proposed, in this study, as a route to both prevent oxidation of Ti and for improvement of hydrogen absorption in Ti systems. When Ti-Pd system is exposed to elevated temperature under hydrogen environment, it forms TiH_2 phase with possibly Ti-Pd intermetallic compounds. When Ti-Pd system is exposed to elevated temperature in vacuum, Ti and Pd interdiffusion is observed. Section 2.3.1 discusses the impact of thermal annealing of Ti-Pd layer stack in a hydrogen environment while possible intermetallic compounds are given in section 2.3.2.

2.3.1 Effect of thermal annealing Ti-Pd system in hydrogen environment

Several researchers have investigated and reported on the effect of Pd film on hydrogen absorption. For examples, Cabrera et al [2.53] reported that when titanium is exposed to hydrogen environment at room temperature there is no absorption of hydrogen, but noted a substantial amount of hydrogen absorption and diffusion into Ti lattice once coated by a layer of Pd. Mazwi [2.23] also reported hydrogen absorption in Ti6Al4V coated with thin film of

Pd at room temperature while no absorption was experienced in uncoated Ti6Al4V alloy. The amount of hydrogen absorbed at room temperature in titanium was however not enough to form hydrides [2.53, 2.23], therefore a higher temperature for activation energy of diffusion in the bulk is required. Hydrides in Ti-Pd system are found at a temperature range between 350-550 ^{o}C but more hydrogen absorption has been noted at 550 ^{o}C [2.23, 2.21]. Topic et al. [2.24] hydrogenated bulk Ti6Al4V alloy coated with 200 nm thin film of Pd, at 550 ^{o}C and they reported absorption of 36 at.% H, compared to the uncoated Ti6Al4V which absorbed 31 at. % H. The hydrogenation of Ti-Pd system proceeds in two phases of TiH_2 and TiPd compounds, the latter indicates interfacial intermixing as mentioned in the previous section.

Fujimoto et al. [2.54-2.56] investigated the structural stability of Ti-Pd multilayer systems upon annealing. In their investigation, 20 layers of Ti(10nm)/Pd(5nm), deposited onto Si substrate, were thermally annealed under pure hydrogen atmosphere and in vacuum for 24 hours at 350 ^{o}C. Upon annealing, in vacuum atomic interlayer mixing was observed, while under pure hydrogen environment no interlayer mixing was noted. Hydrogen in a form of TiH_2 was given as an explanation for diffusion barrier preventing Ti and Pd interlayer mixing.

It is therefore not well understood if the interdiffusion reported by Topic et al [2.24] could be due to the absence of TiH_2 when a mixture of 15% H + 85% Ar is used, as in the case of their experiment. It is worth noting that for hydrogen storage purposes, for hydrogen absorption and desorption over several cycles, a stable system of Ti-Pd is essential for long lifetime of usage.

2.3.2 The effect of thermal annealing Ti-Pd system in vacuum

When Ti-Pd system is annealed in vacuum it forms Ti-Pd intermetallic compounds at relatively high temperature of above 400 ^{o}C. The Ti-Pd interdiffusion is amplified at higher temperature environment.

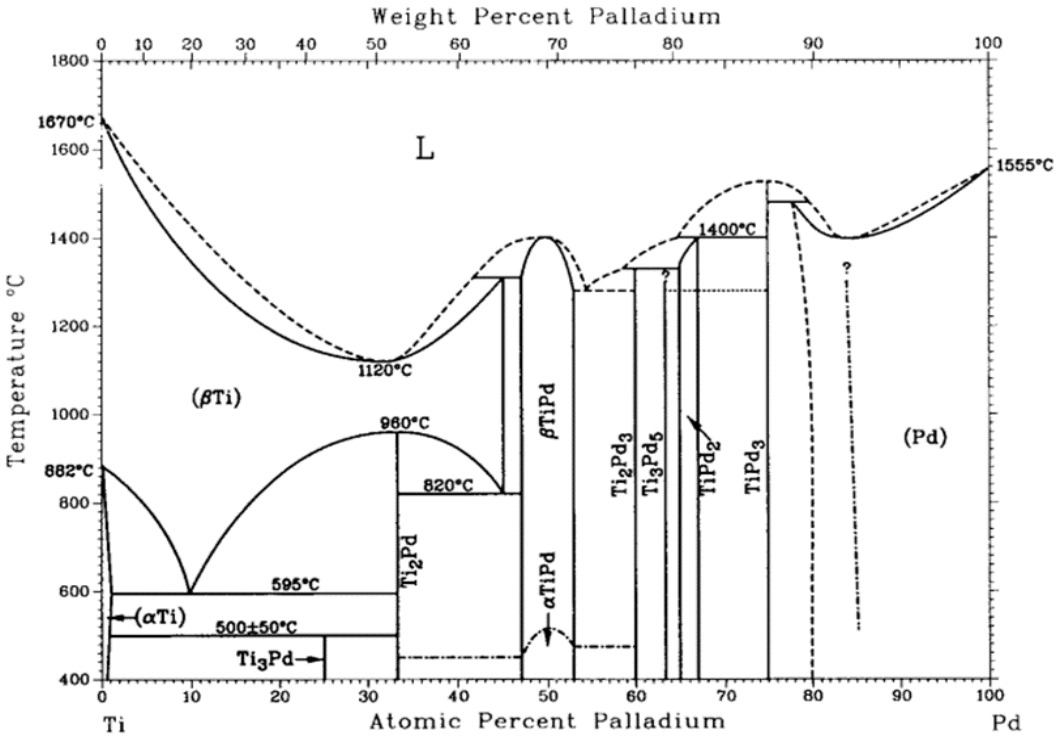

Figure 2.6: *The phase diagram of Ti-Pd system [2.36, 2.40].*

Numerous researchers have studied Ti-Pd phase transformation under vacuum and seven intermetallic compounds with different crystal structures were reported [2.30-2.42] and are summarized in table 2.1 with their respective references. Figure 2.6 shows the conditions under which those different compounds are formed.

Table 2.1: *Summarized literature of intermetallic Ti-Pd System.*

Phase	**Crystal structure**	**Type**	**Lattice parameters [Å]**			**References**
			A	*b*	*c*	
$\boldsymbol{TiPd_3}$	Hexagonal	$TiNi_3$	5.489	5.489	8.964	[2.31, 2.32, 2.33, 2.40]
$\boldsymbol{TiPd_3}$	Cubic	$AuCu_3$	3.985	3.985	3.985	[2.30]
$\boldsymbol{TiPd_2}$	Tetragonal	$MoSi_2$	3.24	3.240	8.480	[2.34, 2.35, 2.40]
$\boldsymbol{TiPd_2}$	Orthorhombic	$ReSi_2$	3.410	3.070	8.560	[2.34]
$\boldsymbol{Ti_3Pd_5}$	Tetragonal	tI8	3.260	3.260	11.430	[2.34, 2.40]
$\boldsymbol{Ti_2Pd_3}$	Cubic	oS20	4.610	14.33	4.640	[2.31, 2.36, 2.40]
$\boldsymbol{\alpha - TiPd}$	Orthorhombic	AuCd	4.560	2.810	4.890	[2.37, 2.38, 2.40]
$\boldsymbol{\beta - TiPd}$	Cubic	CsCl	3.180	3.180	3.180	[2.37, 2.38, 2.40]
$\boldsymbol{Ti_2Pd}$	Tetragonal	$MoSi_2$	3.090	3.090	10.054	[2.31, 2.36, 2.40, 2.42]
$\boldsymbol{Ti_3Pd}$	Cubic	Cr_3Si	5.055	5.055	5.055	[2.41]

Among this intermetallic compounds the tetragonal $MoSi_2$-type crystal structure of Ti_2Pd phase was reported to form stable hydride while $TiPd_2$ phase do not form a stable hydride [2.43, 2.44, 2.45]. The compound Ti_2Pd is known for its hydrogen storage capability [2.46] and the absorption can produce ternary metal hydride phase [2.43].

2.4 References

[2.1] N.A.A. Rusman, M. Dahari, A review on the current progress of metal hydrides material for solid-state hydrogen storage applications, *International Journal of Hydrogen Energy*, 41 (28), 12108-12126, (2016).

[2.2] Y. Sun, C. Shen, Q. Lai, W. Liu, D.W. Wang, K.F. Aguey-Zinsou, Tailoring magnesium based materials for hydrogen storage through synthesis: Current state of the art. *Energy Storage Materials*, 10, 168-198, (2018).

[2.3] A. Züttel, Hydrogen storage and distribution systems, *Mitigation and Adaptation Strategies for Global Change*, 12, 243- 365, (2007).

[2.4] M. Dornheim, Thermodynamics of metal hydrides: tailoring reaction enthalpies of hydrogen storage materials, *In Thermodynamics-Interaction Studies-Solids, Liquids and Gases*. InTech, (2011).

[2.5] R. R. Boyer, An overview on the use of titanium in the aerospace industry. *Materials Science and Engineering*: A213, 103-114, (1996).

[2.6] X. Liu, P.K. Chu, C. Ding, Surface modification of titanium, titanium alloys, and related materials for biomedical applications. *Materials Science and Engineering: R: Reports*, 47 (3-4), 49-121, (2004).

[2.7] O. Adesina, P. Popoola, O. Fatoba, Laser surface modification - A focus on the wear degradation of titanium alloy. Fiber Laser, 16, 368-381, (2016).

[2.8] Z. Tarnawski, N. T. H. Kim-Ngan, Hydrogen storage characteristics of Ti and V based thin film, *Jornal of science: Advanced materials and devices*, 1, 141-146, (2016).

[2.9] E. Tal-Gutelmacher and D. Eliezer, Hydrogen-Assisted Degradation of Titanium Based Alloys, *Materials Transactions*, 45, 1594 -1600, (2004).

[2.10] A. López-Suárez, J. Rickards, R. Trejo-Luna, Mechanical and microstructural changes of Ti and Ti–6Al–4V alloy induced by the absorption and desorption of hydrogen. *Journal of Alloys and Compounds*, 457 (1-2), 216-220, (2008).

[2.11] C. Leyens, M. Peters, editors. *Titanium and titanium alloys: fundamentals and applications*. John Wiley & Sons, 1-10, (2003).

[2.12] A. San-Martin, F.D. Manchester, The H-Ti (Hydrogen-Titanium) system, *Bulletin of Alloy Phase Diagrams*, 8, 30-42, (1987).

[2.13] R.S. Laptev, V.N. Kudiiarov, Y.S. Bordulev, A.A. Mikhaylov, A.M. Lider, Gas-phase hydrogenation influence on defect behavior in titanium-based hydrogen-storage material. *Progress in Natural Science: Materials International*, 27 (1), 105-111, (2017).

[2.14] N. E. Paton and J. C. Williams: Effect of Hydrogen on Behavior of Materials, (Eds: A. W. Thompson, I. M. Bernstein), (AIME, New York, 409 - 432, (1976).

[2.15] H. G. Nelson: Hydrogen Effects in Metals, (Eds.: A. W. Thompson, N.R. Moody), TMS, Warrendale, PA, 699 - 715, (1996).

[2.16] W.R. Kerr, The effect of hydrogen as a temporary alloying element on the Microstructure and Tensile Properties of Ti-6AI-4V, *Metallurgical Transactions A*, 16A, 1077 - 1078, (1995).

[2.17] J.I. Qazi, O.N. Senkov, F.H. Froes, Phase transformations in the Ti-6Al-4V-H system, *The Journal of The Minerals, Metals and Materials Society* , 54, 68 - 71, (2002).

[2.18] Y. Mahajan, S. Nadiv, W.R. Kerr, Studies of hydrogenation in Ti-6Al-4V alloy. *Scripta Metallurgica*, 13 (8), 695 - 699, (1979).

[2.19] I.N. Filimonov, V.V. Yuschenko, A.V. Smirnov, S.N. Nesterenko, I.V. Dobryakova, I.I. Ivanova, E.N. Lubnin, L. Galperin, R.H. Jensen, Deactivation of titanium during temperature-induced hydrogen absorption–desorption cycling: I. Effects of water, oxygen and nitrogen traces. *Journal of alloys and compounds*, 390 (1-2), 144 - 154, (2005).

[2.20] S.M. Lee, and T.P. Perng, Effect of the second phase on the initiation of hydrogenation of TiFe1− xMx (M= Cr, Mn) alloys. *International journal of hydrogen energy*, 19(3), .259 - 263, (1994).

[2.21] A. Lopez-Suarez, J Rickards, R. Trejo-Luna, Analysis of hydrogen absorption by Ti and Ti–6Al–4V using the ERDA technique. *International journal of hydrogen energy*, 28(10), 1107 - 1113, (2003).

[2.22] Y. Baoguo, W. Yujie, Z. Yubin, G. Longqing, Hydrogenation Behaviour of Ti6Al4V Alloy, *Rare metal Materials and Engineering*, 46(6), 1486 - 1490, (2017).

[2.23] S. Mazwi, Hydrogen storage in Ti-based coatings and Ti6Al4V alloy, unpublished master's thesis, *University of the Western Cape, Cape Town, South Africa*, (2016).

[2.24] M. Topić, S. Halindintwali, C. Mtshali, S. Nsengiyumva, Z.M. Khumalo, Hydrogen storage in Ti-based metal hydrides investigated by elastic recoil detection analysis (ERDA). *Nuclear Instruments and Methods in Physics Research Section B: Beam Interactions with Materials and Atoms*, 450, 239-243, (2019).

[2.25] S.Z. Ngwanakgagane, Hydrogenisation of metals, unpublished master's thesis, *University of the Western Cape, Cape Town, South Africa*, (2013).

[2.26] M.C. Burrell, N.R. Armstrong, Deuterium uptake in titanium thin films: t ssc00621 the effect of oxide, and the metal (Ti and Fe) overlayers. *Surface Science*, 160 (1), 235- 252, (1985).

[2.27] E. Gemelli, N.H.A. Camargo, Oxidation kinetics of commercially pure titanium. *Matéria (Rio de Janeiro)*, 12 (3), 525 - 531, (2007).

[2.28] L.L. Jewell, B.H. Davis, Review of absorption and adsorption in the hydrogen–palladium system. *Applied Catalysis A: General*, 310, 1 - 15 (2006).

[2.29] K. Drogowska, S. Flege, C. Schmitt, D. Rogalla, H.W. Becker, N.T. Kim-Ngan, A. Brudnik, Z. Tarnawski, K. Zakrzewska, M. Marszalek, A.G. Balogh, Hydrogen Charging Effects in Pd/Ti/TiO 2/Ti Thin Films Deposited on Si (111) Studied by Ion Beam Analysis Methods, *Advances in Materials Science and Engineering*, 2012, 1 - 8, (2011).

[2.30] N. Selhaoui, J.C. Gachon, J. Hertz, J Less Common Metals, 154, 137–47, (1989).

[2.31] E. Raub, E. Rөschel. *Z Metallk*, 59, 112 - 4, (1968).

[2.32] I.R. Harris, M. Norman, *Journal of Less Common Metals*, 22, 127 - 30, (1970).

[2.33] H. Schulz, K. Ritapal, W. Bronger, W.Z. Klemm, Anorg Allge Chemie, 357, 299 - 313, (1968).

[2.34] P .Krautwasser, S. Bahn, S. Schubert, *Z Metallk*, 59, 724 - 729, (1968).

[2.35] P. Wodniecki, B. Wodniecka, A. Kulınska, M. Uhrmacher, K.P. Lieb. *Journal of Alloys and Compounds*, 385, 53 - 58, (2004).

[2.36] H. Okamoto, Pd-Ti (palladium-titanium). *Journal of phase equilibria*, 14, 128-129, (1993).

[2.37] H.C. Donkersloot, J.H.N. Van Vucht. *Journal of Less Common Metals*, 20, 83 - 91, (1970).

[2.38] A.E. Dwight, Conner Jr RA, Downey JW. *Acta Crystallographica*, 18, 837 - 839, (1965).

[2.39] V.P. Sivokha, A.S. Savvinov, V.P. Voronin, V.N. Khachin, *Physics of metals and metallography*, 56, 112 - 116, (1983).

[2.40] J. L. Murray, the Pd-Ti (Palladium-Titanium) System, Bulletin of alloy phase diagrams, 3, 321 - 239, (1982).

[2.41] A. F. Jankowski, *Journal of alloys and compounds*, 182, 35 - 42, (1992).

[2.42] V.N. Eremenko, T.D. Shtepa, Phase diagram of titanium–palladium system. Poroshk. Metall, (3), 75 - 81, (1972).

[2.43] A. J. Maeland, G. G. Libowitz, Hydrogen absorption in some A_2B intermetallic compounds with the $MoSi_2$-type structure (C11b). Journal of the Less Common Metals, 74 (2), 295-300, (1980).

[2.44] R. Kadel, A. Weiss, Solubility of hydrogen in CuTi, CuTi2, PdTi2, Cu0.5Pd0.5Ti2. Reactions of titanium alloys with gaseous hydrogen, Ber. Bunsenges. *The Journal of Physical Chemistry*. 82 (12) 1290 - 1302, (1978).

[2.45] Dae-Bok Kang, comparison of bonding characteristics of hydrogen in Ti_2Pd and Pd_2Ti alloys, 32 1879 - 1883, (2011).

[2.46] R.C. Bowman, A. Attalla Jr, G.C. Abell, J.S. Cantrell, A.J. Maeland, *Journal of the Less Common Metals*, 172 - 174:643 - 8, (1991).

[2.47] A. Pundt, R. Kirchheim, Hydrogen in metals: microstructural aspects Annual Review of Material Research, 36, 555 - 608, (2006).

[2.48] F. Favier, E.C. Walter, M.P. Zach, T. Benter, R.M. Penner, . Hydrogen sensors and switches from electrodeposited palladium mesowire arrays. *Science*, *293*, 2227 - 2231, (2001).

[2.49] L.L. Jewell, B.H. Davis, Review of absorption and adsorption in the hydrogen–palladium system. *Applied Catalysis A: General*, 310, 1 - 15, (2006).

[2.50] E. Antolini, Palladium in fuel cell catalysis. *Energy & Environmental Science*, 2, 915 - 31, (2009).

[2.51] H.J. Christ, M. Schützand, S. Zeitler, Thermogravimetric study of the hydrogen uptake of the metastable β-titanium alloy Ti 38-6-44. *Materials and Corrosion*, 49 (1), 13 - 17 (1998).

[2.52] E.M.B. Heller, J.F. Suyver, A.M. Vredenberg, D.O. Boerma, Oxidation and annealing of thin FeTi layers covered with Pd, *Applied Surface Science*, 150, 227 - 234, (1999).

[2.53] A.L. Cabrera, J.I. Avila, D. Lederman, Hydrogen absorption by metallic thin films detected by optical transmittance measurements, *International Journal of Hydrogen Energy*, 35, 10613 - 10619, (1994).

[2.54] S.M. Tadayyon, O. Yoshinari, and K. Tanaka, Interdiffusion in Pd/Ti bilayer films studied by Auger electron depth profiling. *Japanese journal of applied physics*, *32*, 3928 - 3932 (1993).

[2.55] S.M. Tadayyon, Y. Fujimoto, K. Tanaka, M. Doi, M. Matsui, Solid-State Amorphization in Palladium/Titanium Multilayer Films during Sputter Deposition

and Postdeposition Annealing, *Japanese journal of applied physics*, 33, 4697- 4702, (1994).

[2.56] Y. Fujimoto, S.M. Tadayyon, O. Yoshinari, K. Tanaka, Effect of hydriding on structural stability of Ni/Ti and Pd/Ti multilayers. *Materials Transactions*, 38 (9), 780-786, (1997.).

[2.57] A.A. Ilyin, B.A. Kolachev, A.M. Mamonov, Phase and structure transformations in titanium alloys under thermohydrogenous treatment. Titanium, 92, .941 - 947, (1992).

CHAPTER THREE

Material and methods

3.1 Introduction

This chapter discusses the description of material, the preparation of the samples as well as the characterization techniques used for the investigations as it is illustrated in table 3.1.

Table 3.1: *Outline of chapter three (material and methods).*

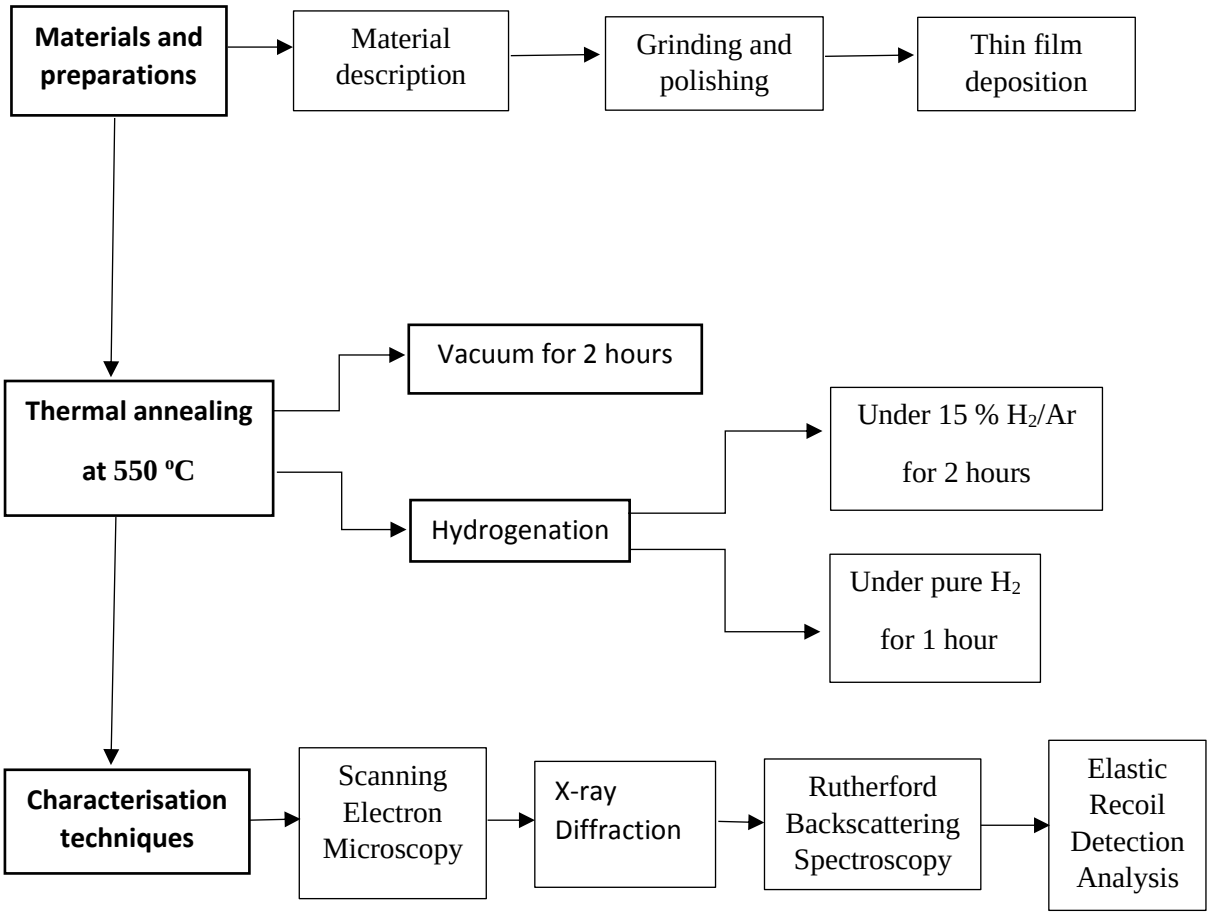

3.2 Material and preparations

3.2.1 Material description

Bulk material of commercially pure titanium (CP-Ti) with 99.6% purity and titanium alloy (Ti6Al4V) with 90 wt.% Ti, 6 wt.% Al and 4 wt.% V purchased from Good-Fellow company were used to prepare samples for the investigation. Small pieces of samples were cut out of the bulk material into the discs of dimensions 10 mm (diameter) and 2 mm (thickness) as shown in figure 3.1 (a). Other pieces were cut into cubes of dimensions 10×10 mm and 2 mm in thickness as shown in figure 3.1 (b). The next sections discuss the sample preparation and thin film deposition.

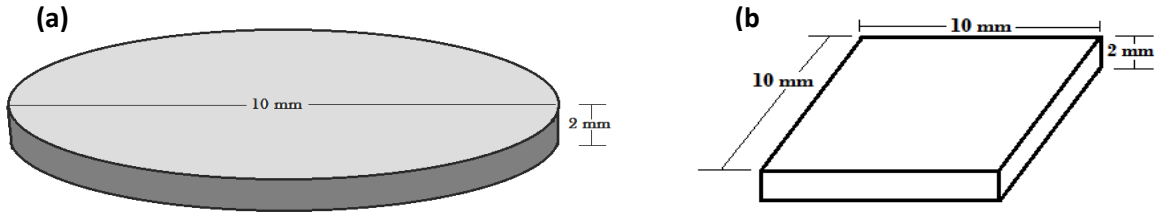

Figure 3.1: *Schematic representation of samples cut from bulk material of CP-Ti and Ti6Al4V; (a) disk of 10 mm diameter by 2 mm thickness, and (b) cube of 10×10 mm with a thickness of 2 mm.*

3.2.2 Grinding and polishing

All samples which were cut from bulk material of CP-Ti and Ti6Al4V-alloy were prepared for surface polishing at University of Cape Town at centre for material engineering. The samples were individually mounted on an acrylic resin using Struers Labopress-3 machine. During the mounting procedure, heating of 180 ^{o}C was applied to melt the acrylic resin and then cooling was also applied to solidify. The heating and cooling time was maintained at 6 minutes sequentially. During the cooling process, 20 kN force was applied and then the resin was solidified into the samples. After cooling of the resin, the samples were individually and sequentially grinded and polished. 800 µm Grit-SiC paper was first used to remove the

damage from sectioning, then followed by 1200 µm Grit-SiC paper to remove the lines from grinding process. Running water was used as a lubricant during the grinding process. On the polishing stage, the diamond paste with a grain size of 9 µm on MD DUR pad was used with a mixture of 25 ml colloidal silica suspension (OP-S) and 5 ml H_2O_2 were used as a lubricant to produce a mirror-like finish surface. The samples were then rinsed with water, followed by ethanol and they were dried using a hair dryer and then removed from the acrylic resin.

3.2.3 Thin film deposition

In preparation for thin film deposition, all polished samples were ultrasonically cleaned to remove the residue on the surface. The organic solvents were used sequentially as the cleaning reagents as follows; ethanol, acetone, trichloroethylene, acetone, and methanol. The cleaning time for every solvent was 10 minutes. Samples were dried using argon gas after cleaning. Clean samples were loaded into the electron beam evaporator as shown in figure 3.2. The targets of pure Pd and Ti pellet with 99.99% purity were placed in the separate crucible for thin film deposition.

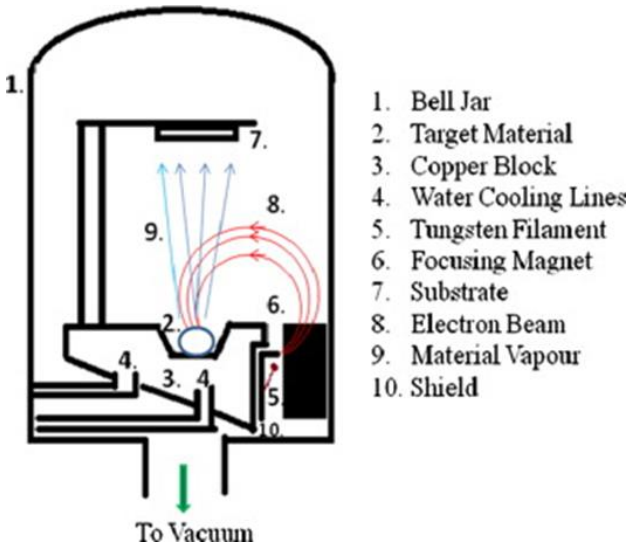

Figure 3.2: *Schematic representation of electron beam evaporator machine [3.1].*

Thin palladium (Pd) and titanium (Ti) films were deposited onto CP-Ti and Ti6Al4V-alloy samples using a high vacuum e-beam evaporator system equipped with crystal thickness monitor at room temperature. During deposition a voltage of 5 kV was applied across the tungsten filament creating emission of electrons. The emitted electrons are focused onto the target material using electromagnets. When the electron beam hits the target material, their kinetic energy is converted into thermal energy causing heat and material vapour within the target' surface. Vaporized material forms a coating on the surface of the substrate. Multilayer coated samples were produced as shown in schematic representation on figure 3.3. The deposition rate and chamber pressure were kept at about 0.6 Å/s and 10^{-6} mbar respectively during all depositions. Summary of all deposited samples is presented in table 3.2.

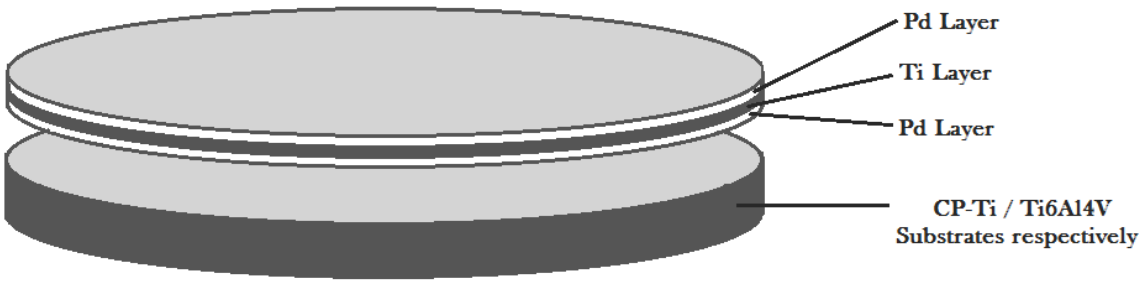

Figure 3.3: *The schematic structure of multilayer coated samples, where two samples of CP-Ti and Ti-6Al-4V were coated with Pd/Ti/Pd respectively.*

Table 3.2: *Summary of CP-Ti and Ti-6Al-4V samples coated with multilayer of Pd/Ti/Pd thin film.*

Substrates (Materials)	**Coating layers (element)**	**Coating thickness (nm)**
CP-Ti	Pd/Ti/Pd	50/25/50
Ti-6Al-4V	Pd/Ti/Pd	50/25/50
CP-Ti	Pd/Ti/Pd	100/25/100
Ti-6Al-4V	Pd/Ti/Pd	100/25/100

3.3 Vacuum annealing

In order to investigate the phase transformation, intermixing of multilayers and kinetics, some of the samples presented in table 3.2 were subjected to vacuum thermal annealing using an Elite Thermal System Limited furnace based at iThemba LABS. Samples were placed in a ceramic boat and loaded inside the quartz tube of the furnace maintained under vacuum. A base pressure of 10^{-7} mbar was achieved. The temperature was ramped up to 550 ^{o}C for the samples at a ramping rate of 1.0 ^{o}C/sec and kept at these temperatures for two hours. The samples were cooled down to room temperature at a rate of 3 ^{o}C/min in vacuum. Summary of the sample characteristics is presented in table 3.3.

Table 3.3: *Summary of thermally annealed substrates of coating layers under vacuum.*

Substrates (Material)	**Coating layer (element)**	**Coating thickness (nm)**	**Temperature (ºC)**	**Time (hours)**
CP-Ti	Pd/Ti/Pd	50/25/50	550	2
Ti-6Al-4V	Pd/Ti/Pd	50/25/50	550	2

3.4 Hydrogenation procedure

In order to investigate the capability and viability of the Ti-Pd material for hydrogen absorption and storage, hydrogenation experiments were conducted in one of the furnace situated at centre for material engineering at University of Cape Town using H_2(15%)/Ar(85%) gas mixture. Other samples were hydrogenated at physics department at University of the Western Cape using pure H_2. All hydrogenation experiments were conducted at a temperature of 550 ^oC with the flow rate of 100 SCCM for this investigation.

The hydrogenation procedure followed during the experiment with experimental conditions is described below and summary of the hydrogenated sample is presented in table 3.4.

i. Samples were mounted on the sample holder and inserted into a furnace. Vacuum was pumped up to 10^{-7} mbar, which then dropped during hydrogenation to 10^{-3} mbar.

ii. Samples were heated up to 550 ^oC, then hydrogen gas was allowed into the furnace at a constant flow rate of 100 SCCM and the pressure during hydrogenation was kept at 100 μbar. When using H_2/Ar gas mixture samples were hydrogenated for two hours, while using pure H_2 samples were hydrogenated for one hour.

iii. After hydrogenation, the furnace was switched off for allowing the samples to cool down to room temperature at a rate of 5 ^{o}C/min in the presence of hydrogen environment.

iv. At the end, samples were taken out of the furnace and kept at liquid nitrogen temperature to limit the hydrogen diffusion from the samples.

Table 3.4: *Summary of hydrogenated samples of Pd/Ti/Pd/CP-Ti and Pd/Ti/Pd/Ti6Al4V multilayer systems.*

samples	**H_2/Ar gas Flow rate (sccm)**	**Pure H_2 gas Flow rate (sccm)**	**Temperature (^{o}C)**	**Time (hour/s)**
Pd(50nm)/Ti(25nm)/Pd(50nm)/ CP-Ti	100	-	550	2
Pd(50nm)/Ti(25nm)/Pd(50nm)/ Ti6Al4V	100	-	550	2
Pd(50nm)/Ti(25nm)/Pd(50nm)/ CP-Ti	-	100	550	1
Pd(50nm)/Ti(25nm)/Pd(50nm)/ Ti6Al4V	-	100	550	1
Pd(100nm)/Ti(25nm)/Pd(100nm)/ CP-Ti	-	100	550	1
Pd(100nm)/Ti(25nm)/Pd(100nm)/ Ti6Al4V	-	100	550	1

3.5 Characterisation techniques

3.5.1 Scanning Electron Microscopy (SEM)

3.5.1.1 Introduction

Scanning electron microscopy (SEM) is an analytical technique used for analysis of surface morphology and chemical composition of the samples. SEM make uses of high energy (1-30 KeV) focused electron beam to scan surface of the material and eject secondary electrons from the specimen which are used to create an image of the sample' surface [3.2]. This technique is used to study the difference in surface morphology and cross-sectional view of the samples.

The SEM machine shown in figure 3.4 consists of; an electron gun with tungsten filament that produces electrons when energized with high voltage between (1-30 KeV), electromagnetic lenses to focus and narrow the beam of electrons into the centre of the microscope column, specimen stage for mounting the samples, electron detector to capture secondary electrons generated by primary electron beam in order to generate an image of the surface, computer for displaying image or results and deflecting coils to scan the beam across the surface of the sample. Other detectors can also be fitted inside the chamber to record Auger electrons, backscattered electrons and x-rays generated as a results of primary beam interacting with the sample. The machine is always operated under vacuum to ensure that the electrons travel freely through the column without any collision with nonessential particles and also increases the free path of the electrons in the column.

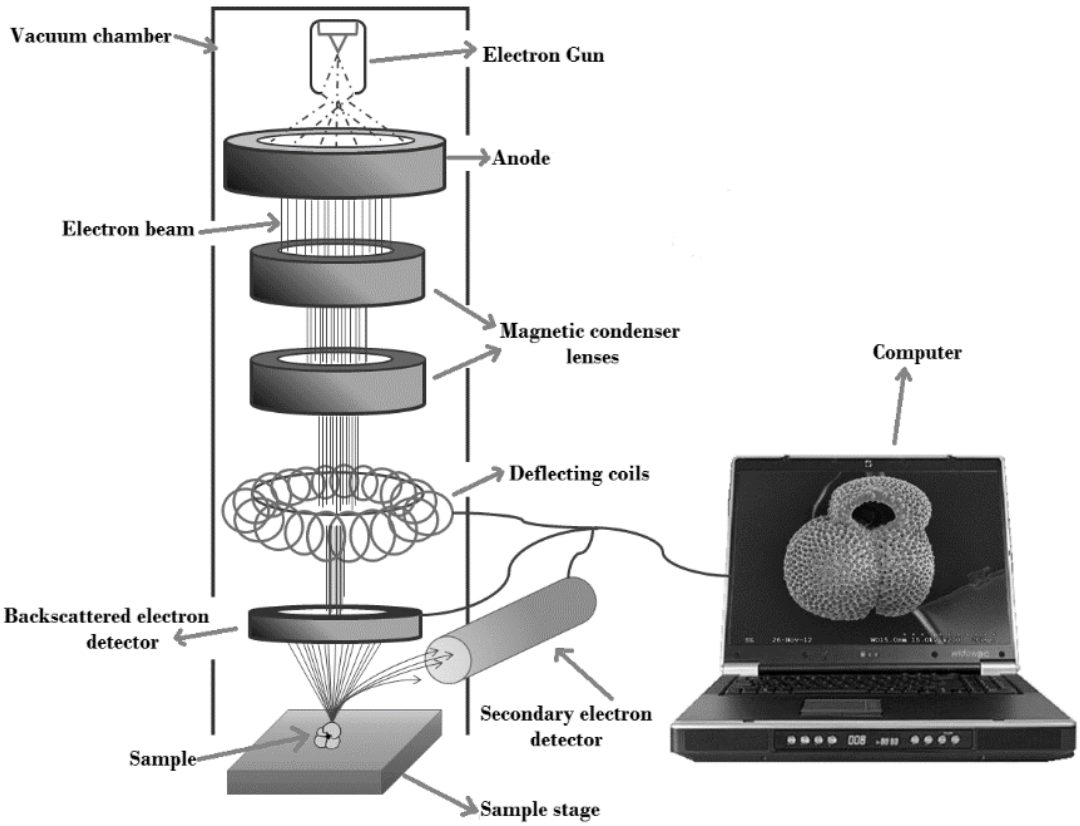

Figure 3.4: *Schematic of SEM column [3.3].*

3.5.1.2 Basic principles

Figure 3.5 displays different signals generated in the SEM and the principle is based on either elastic or inelastic interaction of energetic incident electron beam interacting with a sample being analysed. All these signals contain critical information about the sample being analysed, they can be detected and recorded using various detectors.

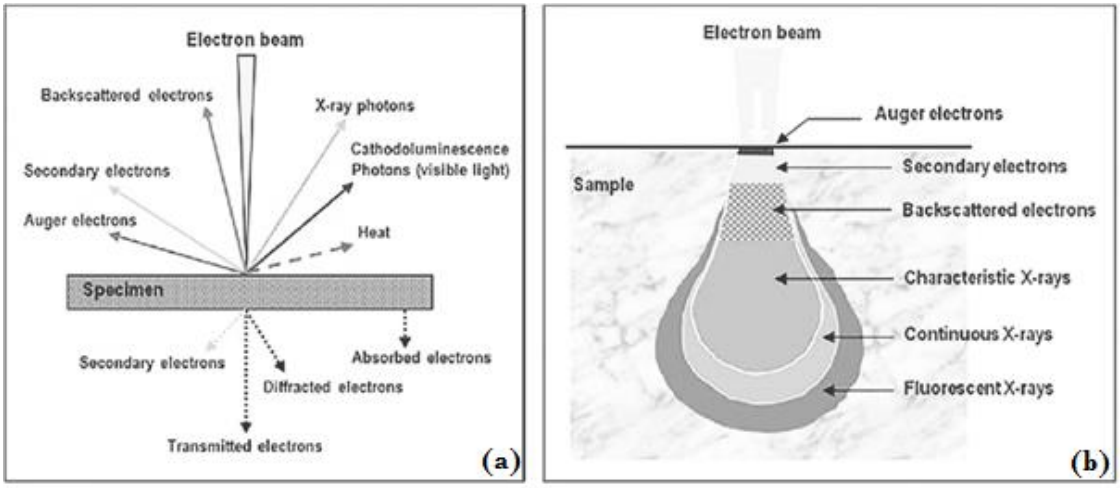

Figure 3.5: *Representation of signals generated by specimen-beam interaction, (b) interaction volume between the electron beam and the specimen [3.2].*

Elastic scattered electrons contains almost the whole energy of the incident beam; these electrons are regarded as backscattered electrons. Due to the high energy of the backscattered electrons they are able to escape the surface of the specimen with the energy greater than 50 eV. The signal of backscatted electrons gives information about specimen topography with the resolution about 1 µm.

Inelastic scattered electrons loose majority of their energy, which are referred to as secondary electrons. These electrons are low energetic less than 50 eV. They are absorbed by the surrounding atoms in the specimen when produced deep within the interaction volume as shown in figure 3.5 (b). Secondary electrons are therefore used to provide the surface image of the sample, since image created in the region of the primary beam interaction with the specimen surface and this image are responsible for high resolution imaging (in-lens Secondary Detector). The secondary electrons signal can feature surface structure down to 10 nm and better. Among other interaction volume is Auger electrons and X- rays. The Auger electrons contains very low energy which can escape within the vicinity of the few nm in the interaction volume see figure 3.5 (b).

Characteristic X-rays are mainly used to determine the elemental composition of the sample and its production principle is shown in figure 3.6. During the interaction of primary electron beam with the sample, highly energetic electrons from the electron, knock off the electrons from the inner K-shell of the specimen atom, leaving a vacancy. The atom will be left in an excited state, and an electron from the L-shell will undergo transition to fill the K-shell vacancy. When the L-shell undergoes transition it emits the X-ray photon of energy $E_{K\alpha}$. The emitted X-rays are characteristic of each element within the sample. Energy dispersive X-rays spectroscopy (EDS) is used to characterize sample by finding different elemental composition. The detection is achieved with the assistance of semiconductor detector. The absorbed X-rays by the detector excite number of electrons in the detector converting them into an electronic pulse signal, which is amplified and passed to multichannel analyser. The analyser sort the signal and count the number of X-rays received, then generate the EDS spectrum.

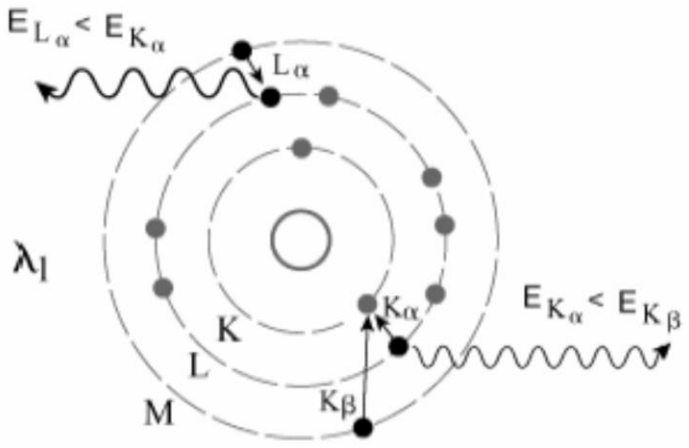

Figure 3.6: *Emission of characteristic X-ray by an atom [3.2].*

3.5.1.3 Experimental Setup

For this investigation the samples were mounted on the specimen stubs using carbon tabs and placed inside Auriga Zeiss instrument at University of the Western Cape. Voltage of 1 kV was applied and high resolution SEM images were obtained at working distance between 5.5

- 6.8 mm using secondary electrons. Energy dispersive spectroscopy (EDS) was performed using a Si detector attached to Auriga Zeiss instrument, where characteristic X-rays were used for determination of elemental composition.

3.5.2 X-Ray Diffraction (XRD)

3.5.2.1 Introduction

X-ray diffraction is an analytical technique used for determination of crystallographic information of the sample such as particle size, phase identification and as well as unit cell dimensions. The x-ray diffraction technique consists of x-ray source for generating beam of x-rays, sample holder for mounting the sample, x-ray detector to detect scattered x-rays and software for analysis. In this work x-ray diffraction was used for phase transformation analysis on Ti-Pd system under thermal annealing in vacuum, H_2/Ar gas mixture and pure H_2 gas.

3.5.2.2 Basic principle

Figure 3.7 display the basic principle of XRD which is based on interaction of the primary x-ray beam with the atoms of the sample being analysed, thereby producing scattering of the same x-rays into x-ray detector.

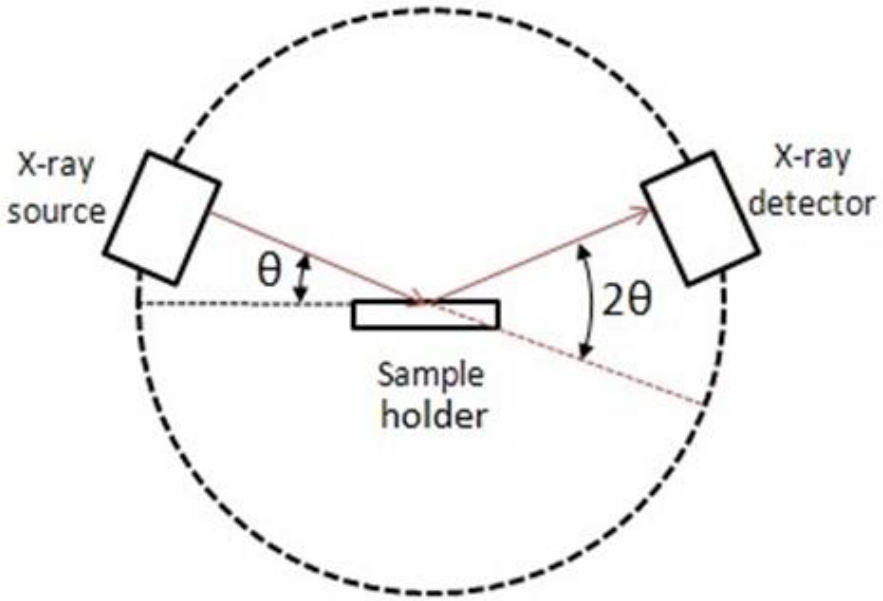

Figure 3.7: *Schematic arrangement of x-ray diffractometer [3.4].*

3.5.2.3 X-ray generation from the source

When high voltage is applied onto an anode plate within the X-ray tube the cathode filament emit the electrons. The emitted electrons are then accelerated under high vacuum towards the anode plate which is made out of copper metal and generate x-rays. Monochromatic x-rays then exit the tube through a beryllium window and directed to the sample. Diffracted x-rays are then recorded by the detector and produce XRD peak pattern of diffracted angle 2θ vs intensity.

3.5.2.4 X-ray interaction with the sample

The interaction and interpretation of the results is based on the theory that atoms within the materials are either distributed randomly or distributed in a periodic pattern and are represented by Point lattice see figure 3.8. When atoms are arranged randomly they result in amorphous, while arranged periodically in three dimension they result in crystalline material.

Point lattice is an array of points in a space organized in a way that each point has identical surroundings, as shown in figure 3.8 (a).

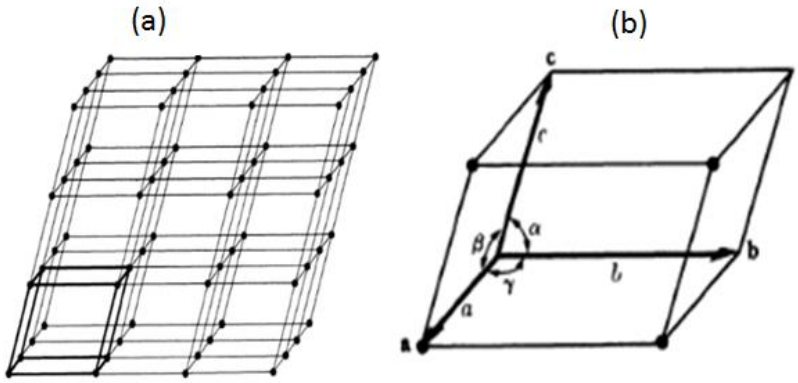

Figure 3.8: *Schematic representation of (a) point lattice, and (b) a unit cell [3.4].*

Figure 3.8 (b) shows a cube from the point lattice which represent a unit cell. This unit cell has parameters such as shape and size which can be described by three vectors a, b, and c drawn from one corner of unit cell. The lattice parameters of unit cell are formed by actual length of the vectors (a, b, c) and the angle between the vector (α, β, γ). The unit cell contains unique information about the point lattice, which makes the unit cell a building block of the crystal structure. There are fourteen possible point lattice so called Bravais lattice, whereby vectors a, b, & c and angles α, β, γ are having different unique values and forming special shapes, see Table 3.5.

Table 3.5: *Crystal system of fourteen Bravais lattice [3.4].*

Systems	**Axial lengths and angles**	**Bravais lattice**	**Lattice symbol**
Cubic	Three equal axis at right angles $a = b = c, \alpha = \beta = \gamma = 90^o$	Simple Body centered Face centered	P I F
Tetragonal	Three equal axis at right angles, two equal $a = b = c, \alpha = \beta = \gamma = 90^o$	Simple Body centered	P I
Orthorhombic	Three unequal axis at right angles $a \neq b \neq c, \alpha = \beta = \gamma = 90^o$	Simple Body centered Base centered Face centered	P I C F
Rhombohedral	Three equal axis at right angles, equally inclined $a = b = c, \alpha = \beta = \gamma \neq 90^o$	Simple	P
Hexagonal	Two equal co-planar axis at 120^o, $a = b \neq c, \alpha = \beta = 90^o, \gamma = 120^o,$	Simple	P
Monoclinic	Three unequal axis, one pair not at right angles $a \neq b \neq c, \alpha = \gamma = 90^o \neq \beta$	Simple Base centered	P C
Triclinic	Three unequal axis, unequally inclined and none at angles $a \neq b \neq c, \alpha \neq \beta \neq \gamma \neq 90^o$	Simple	P

When monochromatic beam of x-rays with wavelength (λ) incident on the crystal lattice at an angle (θ), with a distance (*d)* on one plane as shown in Figure 3.9, each planes of atoms in a periodic pattern with equal space between the atoms is capable of scattering incident radiation constructively or destructively. Only those x-rays which undergone constructive interference will reach the detector and can be expressed using Bragg's law (equation 3.1) as illustrated in figure 3.9. The Bragg's law can be expressed mathematically as follows;

$$n\lambda = 2dsin\theta \tag{3.1}$$

Where n represent integer, λ is the x-ray wavelength, d is crystal plane separation, and θ is the angle between incident x-ray beam or reflected beam, and crystal plane.

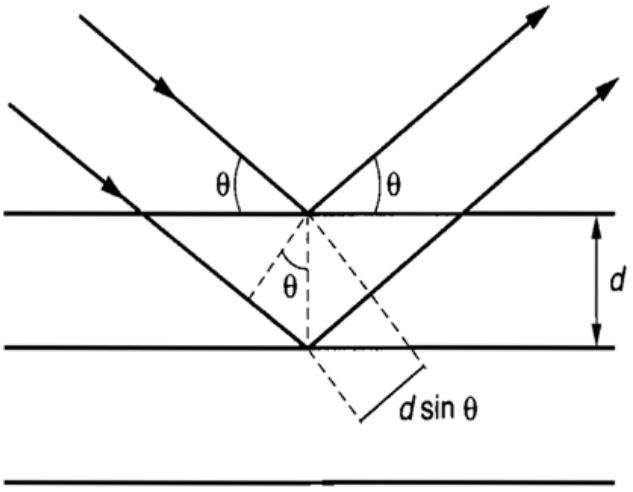

Figure 3.9: *Shows constrictive interference of x-ray and illustration of Bragg's law [3.4].*

The investigation of XRD analysis was done at Material Research Department iThemba LABS using Bruker D8-Advance-8 advance x-ray diffractometer with CuK_α of 1.54050 Å, a voltage of 40 KV and current of 40mA. The measurements were done at room temperature in the angle between 35^o to 80^o in 2*theta*. Counts were collected for 96 seconds per step at angular step size of 0.034^o.

3.5.3 Rutherford Backscattering Spectroscopy (RBS)

3.5.3.1 Introduction

RBS is a quantitative, non-destructive technique that is used to analyse the depth profiling of the atoms on thin films and bulk materials. It is based on the scattering of alpha particle by atoms, which was first investigated by Ernest Rutherford in 1908 who hypothesised that an atom is made of lighter dense of positive charge (nucleus) surrounded by lighter dense of negative charge (electrons). Geiger and Marsden confirmed Rutherford's hypothesis by directing alpha particles into free standing gold foil while observing flashes of scattered light on a fluorescence screen and began the development of RBS technique for thin film analysis.

This technique is more sensitive to heavy elements and less sensitive to light elements and is routinely used in many laboratories and in modern technology to characterise materials. Typically, information that can be obtained using this technique include depth information, thickness of the film, stoichiometry, and diffusion kinetics of grown multilayer films. For normal standard RBS, typically parameters are as listed in table 3.6.

Table 3.6: *Parameters and normal standards for RBS [3.5].*

RBS standard	**Parameters**
Beam	$\sim$2 mm
Lateral resolution	$\sim$2 mm
Depth resolution	$\geq$ 10 nm ($\geq$ 1 nm for glacing angle set $-$ up)
Detection sensitivity	$\geq 10^{-2}$ atomic layers for heavy impurities on light substrates, tens of at% for light elements in heavy substrates
Analysis depth	$\geq$ 3 µm

Mass resolution	≥ 3 μm amu at mass 50 amu target and ≥ 20 at 200 amu target
Overall accuracy	~5 %

Furthermore, RBS is based on the elastic interaction between incident particles and target atoms as shown in figure 3.10 and schematically represented in figure 3.11 which is depended on particle's parameter such as the energy, velocity, mass of the ion, atomic size, etc. This technique further involves fundamental physics concepts of interaction such as kinematics and energy transfer, Rutherford scattering cross section, energy loss and ion stopping also energy straggling which are briefly discussed below.

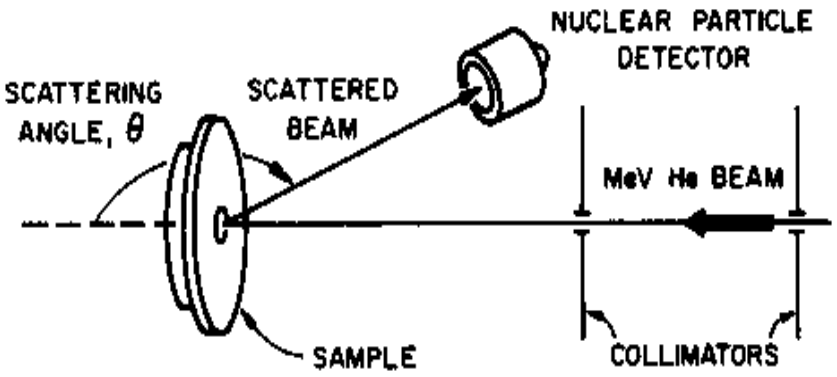

Figure 3.10: *Schematic representation of experimental setup for RBS [3.6].*

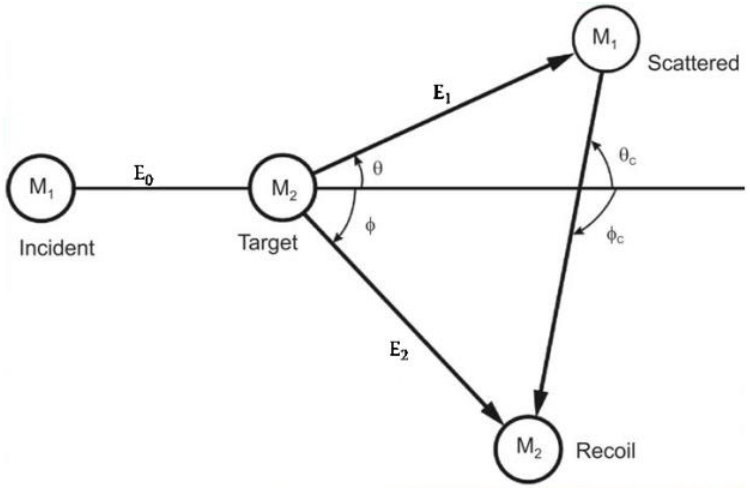

Figure 3.11: *Schematic representation of the collision process that take place in the sample between projectile of mass M_1, energy E_0 and target of mass M_2, initially at rest [3.6].*

3.5.3.2 Kinematic factor

In an elastic interaction that happens during RBS experiment, there are incident particles being scattered to a certain angle as shown in figure 3.11, two laws of physics in the perpendicular and parallel direction of the incident beam play major role. These laws are;

1. The Conservation of energy given by:

$$E = \frac{1}{2}M_1v_0^2 = \frac{1}{2}M_1v_1^2 + \frac{1}{2}M_2v_2^2 \tag{3.2}$$

2. The conservation of Momentum given by:

$$P = M_1v_0 = M_1v_1 + M_2v_2 \rightarrow \begin{cases} M_1v_0 = M_1v_1\cos\theta + M_2v_2\cos\phi \\ 0 \quad\quad = M_1v_1\sin\theta - M_2v_2\sin\phi \end{cases} \tag{3.3}$$

Combination results of these laws outcomes in kinematic factor (K) equation given by:

$$K_1 = E_1/E_0 = \left(\frac{\left(\sqrt{M_2^2 - M_1^2\sin^2\theta}\right) + M_1\cos\theta}{M_1 + M_2}\right)^2 \tag{3.4}$$

For recoil atom M_2, kinematic factor equation (K_2) is given by:

$$K_2 = E_2/E_0 = \left[\frac{\sqrt{1-(R\sin\theta)^2} + R\cos\theta}{(1+R)}\right]^2 \text{ ,Where } R = \frac{M_1}{M_2} \tag{3.5}$$

This factor K is important in determining what is in the target materials being investigated.

3.5.3.3 Rutherford scattering cross section

During interaction between incident particles and target atoms, incident atoms experience many collision and loose energy during that collision. One fundamental parameter that defines the amount of collisions and the probability of collision is scattering cross-section. It is normally referred to as angular cross section. It gives a measure of the probability of scattering a projectile into some angle. The use of this fundamental parameter is evidenced in

the instances where collision is purely Coulombic, as in the case for Rutherford scattering where the interaction involves interatomic potential V(r) given by

$$V(r) = \frac{Z_1 Z_2 e^2}{r} \tag{3.6}$$

The Rutherford differential scattering cross-section for the laboratory frame of reference, after derivation is given by:

$$\frac{d\sigma(\theta)}{d\Omega} = \left(\frac{Z_1 Z_2 e^2}{4E}\right)^2 \frac{4}{\sin^4\theta} \frac{\left\{\left[1-((M_1/M_2)\sin\theta)^2\right]^{1/2}+\cos\theta\right\}^2}{\left[1-((M_1/M_2)\sin\theta)^2\right]^{1/2}} \tag{3.7}$$

This fundamental parameter give an indication of how much collision was involved and therefore the amount of atoms constitute target area. Deviation from Rutherford differential scattering cross-section occurs at low energies of the incident beam due to the screening by orbitals electrons and therefore require application of screening potential. Also at higher energies where the distance of closets approach of nuclei within nuclear forces comes into effect and coulombic potential is not applicable, deviation occur.

Furthermore, the shape of the spectrum and spectrum yield or even counts is dependent on this fundamental parameter. The spectrum yield of backscattered particles is given by:

$$Y = \sigma(\theta)\Omega Q N \Delta t / \cos\theta_1 \tag{3.8}$$

Where; $\sigma(\theta)$ is the scattering cross-section at angle θ and Ω is the detector solid angle.

Q is the measured number of incident particles

N is the atomic density, which makes $N\Delta t$ the number of target atoms per unit area in the layer Δt thick

θ_1 is the angle between the incident beam and the surface normal of the target.

Applying Rutherford scattering cross-section for the analysis of thin film layer with thickness t, equation 3.8 becomes:

$$Y(t) \cong \left(\frac{Z_1 Z_2 e^2}{4E}\right)^2 \Omega Q N \Delta t \propto \frac{1}{E(t)^2} \tag{3.9}$$

3.5.3.4 Energy loss and Ion stopping

The energy loss parameter, Ion stopping and energy straggling give indication of depth scale and therefore the thickness of a particular layer. As mentioned above that during the interaction, incident ions loose energy via collision with target atoms, this loss happens via two processes:

(1) Nuclear collision (elastic), in which energy is transmitted as translator motion to target atoms as a whole.

(2) Electronic collision (inelastic), in which the moving particle loses its kinetic energy by exciting or ejecting atomic electrons.

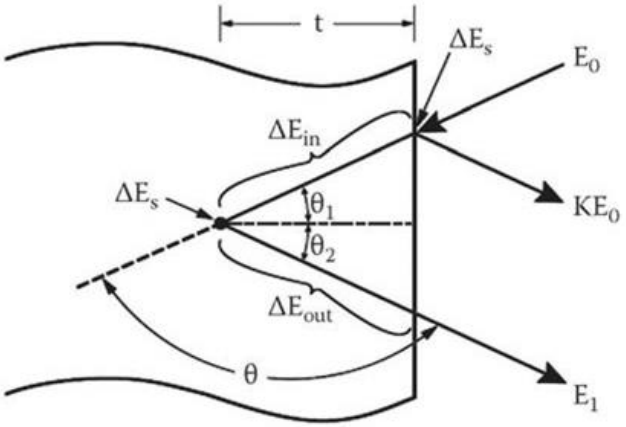

Figure 3.12: *Schematic representation of energy loss components for an incident ion scattered from a depth t, in a single element target [3.7].*

The energy-loss rate can be expressed by:

$$\frac{dE}{dx} = \left.\frac{dE}{dx}\right|_n + \left.\frac{dE}{dx}\right|_e \tag{3.10}$$

And the stopping cross-section given by:

$$\varepsilon^A \equiv \frac{dE/dx}{N} \tag{3.11}$$

Where N is the atomic density

The energy of the particle measured at the detector after going though target layer shown in figure 3.12 is dependent on energy loss rate and the path travelled going in and coming out of the target layer and it is given by:

$$E_1 = E_0 - (\Delta E_s + \Delta E_{in} + \Delta E_{out}) = KE_t - \Delta E_{out} \tag{3.12}$$

Where E_0 is energy of the incident projectile, K is backscattering kinetic factor E_1/E_0, ΔE_{in}, the total energy loss into depth t, ΔE_s, the energy lost in the elastic scattering process and ΔE_{out}, the energy lost to electronic stopping on the outwards of depth t.

The energy losses going in and out are respectively given by:

$$\Delta E_{in} = \int_0^{t/\cos\theta_1} \left.\frac{dE}{dx}\right|_{in} dx \cong \frac{t}{\cos\theta_1}\left.\frac{dE}{dx}\right|_{in} \tag{3.13}$$

And

$$\Delta E_{out} = \int_0^{t/\cos\theta_2} \left.\frac{dE}{dx}\right|_{out} dx \cong \frac{t}{\cos\theta_2}\left.\frac{dE}{dx}\right|_{out} \tag{3.14}$$

3.5.3.5 Experimental setup

The 3MV Tandetron accelerator from iThemba LABS was used to irradiate the samples with 1 mm collimated 2 MeV He^{++} ions, and the voltage of 50 kV was applied. Individual samples were mounted on the sample ladder and loaded into the chamber. The samples were tilted by angle (α) of 5º towards the Si surface barrier detector with energy resolution of ~23 keV positioned at a scattering angle (θ) of 150º see figure 3.13. An average current of 60 nA and total charge of 20 μC were used for all samples. The vacuum pressure during measurement was 10^{-6} mbar. The channel number calibration in terms of backscattered energy of particles was achieved using gold-cobalt on top of silicon dioxide deposited on silicon substrate (AuCo/SiO2/Si) standard sample. Simulations of RBS spectra were achieved using SIMNRA software version [3.8].

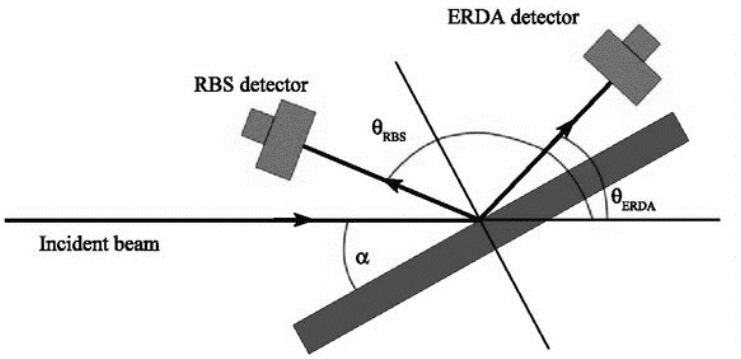

Figure 3.13: *Schematic diagram of RBS and ERD, where α is tilt angle and θ is the scattering angle [3.9].*

3.5.4.1 Elastic Recoil Detection Analysis (ERDA)

ERDA is one of ion beam analysis technique used for depth profile of lighter elements depending on the incident ion mass [3.10]. For example krypton can recoil (1<Z<40) while oxygen can recoil (1<Z<11) at recoil angle of 30°. The technique relies on the concept of recoiling lighter atoms of target material into the detector as shown in figure 3.14

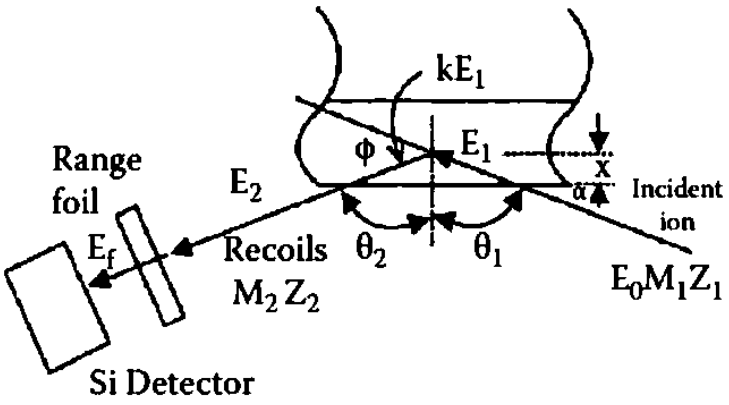

Figure 3.14: *Schematic representation of incident ion penetrating the sample (depth x) and a recoiling atom of a target after collision with energy E_0 and kE_1 respectively, escaping energy E_2 of the recoil atom [3.7].*

This technique is based on the transfer of energy from the incident ions into target atoms and during the process, target atoms are recoiled into the detector. This energy transfer from M_1 (incident ion) into M_2 (target atom) can be described and calculated via conservation of energy and momentum as in the case of RBS. The recoil kinematic factor (K_R) in the laboratory frame of reference can be given by:

$$K_R = \frac{E_2}{E_0} = \left[\frac{4M_1M_2}{(M_1+M_2)^2}\right]\cos^2\phi \qquad (3.15)$$

Where E_0, E_2 and ϕ are energy of the incident particle, energy of the recoil and recoil angle respectively. In ERDA, where $M_1>M_2$ the only way to satisfy the positive sign for the radical

term is for the elastically scattered projectiles to be limited within a cone such as recoil angle of 30^{o} for conventional ERDA.

As with RBS the capability of ERDA to quantify relies on the fundamental parameter such as cross-section which describes the probability of recoiling target atom to preferred recoil angle guided by interatomic interaction potential. For coulombic interaction such as Rutherford interaction, the recoil cross-section is given by

$$\frac{d\sigma(\theta)}{d\Omega} = \left(\frac{Z_1 Z_2 e^2}{2E_1}\right)^2 \left(\frac{M_1+M_2}{M_2}\right)^2 \frac{1}{\cos^3\phi} \tag{3.16}$$

Where E is given in MeV, e^2 =1.44 $\times 10^{-13}$ MeV. cm, and $(d\sigma/d\Omega)_\phi$ is given in square centimetres.

In ERDA, when it comes to energy loss concept, the total energy loss by incident ion as it penetrates and recoil atoms of the target is considered. As shown in figure 3.14, the incident ion enters the target surface at a certain angle and collide with target atoms transferring energy to recoil them to the detector where they arrive at the surface of the detector with the residue energy given by:

$$E_{detector} = K_R \left[E_0 - \int_0^{x/\sin\beta} S_p(x)dr\right] - \int_0^{x/\sin(\phi-\beta)} S_{rec}(x)dr \tag{3.17}$$

Where $S_p(x)$ and $S_{rec}(x)$ are stopping forces of the incident ion and recoil atom respectively. The first term gives residual energy of the incident ion before collision and second term give energy loss of the recoil atom as it exits the surface of the target.

Generally, the stopping force is used in converting energy into depth information and is given by:

$$S = dE/dx = \Delta E/\Delta x \tag{3.18}$$

Where dE and dx are the energy loss and distanced travelled respectively. ΔE and Δx are energy resolution and depth resolution. Stopping forces can be estimated using semi experimental parameterisation method through simulation code SRIM by Ziegler et al. [3.5] estimation is much more accurate for lighter incident ions such as hydrogen and helium ions but can deviate up to 20% for heavier ions.

3.5.4.2 Experimental setup

The 3MV Tandetron accelerator from iThemba LABS was used to irradiate the samples with 1 mm collimated 3 MeV He^{++} ions, and the voltage of 50 kV was applied. Individual samples were mounted on the sample ladder along with a 15 μm kapton foil for channel number/energy calibration and loaded into sample chamber evacuated to a vacuum pressure of 10^{-6} mbar. Energy calibration on kapton were collected using He^{++} beam energies of 2, 2.5, 3 MeV, thereafter samples were measured using a beam energy of 3 MeV. The average current of 60 nA and a total collected charge of 20 μC were maintained in all samples. The energy spectra of recoiled hydrogen atoms were recorded using Si surface detector with energy resolution of ~25 Kev positioned at recoiled angle of 30^o see figure 3.13. The simulation and analysis of ERDA spectra were done with SIMNRA software [3.8]. The depth profiling of hydrogen concentration from simulated spectra were calculated using the following equation

$$\sum_{i=1}^{n} \frac{H_i t_i}{T}$$

Where: *i* in the equation is considered as the order number of layers in the sample. *H* is the hydrogen concentration at a specific layer in at.%, *t* is the thickness at that specific layer in monolayers ($1 \times 10^{15} atoms/cm^2$) and *T* is the total thickness

3.6 References

[3.1] P. Mohanty, D. Kabiraj, , R.K. Mandal, P.K. Kulriya, A.S.K. Sinha, and C. Rath, Evidence of room temperature ferromagnetism in argon/oxygen annealed TiO_2 thin films deposited by electron beam evaporation technique. *Journal of Magnetism and Magnetic Materials*, 355, 240 - 245, (2014).

[3.2] J. Humphreys, R. Beanland, and P.J. Goodhew, *Electron microscopy and analysis*. CRC Press (2014).

[3.3] S. Hussain, Investigation of Structural and Optical Properties of Nanocrystalline ZnO, MSc Dissertation, *Linkoping University, Sweden*, (2008).

[3.4] B.D. Cullity, S. R. Stock, Elements of X-ray Diffraction, Third Edition. *New York: Prentice-Hall*, (2001).

[3.5] Ziegler, James F., Matthias D. Ziegler, and Jochen P. Biersack. SRIM*: the stopping and range of ions in matter*. Cadence Design Systems, 2008.

[3.6] L.C. Feldman, and J.W. Mayer, Fundamentals of surface and thin film analysis. *North Holland, Elsevier Science Publishers, P. O. Box 211, 1000 AE Amsterdam, The Netherlands*, (1986).

[3.7] M. Nastasi, J.W. Mayer, and Y. Wang, Ion beam analysis: fundamentals and applications. *CRC Press*, (2014).

[3.8] Mayer, M., Max-Planck-Institut für Plasmaphysik, Garching, Germany, SIMNRA User's Guide, 6, (2008).

[3.9] Z. Alfassi, and M. Peisach, Elemental analysis by particle accelerators. *CRC Press*, (1991).

[3.10] B.L. Doyle, and D.K. Brice, The analysis of elastic recoil detection data. *Nuclear Instruments and Methods in Physics Research Section B: Beam Interactions with Materials and Atoms*, *35*(3-4), 301 - 308, (1988).

CHAPTER FOUR

Results and Discussion

4.1 Introduction.

This chapter presents and discusses the results obtained from the different and complementary analytical techniques used. It is arranged in the following sections. Section 4.2 discusses the effect of thermal annealing on Ti-Pd multilayer systems in vacuum; section 4.3 presents the results of hydrogenation of Ti-Pd multilayer systems in H_2(15%)/Ar(85%) gas mixture atmosphere; section 4.4 reports on hydrogenation of the same system in pure H_2 gas and the last section 4.5 studies the effect of the catalyst's thickness on hydrogen storage capacity of Ti-Pd systems.

4.2 The effect of thermal annealing in vacuum.

As discussed in the literature review section, recent studies [4.1 - 4.5] have reported an optimum temperature for hydrogen absorption of 550 ^{o}C in Ti and Ti6Al4V alloy. At this particular temperature structural transformations occur, resulting in the formation of various intermetallic compounds depending on the atoms involved in the process. Therefore, it was important to investigate firstly the thermal stability of the system at this particular temperature. For this purpose, Ti and Ti6Al4V substrates were coated with Pd(50 nm)/Ti(25 nm)/Pd(50 nm) triple layer stack and the systems were thermally annealed in vacuum at 550 ^{o}C for 2 hours.

The samples were then characterised using SEM for surface morphological changes, XRD for phase transformations, and RBS for inter-diffusion and depth profile analyses.

4.2.1 Microstructural changes' analysis.

Figure 4.1 shows SEM micrographs of Pd(50 nm)/Ti(25 nm)/Pd(50 nm) multilayer stack deposited on (a) CP-Ti, (b) Ti6Al4V alloy, (c) deposited on CP-Ti then thermally annealed at 550 ^{o}C for 2 hours and (d) deposited on Ti6Al4V alloy then thermally annealed at 550 ^{o}C for 2 hours. For both substrates, the as-deposited samples showed relatively homogeneous and smooth surfaces.

In contrast, the samples annealed at 550 ^{o}C under vacuum showed, for both substrates, a rougher surface with interconnected crystals. The crystalline growth in the annealed samples suggests reactions that occurred leading to surface transformation.

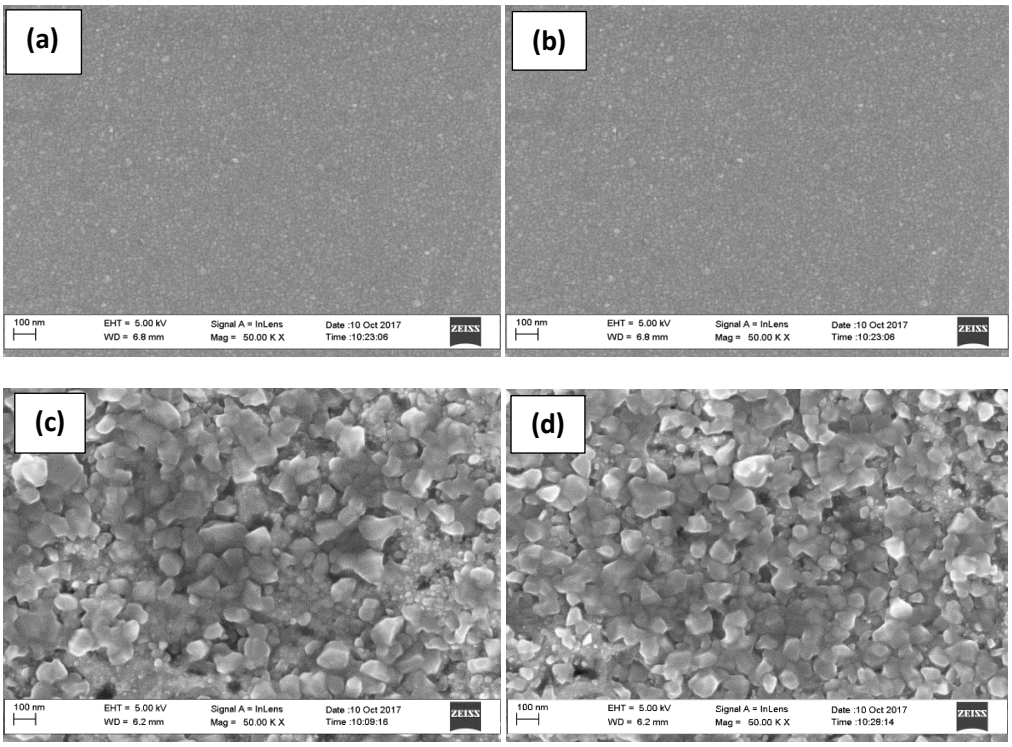

Figure 4.1: *SEM micrographs of (a-b) as- deposited samples, (c-d) thermal annealed sample at 550 ^{o}C for 2 hours in vacuum.*

SEM, which is a surface technique for morphological investigation, cannot provide further information on the structural transformation in the bulk; therefore, in order to correlate the morphological and structural transformations, XRD was used for phase analysis.

4.2.2 Crystal structure and phase transformation.

Figure 4.2 (a)–(b) present in red font the XRD spectra of the as-deposited Pd(50 nm)/Ti(25 nm)/Pd(50 nm) multilayer stack on CP-Ti and on Ti6Al4V-alloy respectively. The patterns in blue font are those of the vacuum thermally annealed samples on both substrates. For comparison, the XRD patterns of as-received substrates are shown in black font.

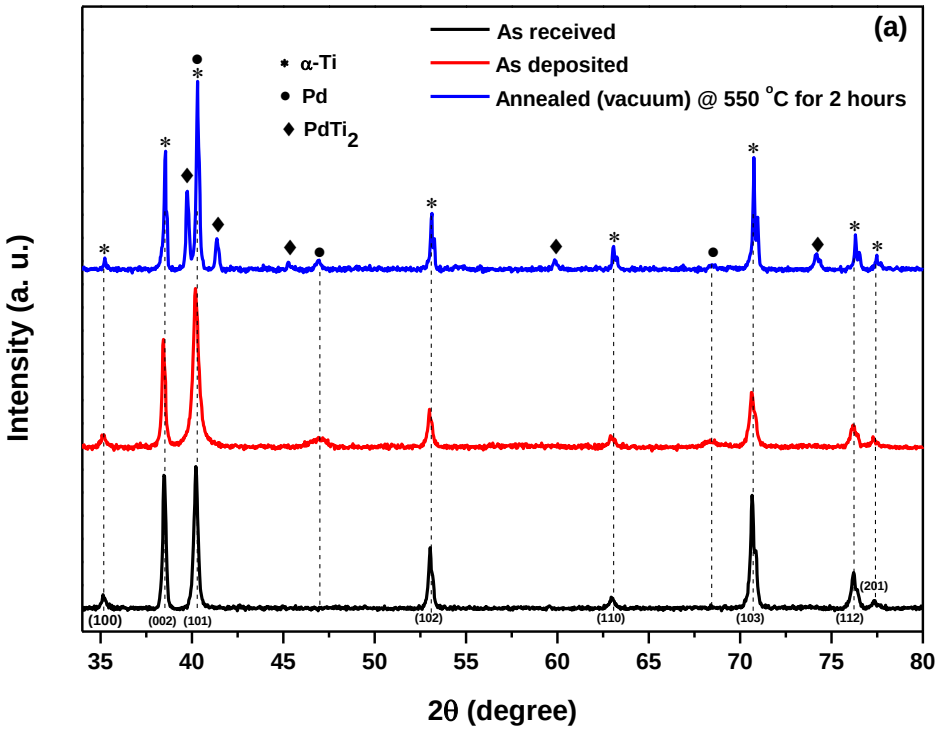

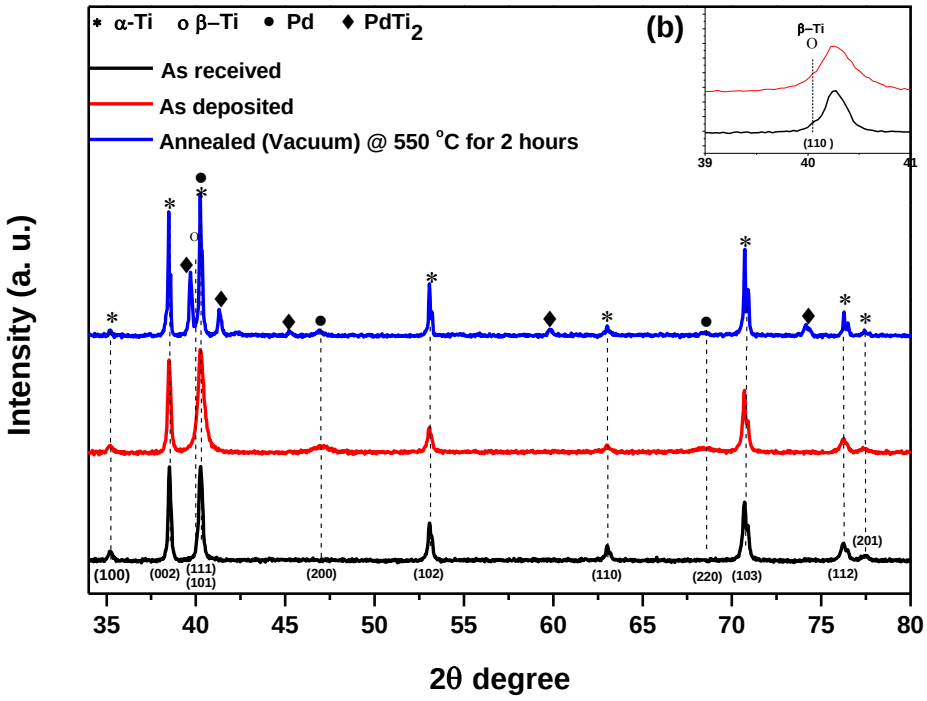

Figure 4.2: *XRD patterns of (a) as-received, as-deposited and annealed samples, on CP-Ti substrate and (b) those of as-received, as-deposited and annealed samples, on Ti6Al4V alloy substrate.*

In both systems, the as-received CP-Ti and Ti6Al4V alloy displayed both peaks corresponding to the hexagonal α-Ti phase (pattern no: 00-044-1294), with lattice parameters a = 2.95 Å and c = 4.68 Å, but for the Ti6Al4V alloy, an additional peak corresponding to β-Ti phase (pattern no: 00-044-1288) with lattice parameters a = 3.31 Å was observed (please see the insert on fig. 4.2(b)). Compared to the as-received patterns, the as-deposited samples in both systems also showed additional diffraction peaks corresponding to face-centered cubic (FCC) Pd (pattern no: 00-046-1043) with lattice parameters a = 3.89 Å..

Meanwhile, results from vacuum annealed sample at 550 ^{o}C displayed a combination of peaks corresponding to the face-centered cubic (FCC) Pd (pattern no: 00-046-1043) with lattice parameters a = 3.89 Å, hexagonal α-Ti phase (pattern no: 00-044-1294) with lattice parameters a = 2.95 Å and c = 4.68 Å and the body-centered tetragonal (BCT) $PdTi_2$ (pattern

no: 00-018-0957) with lattice parameters a = 3.090 Å and c = 10.054 Å, indicating interfacial mixing of layers as a result of thermal annealing in both systems.

The formation of $PdTi_2$ phase is an indication of the suitability of the system for hydrogen absorption since this phase has been reported to be the one responsible for hydrogen absorption [4.6, 4.7] it is also an indication of the elemental inter-diffusion across the Ti and Pd deposited layers. To further investigate the inter-diffusion and the formation of compounds, RBS was used.

4.2.3 RBS spectral analysis.

The probed depth in this investigation was calculated using SRIM2013 software. For both CP-Ti and Ti6Al4V, the simulation gave a penetration range of ~4.7 μm using 2 MeV He^{++} ions and therefore, the probed depth could be only limited to a depth less than 4.7 μm.

Figure 4.3 displays RBS spectra of the as-deposited Pd(50 nm)/Ti(25 nm)/Pd(50 nm) multilayer stack and the vacuum annealed samples (a) on CP-Ti and (b) on Ti6Al4V alloy for 2 hours at 550 °C.

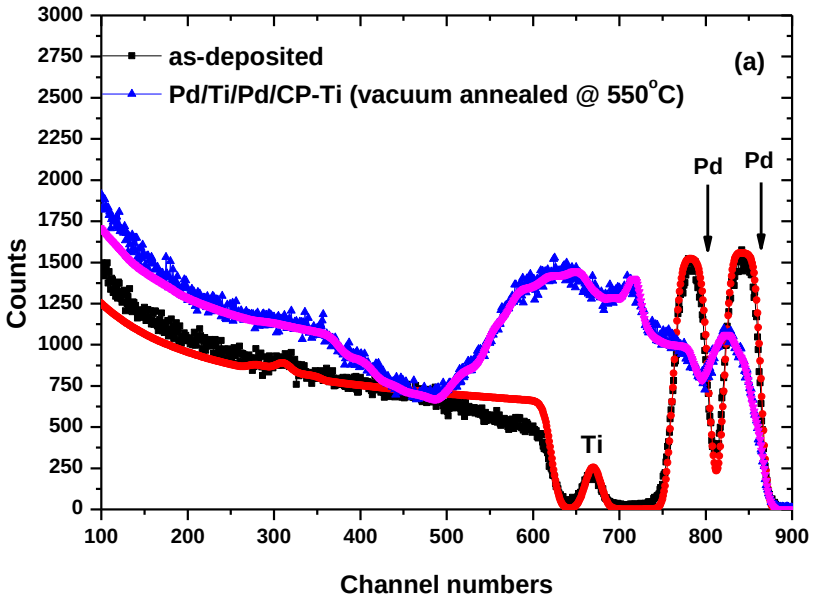

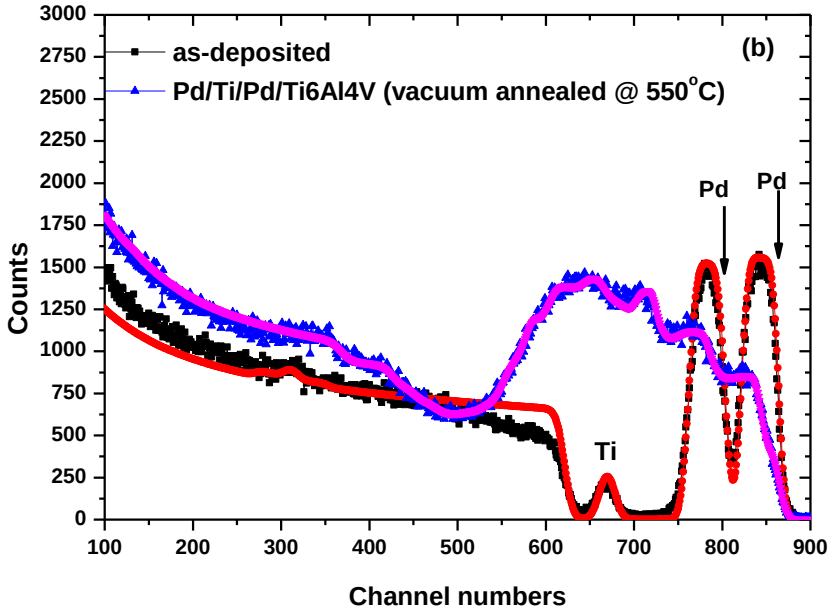

Figure 4.3: *RBS spectra of as-deposited compared to the samples thermally annealed under vacuum on (a) CP-Ti and on (b) Ti6Al4V alloy. The simulations are shown in red and pink solid lines.*

The as-deposited spectra show three peaks corresponding to alpha particles backscattered from Pd and Ti deposited layers, at channels 845 & 775 (for Pd) and 675 (for Ti). The fitting of all spectra was achieved using SIMNRA software version 6.06 [*www.simnra.com*]. There was no signature of intermixing of layers in the as-deposited samples since no tail was noticed in any of the peaks. This indicates that there was no spontaneous reaction during deposition. The thickness of the deposited Pd films were simulated to be ~53.9 nm (surface layer) and ~47.6 nm (at the interface with the substrate). The sandwiched Ti thin film between the Pd layers was found to have reacted with oxygen with a stoichiometry of 35 at.% Ti and 65 at.% O. The simulated thickness shows a disagreement with that obtained by the deposition quartz crystal monitor which recorded 51 nm on both Pd thin film. Curiously, the buried Pd layer seems to be underestimated while the one on the surface seemed to be overestimated. However, the calculated error is in the 5 – 6% bracket.

The shapes of RBS spectra of both vacuum annealed samples suggested intermixing of layers as shown by the decreased counts of Pd on the surface while the counts increased deeper in the bulk between 490 and 750 channel numbers. This indicated the instability of the system at 550 ^{o}C as Pd layers intermixed with the sandwiched Ti deposited film and there is even evidence of interfacial diffusion between the substrate and the buried deposited layer in both systems. Simulation results indicated the phase with the stoichiometry of 33 at.% Pd and 67 at.% Ti. The presence of oxygen in all samples was observed, in agreement with XRD results which confirmed the presence of TiO_2.

DataFurnace software [4.8] was used to convert the RBS spectra into depth profile displayed in figure 4.4 (a-f). In both cases of the as-deposited samples on CP-Ti and Ti6Al4V, Pd (in fig. 4.4(a)) and Ti (in fig. 4.4(b)) peaks are clearly seen with no sign of intermixing. The as-deposited Ti (in fig4.4 (b)) is low in atomic percentage due to oxidation as mentioned. However, in both cases of the thermally annealed samples on CP-Ti (c-d) and Ti6Al4V (e-f), the profiles indicated that Pd atoms diffused inwardly and reacted with Ti to form the $PdTi_2$ phase previously observed in our XRD results. The Ti substrate that was well defined in figure 4.4(b) has dropped from 100 at.% to lower values in most of the original depth profile (see fig. 4.4 (d and f)).

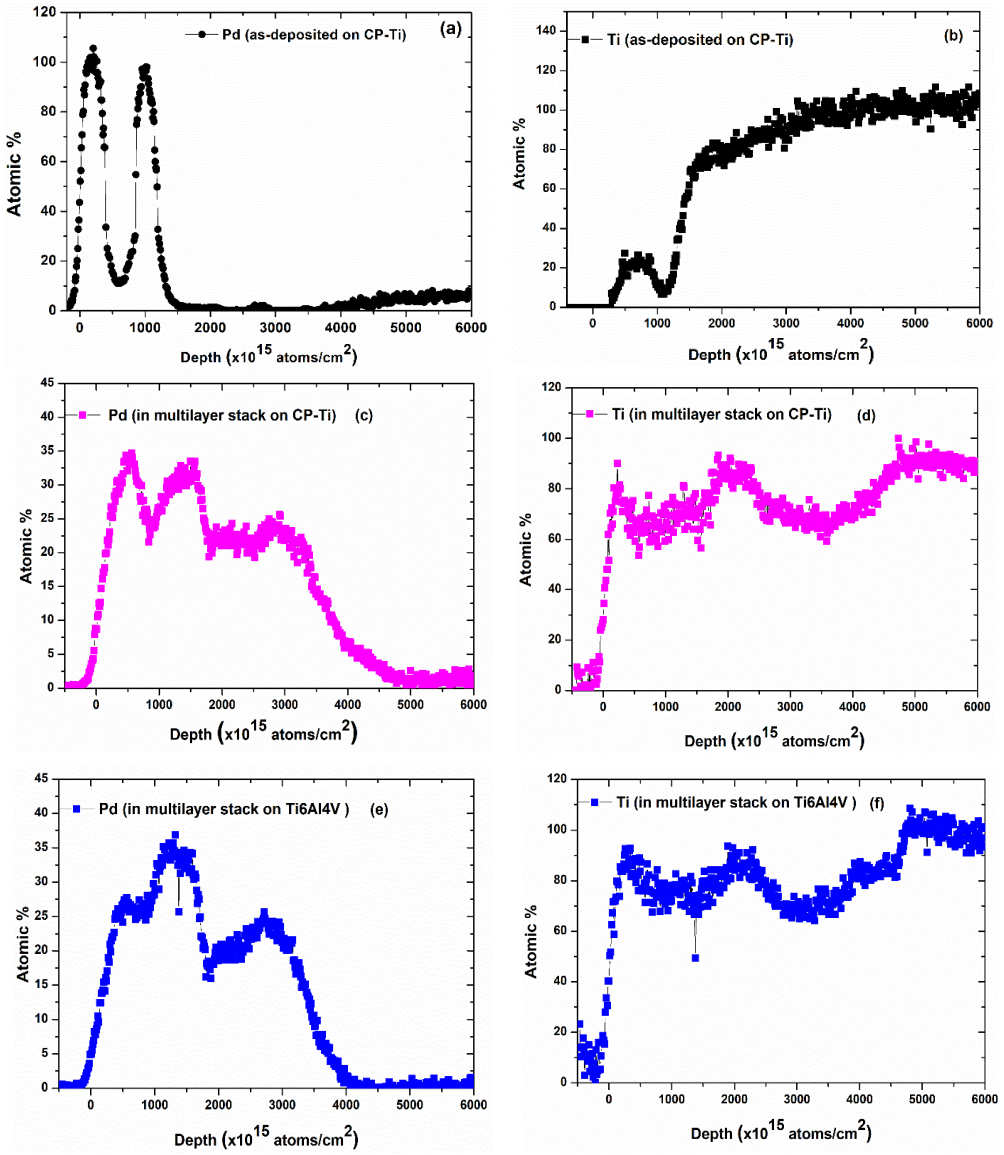

Figure 4.4: *Elemental depth profiles of Pd (left pane) and Ti (right pane) (a-b) in as-deposited samples compared to those samples annealed under H_2(15%)/Ar(85%) gas mixture; (c-d) on CP-Ti and (e-f) on Ti6Al4V substrates.*

To further investigate the inter-diffusion and stoichiometric evolution, in-situ real-time RBS was conducted using 3 MeV He^{++} ions on one sample. The sample was mounted on a flat copper surface heating stage with a thermocouple mounted at the back. The thermal

annealing was carried out with linear temperature ramping from 160 °C to 600 °C at a rate of 3 °C per minute. Figure 4.5 display in-situ real-time RBS spectra showing a colour coded plot of the total spectra monitored through the temperature ramp; the spectra were recorded every 30 seconds. The dwell time at 600 °C was 10 minutes before cooling down back to room temperature.

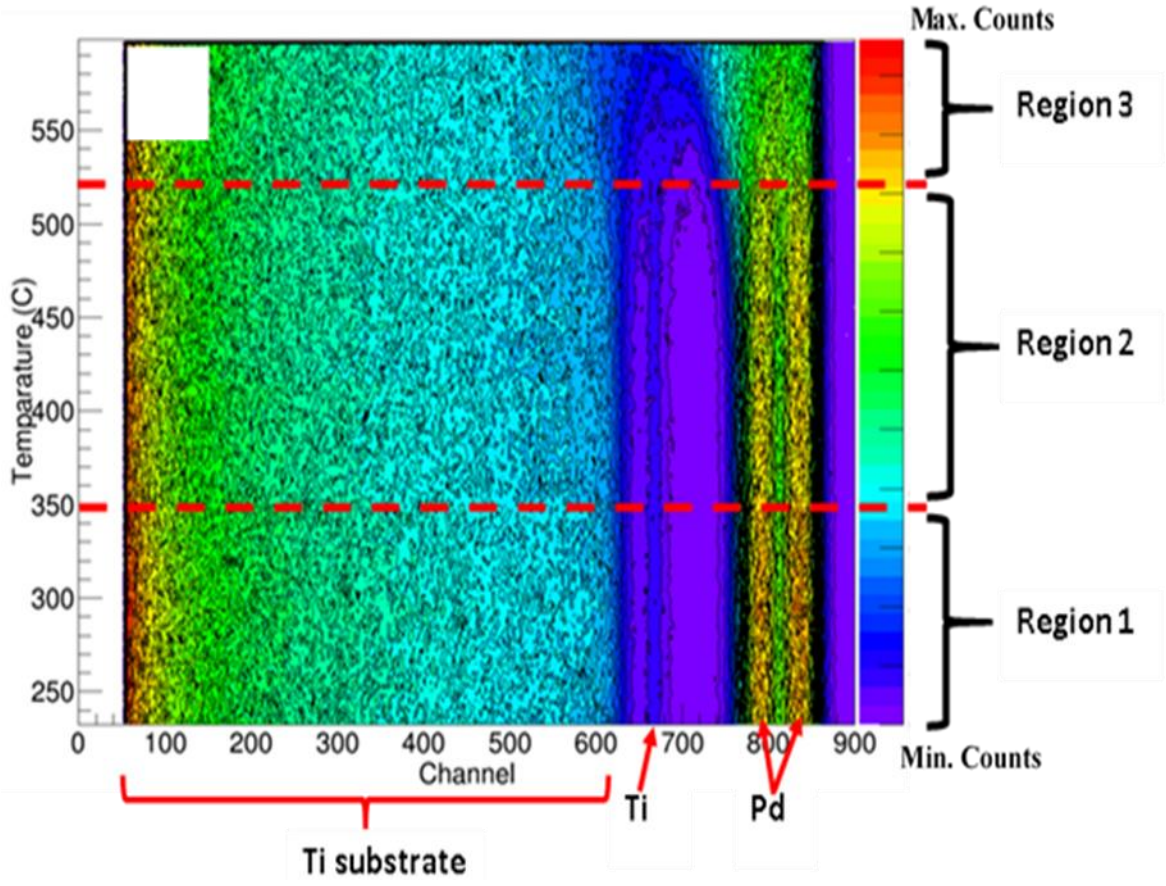

Figure 4.5: *In-situ real-time RBS colour coded plot of the total spectra collected from room temperature to 600 °C on an as- deposited sample.*

For better discussion of the results, figure 4.5 has been divided into three regions and the following conclusion was drawn.

Region (1): Monitoring the colour code (that corresponds to the number of counts) of the deposited Ti and Pd layers, it is clear that there was no change within this

temperature range; it can therefore be concluded that there was no reaction nor intermixing of layers i.e. the system was thermally stable.

Region (2): The colour of the deposited Pd layers changed slightly from reddish to yellowish; this was interpreted as a start of the reactions and /or intermixing between Pd atoms and those of Ti. According to the phase diagram [4.3] and work reported by Tisone et al [4.9], the stable $PdTi_2$ and metastable Pd_3Ti phases co-exist in the temperature range ~350 - 520 ^oC. The metastable Pd_3Ti phase normally starts to vanish at around 520 ^oC.

Region (3): The individual deposited layers of Pd are not anymore distinguishable instead a clear intermixing with the sandwiched deposited Ti layer was noted. At the same time, the monitoring of the signal originating from the Ti deposited layer (between 600 and 700 channel numbers) shows also a mixing with the neighbouring Pd deposited layers. Since XRD results detected only $PdTi_2$ phase at 550 ^oC in addition to α-Ti and Pd peaks, it was concluded that the metastable phase Pd_3Ti was completed consumed in favour of $PdTi_2$.

4.3 Hydrogenation under H_2(15%)/Ar(85%) gas mixture.

4.3.1 Introduction.

Several groups have reported that a temperature around 550 ^oC is the optimum one for hydrogenation of titanium systems [4.10 - 4.12]. Mazwi [4.10] investigated hydrogenation of titanium from 450 - 650 ^oC and found that the highest H content in their study was obtained at 550 ^oC while Lopez-Suarez et al [4.11] studied hydrogenation of titanium in the temperature range between 150 - 750 ^oC and they reported the highest content at the same temperature of 550 ^oC. Baoguo et al [4.16] also investigated hydrogenation behaviour of Ti-6Al-4V from 250 - 800 ^oC and achieved the highest content at 550 ^oC. Consequently, hydrogenation of Ti-Pd system has been done at 550 ^oC for all investigations in the current study. The catalytic activity of Pd is well document [4.13 - 4.15]. Topic et al [4.16] reported improvement of hydrogenation into bulk Ti when coated with a thin film of Pd. In this study, palladium thin films have been used as catalyst to split molecular hydrogen into atomic H and thus allow its adsorption and diffusion in the bulk of Ti or Ti alloy investigated for their hydrogen storage capacity. The ambient under which the hydrogenation is done, plays an important role in both hydrogenation and the stability of the hydrogen's absorbing system. The vacuum annealing of Ti-Pd system is observed to result in the interdiffusion of the respective elements in the system [4.15]; the annealing under pure H_2 delays the interdiffusion up to high temperatures [4.16] while the use of H_2/Ar gas mixture results in early interdiffusion between Ti and Pd [4.17]. Therefore the Pd/Ti/Pd triple layer system onto Ti and Ti6Al4V substrates were annealed under three atmospheres (vacuum, H_2/Ar gas mixture and pure H_2) in order to investigate both the phase formation and the structural stability of the systems at the temperature of 550 ^oC used for hydrogenation as discussed above. SEM, XRD, RBS and ERDA techniques were used to characterise both as-deposited and annealed samples.

4.3.2 Microstructural analysis (H/Ar gas mixture).

Figure 4.6 shows SEM micrographs of Pd(50 nm)/Ti(25 nm)/Pd(50 nm) multilayer stack deposited on (a) CP-Ti, (b) Ti6Al4V alloy, (c) deposited on CP-Ti then annealed under H_2(15%)/Ar(85%) gas mixture at 550 ^oC for 2 hours and (d) deposited on Ti6Al4V alloy then annealed under H_2(15%)/Ar(85%) gas mixture at 550 ^oC for 2 hours. As-deposited samples on both CP-Ti and Ti6Al4V alloy, showed relatively a homogeneous and smooth surface.

In contrast, the surface of annealed samples on both CP-Ti and Ti6Al4V alloy substrates, displayed large interconnected crystals with distinguishable grain boundaries. The evident growth of a crystalline structure during annealing suggests that the deposited films have intermixed as it will be confirmed by RBS.

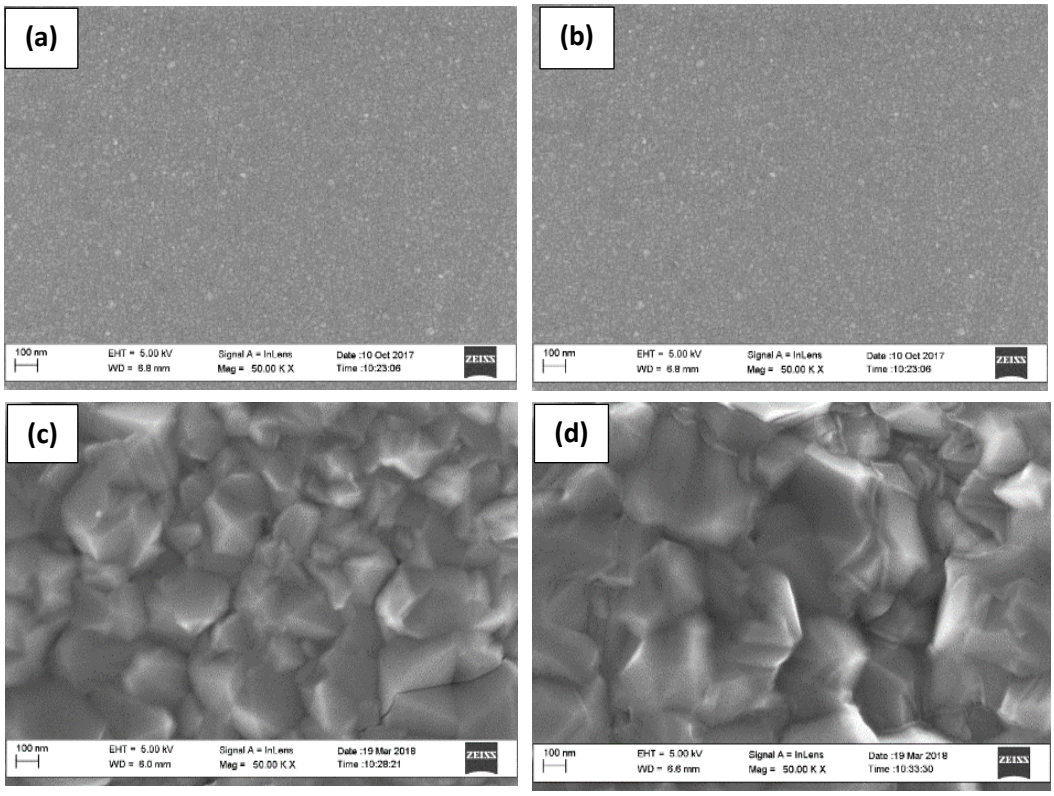

Figure 4.6: *SEM micrographs of (a-b) as deposited samples, (c-d) thermal annealed sample at 550 ^oC for 2 hours under H_2(15%)/Ar(85%) gas mixture on CP-Ti and Ti6Al4V alloy substrates.*

4.3.3 Crystal structure and phase transformation.

Figure 4.7 displays X-rays diffraction patterns of the as-deposited Pd(50 nm)/Ti(25 nm)/Pd(50 nm) multilayer stack on (a) CP-Ti and on (b) Ti6Al4V alloy, plotted together with the ones of samples annealed for 2 hours under H_2(15%)/Ar(85%) gas mixture at 550 ^oC on CP-Ti and Ti6Al4V alloy. For comparison, the patterns of the Ti and Ti6Al4V substrates as-received are given on the figure.

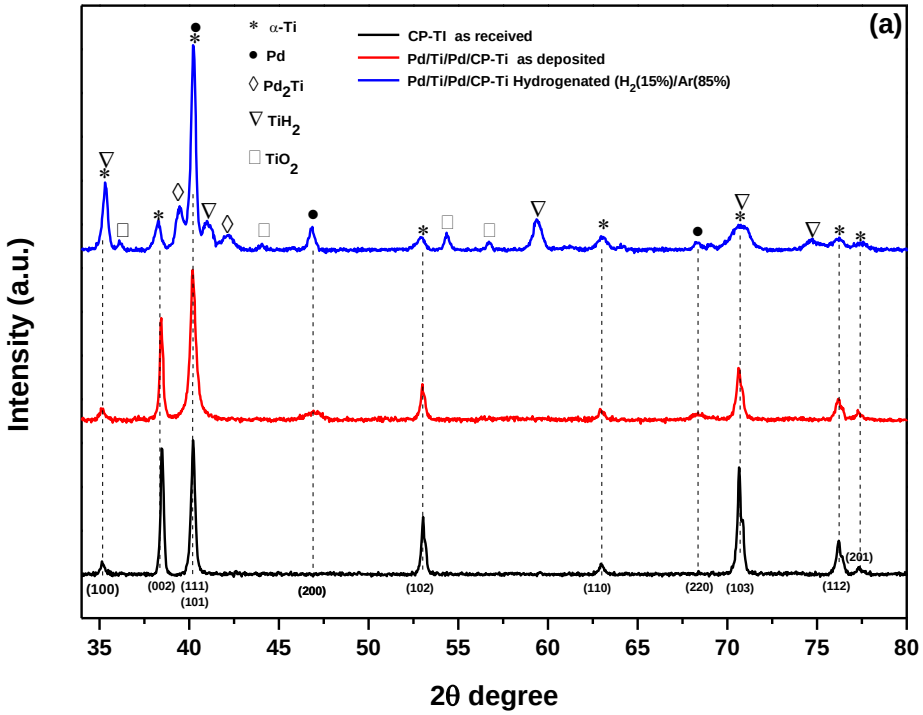

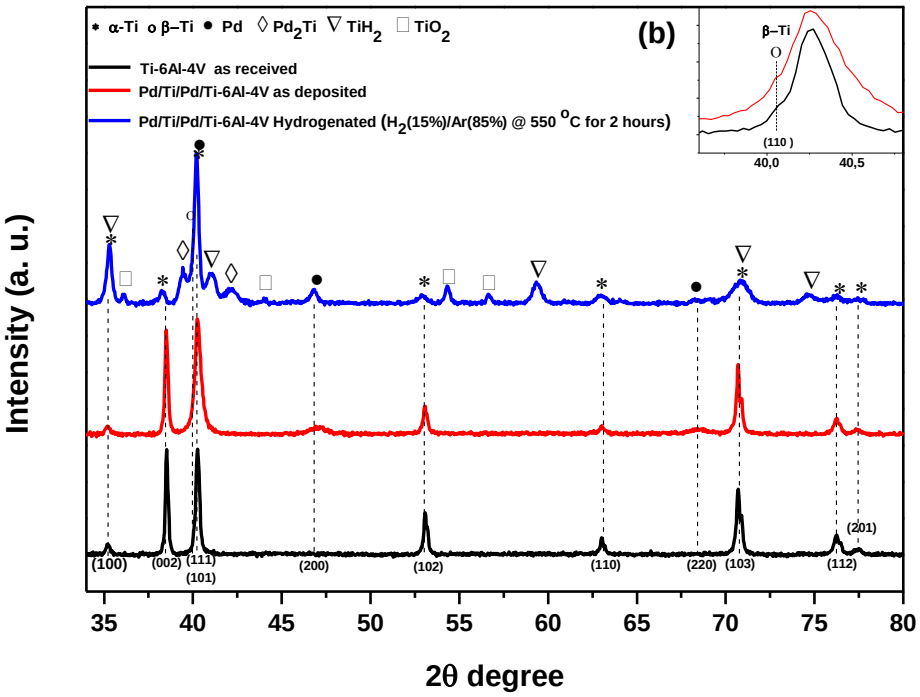

Figure 4.7: *XRD patterns of (a) as-received, as-deposited and annealed under H_2(15%)/Ar(85%) gas mixture atmosphere, on CP-Ti substrate and (b) those of as-received, as-deposited and annealed under H_2(15%)/Ar(85%) atmosphere, on Ti6Al4V alloy substrate.*

As it was noted earlier in section 4.2 when discussing XRD results of samples annealed in vacuum, the as-received CP-Ti and Ti6Al4V alloy display peaks corresponding to the hexagonal α-Ti phase (pattern no: 00-044-1294) with lattice parameters a = 2.95 Å and c = 4.68 Å. An additional peak corresponding to β-Ti phase (pattern no: 00-044-1288) with lattice parameters a = 3.31 Å was observed in Ti6Al4V alloy (please see the insert on fig. 4.7(b)). The as-deposited samples in both systems show, as expected, diffraction peaks corresponding to face-centered cubic (FCC) Pd (pattern no: 00-046-1043) with lattice parameters a = 3.89 Å.

In addition, from the samples annealed in the presence of H_2(15%)/Ar(85%) gas mixture, XRD spectra in both CP-Ti and Ti6Al4V alloy systems, show the presence of Ti hydride, the face-centered cubic (FCC) TiH_2 (pattern no: 00-025-0982) with lattice parameters a = 4.45 Å.

It might be also that some H were incorporated in the Pd network as a solid state solution; however, such H will go un-noticed by XRD.

Furthermore, the presence of body-centred tetragonal Pd_2Ti (pattern no: 00-021-0610) with lattice parameters $a = 3.24$ Å and $c = 8.480$ Å was observed. The Pd_2Ti phase in the H_2(15%)/Ar(85%) gas mixture annealed samples indicates the atomic inter-diffusion between the deposited layers and possibly with the substrate. This is a sign of instability of the system at 550 ^oC under the gas mixture atmosphere, in agreement with the work of Topic et al [4.17] and Fukai [4.18]. TiO_2 compound was also observed in the samples hydrogenated under this atmosphere suggesting either some traces of oxygen impurity in the mixture and / or a post-oxidation effect due to a rough texture of these films. The presence of Pd-hydride was not noted in spite of the two Pd layers in the system contrary to the reports of Fujimoto et al [4.16] and Adams et al [4.19]. This observation may not mean the absence of Pd-hydrides however as it is possible that this type of hydride may be present in an amorphous state or solid state solution and therefore may not have been detected.

Regardless of the presence of the Pd catalyst for effective dissociation of molecular hydrogen, TiO_2 has a detrimental effect of acting a barrier to the atomic H diffusion.

4.3.4 RBS spectral analysis.

As mentioned earlier in section 4.2, the probed depth was 4.7 μm following SRIM simulations. Figure 4.8 shows RBS spectra of the as-deposited Pd(50 nm)/Ti(25 nm)/Pd(50 nm) multilayer stack on (a) CP-Ti and on (b) Ti6Al4V alloy, overlaid with spectra of the annealed samples for 2 hours under H_2(15%)/Ar(85%) gas mixture at 550 ^oC. The details about the gas flow were given in the experimental section. As it can be seen in the figure, the edge of the RBS peaks for the Pd deposited layers are situated at channel number 845 (for the

top layer) and 775 (for the interfacial layer with the substrate) while the one of the RBS peak for the sandwiched deposited Ti film is at channel number 675. The fitting of all spectra was achieved using SIMNRA; the simulated spectra are overlaid on the experimental graphs. There was no sign of intermixing of deposited layers in the as-deposited samples as no tail was observed in any of their respective RBS peaks.

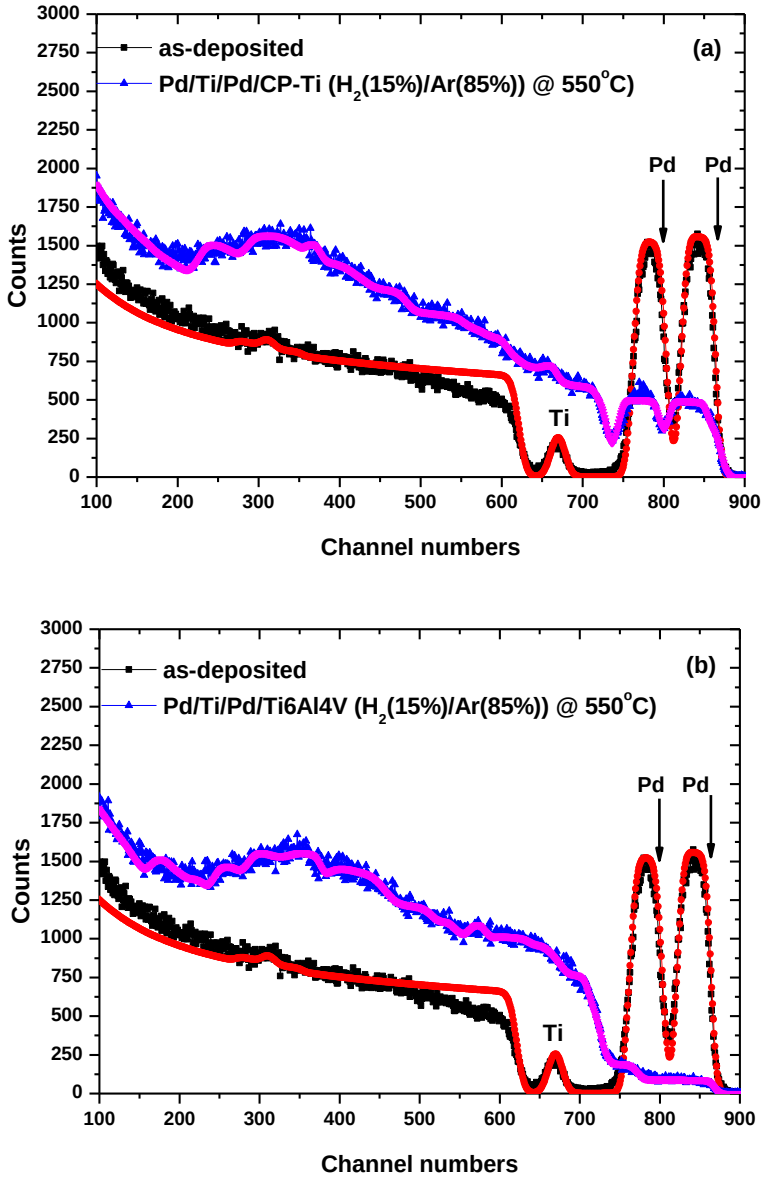

Figure 4.8: *RBS spectra of as-deposited compared to the samples thermally annealed under H_2(15%)/Ar(85%) gas mixture on (a) CP-Ti and on (b) Ti6Al4V alloy. The simulations are shown in red and pink solid lines.*

It was noted on the spectra of the annealed samples, that the yield of the deposited Pd layers decreases significantly in the CP-Ti system and it does almost disappear in the Ti6Al4V alloy system while the part of the spectrum corresponding to both deposited Ti film and substrate, increased significantly in counts (in both systems); this is interpreted as the inwards diffusion of Pd atoms into both the Ti deposited layer and substrates. The simulations showed a stoichiometry of 65 at.% Pd and 35 at.% Ti which corresponds on the $PdTi_2$ phase observed by XRD. The presence of oxygen was observed in all samples; this is in agreement with XRD results that confirmed the presence of TiO_2 phase in both systems.

Figure 4.9 (a-f) presents the plots of elemental depth profiles (left pane for Pd and right pane for Ti), obtained by the use of DataFurnace software. Obviously in as-deposited state, there was no reaction or intermixing of the deposited films; thus the as-deposited profiles of Pd and Ti will be similar in stacks on both substrates (in fig. 4.9 (a-b)), only the Pd and Ti depth profile on CP-Ti, are given as a typical examples). The as-deposited Ti (in fig4.9 (b)) is low in atomic percentage due to oxidation. However, the interdiffusion of layers was apparent in the annealed samples in both systems. The profiles indicated that Pd atoms diffused inwardly towards the substrate; this is in agreement with XRD results that showed the presence of Pd_2Ti. The annealing in both systems under H_2(15%)/Ar(85%) gas mixture atmosphere induced inwards diffusion of Pd atoms and intermixing of the three deposited layers and this was noted to be more pronounced in the Ti6Al4V alloy system.

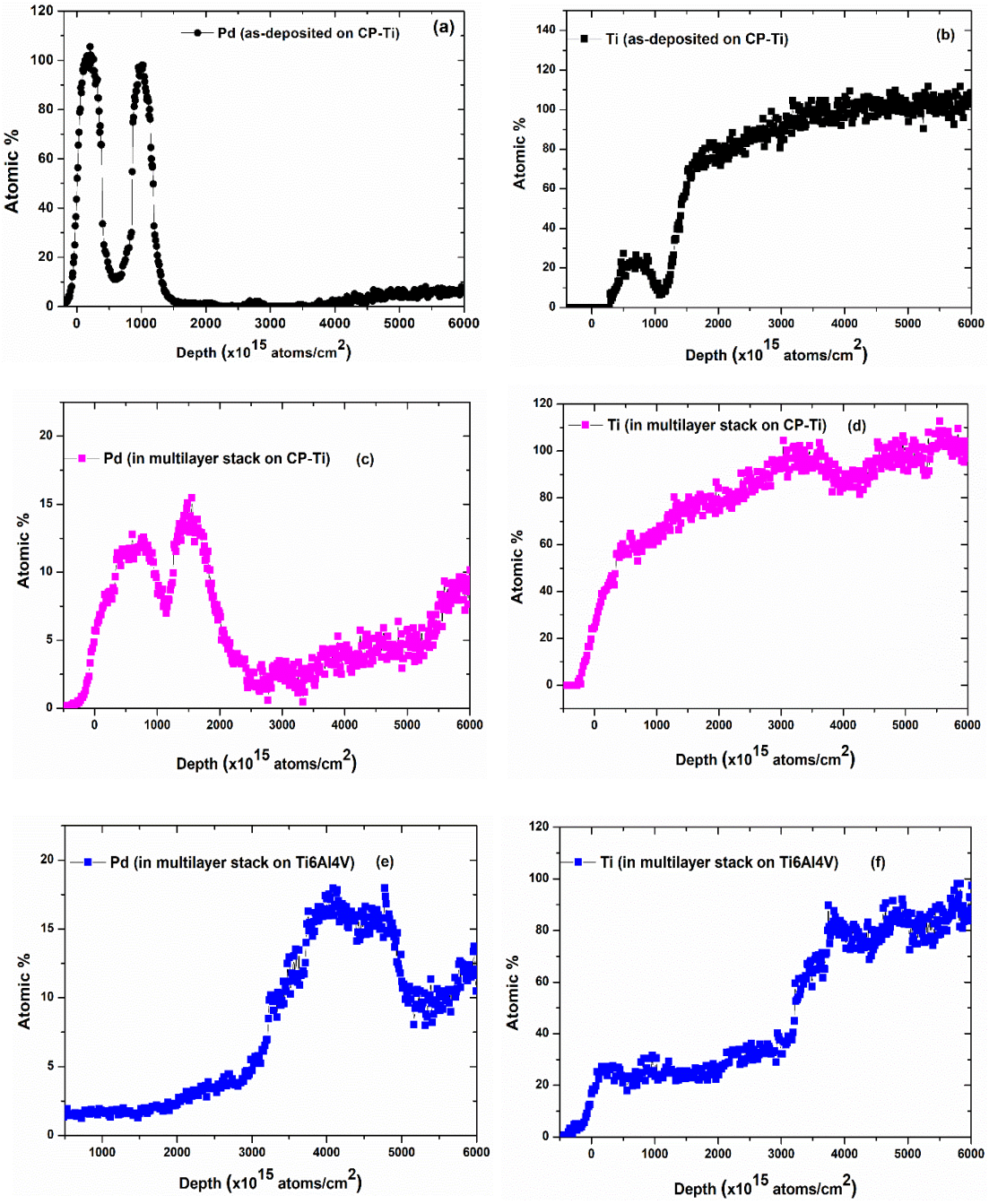

Figure 4.9: *Elemental depth profiles of Pd (left pane) and Ti (right pane) (a-b) in as-deposited samples compared to those samples annealed under H_2(15%)/Ar(85%) gas mixture; (c-d) on CP-Ti and (e-f) on Ti6Al4V substrates.*

4.3.5 ERDA studies.

The probed depth in this part of the investigation was also calculated using SRIM2013 software. In the ERD experiment, the sample is tilted 75^{o} towards the detector, consequently the He++ penetration range was calculated to be 1.92 µm. Figure 4.10 shows ERDA spectra of samples annealed under H_2(15%)/Ar(85%) gas mixture at 550 ^{o}C for two hours on Pd/Ti/Pd/CP-Ti and Pd/Ti/Pd/Ti6Al4V multilayer system. It can be observed that H concentration differed from system to system. For example, from the surface up to 750 and region between 700 to 450 channels numbers, the H content was more in the CP-Ti system as compared to on Ti6Al4V system. Meanwhile in the region deeper in the bulk, more H content was higher in the Ti6Al4V system than in the CP-Ti system, especially below 450 channel numbers.

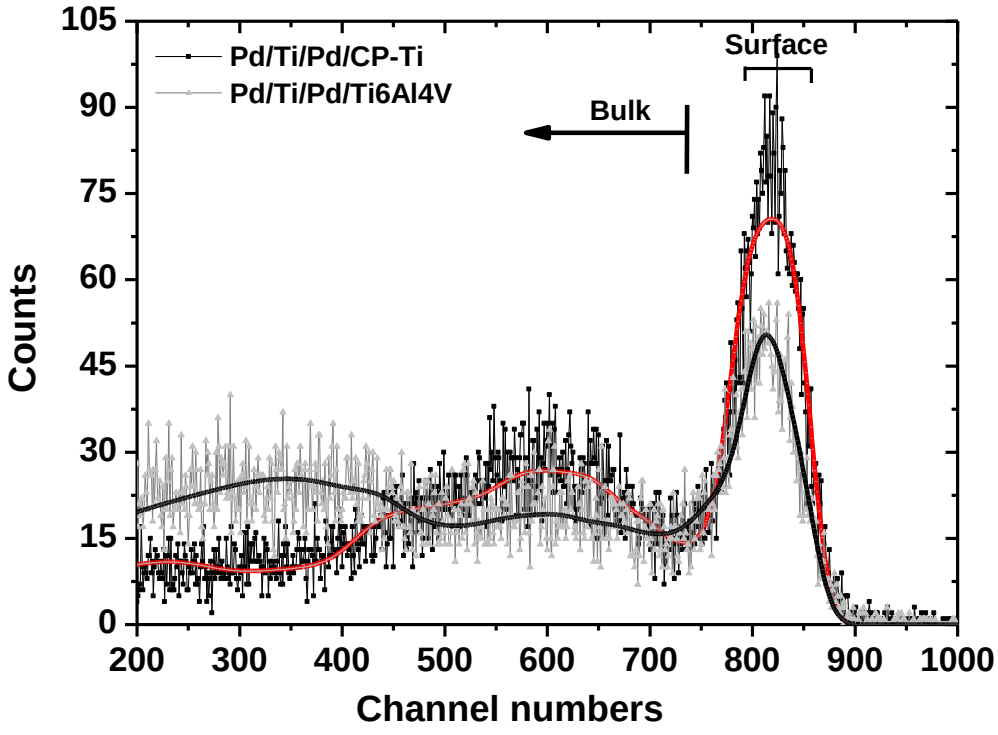

Figure 4.10: *ERDA spectra of annealed samples under H_2(15%)/Ar(85%) gas mixture atmosphere. Square solid points referees to Pd/Ti/Pd/CP-Ti; triangle solid points referees to Pd/Ti/Pd/Ti6Al4V. The simulated spectra are overlaid.*

Figure 4.11 display the hydrogen profiles in both samples. The average content of absorbed H over probed depth of ~750 $\times 10^{15}$ atoms/cm^2 from the surface was found to be ~ 6 at.% in CP-Ti and ~4 at.% in Ti6Al4V alloy. The average content in the bulk beyond 750×10^{15} atoms/cm^2 was found to be ~3.5 at.% in CP-Ti and 6.2 at.% in Ti6Al4V. The region above 2000×10^{15} atoms/cm^2 displayed an increase in Ti6Al4V was observed while CP-Ti showed decrease of H in the bulk.

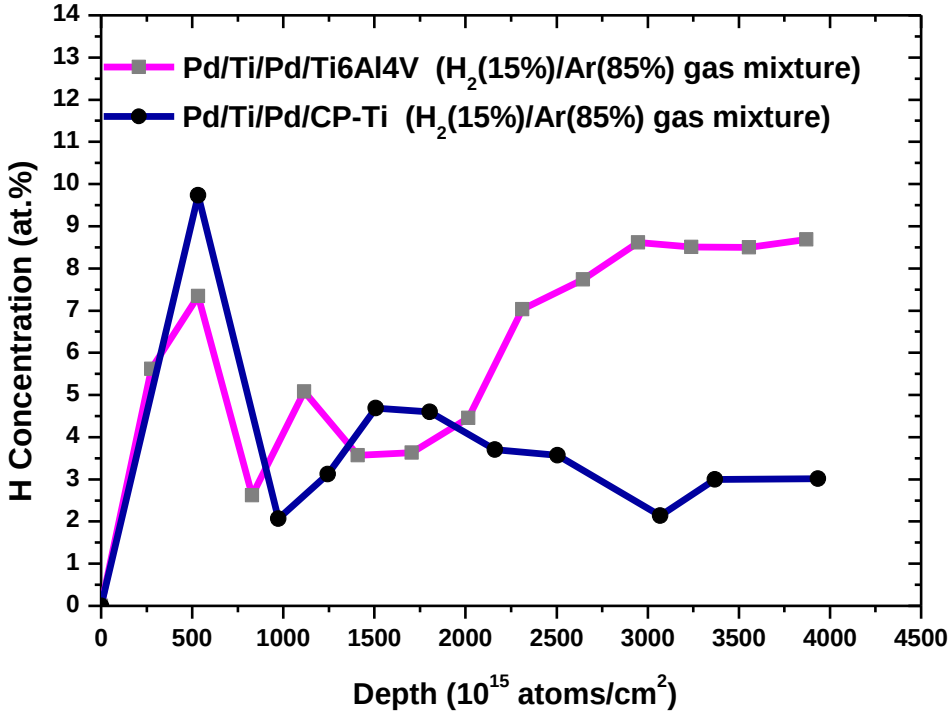

Figure 4.11: *H profile from the samples hydrogenated under H_2(15%)/Ar(85%) gas mixture.*

Even though the average content of the absorbed H was low as compared to the one reported in the literature [4.17, 4.18] these two systems presented a positive response to hydrogen absorption. One of the reasons for low hydrogen absorption into Ti has been reported by Topic et al [4.20] to be the presence of oxygen on the metal surface.

4.4 Hydrogenation under pure H_2 gas.

4.4.1 Microstructural analysis (pure H_2 gas).

Figure 4.12 shows SEM micrographs of Pd(50 nm)/Ti(25 nm)/Pd(50 nm) multilayer stack deposited on (a) CP-Ti, (b) Ti6Al4V alloy, (c) deposited on CP-Ti then annealed under pure H_2 gas at 550 ^oC for 1 hour and (d) deposited on Ti6Al4V alloy then annealed under pure H_2 gas at 550 ^oC for 1 hour. In both cases of CP-Ti and Ti6Al4V alloy, the as-deposited and hydrogenated samples showed a relatively uniform and smooth surface. The smooth surface during hydrogenation with pure H_2 gas suggests that the deposited films have not intermixed as it will be confirmed by RBS. Morphological changes observed in samples hydrogenated under H_2/Ar could be attributed to the presence of Ar in the gas mixture during annealing.

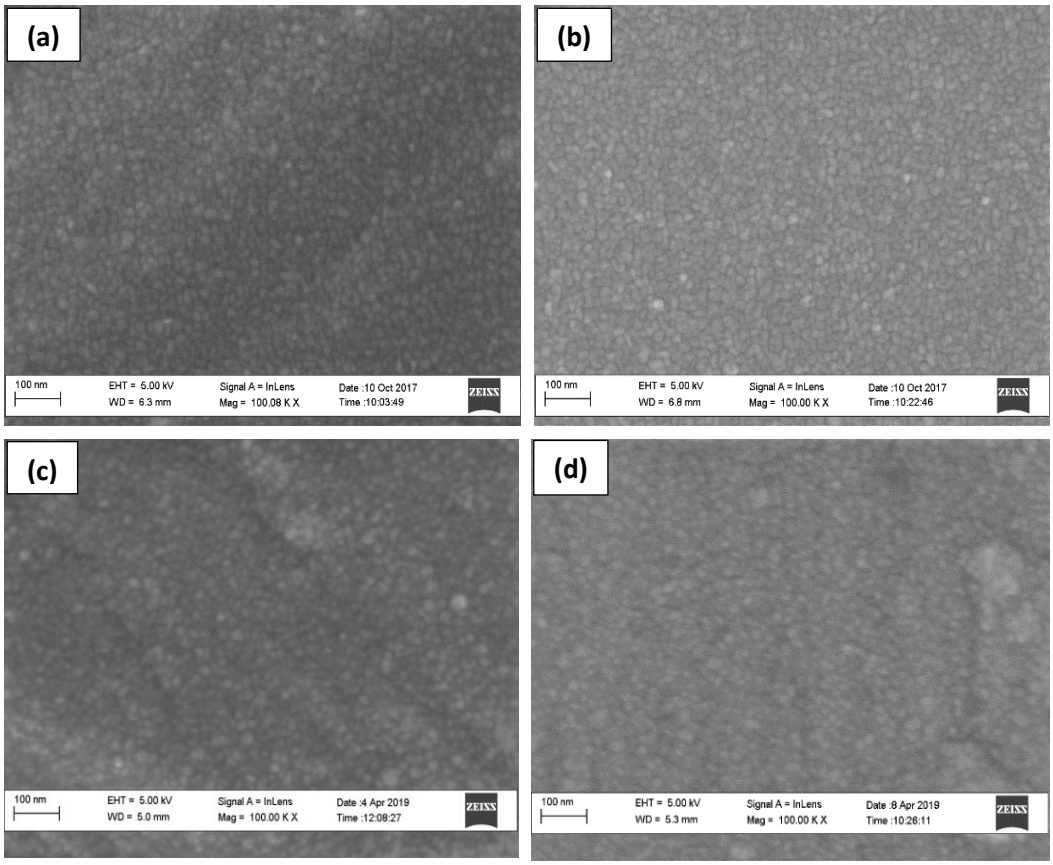

Figure 4.12: *SEM micrographs of (a-b) as deposited samples, (c-d) thermal annealed sample at 550 ^oC for one hours under pure H_2 gas flow on CP-Ti and Ti6Al4V alloy substrates.*

As noted earlier SEM is a surface technique for morphological investigation and it cannot provide further information on the structural transformation in the bulk; therefore, XRD was used for phase analysis.

4.4.2 Crystal structure and phase transformation.

Figure 4.13 shows XRD patterns of the as-deposited Pd(50 nm)/Ti(25 nm)/Pd(50 nm) multilayer stack on (a) CP-Ti and on (b) Ti6Al4V alloy plotted together with the annealed samples for one hour under pure H_2 gas at 550 ^oC on CP-Ti and on Ti6Al4V alloy. For comparison, the patterns of the Ti and Ti6Al4V substrates as-received are given on the figure.

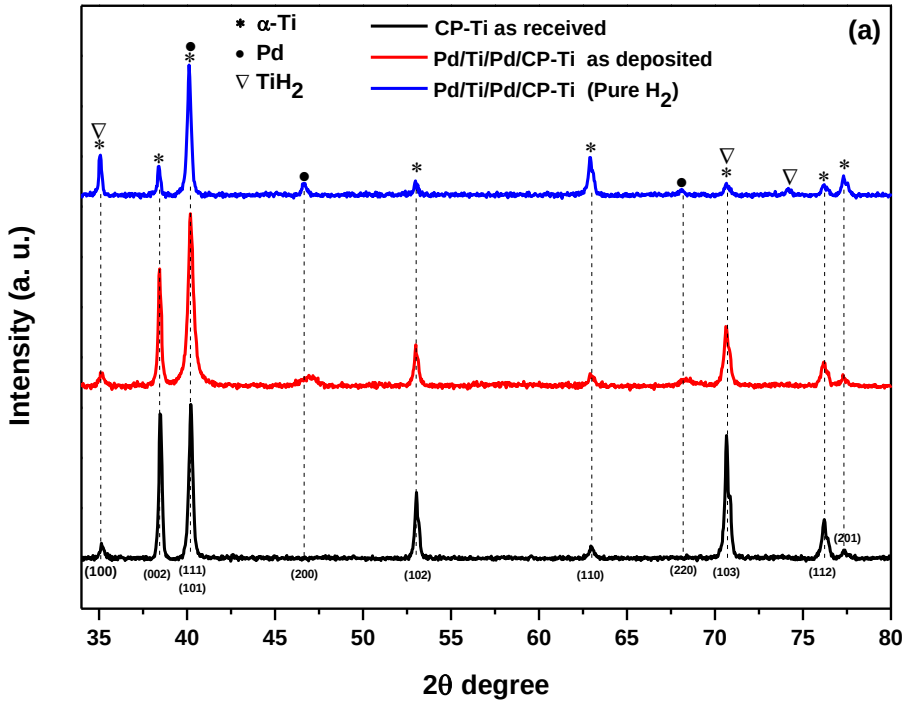

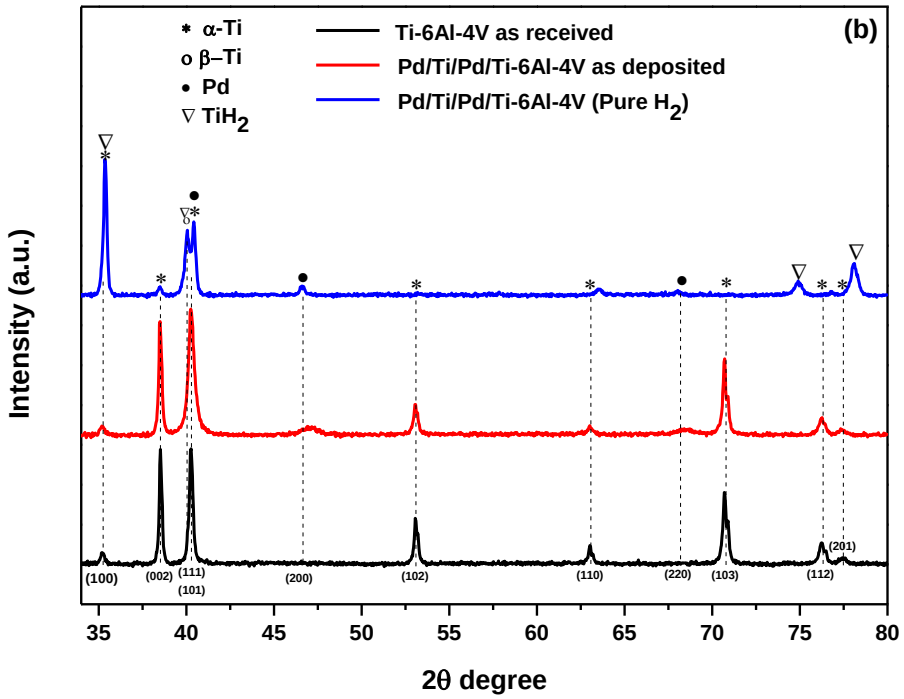

Figure 4.13: *XRD patterns of (a) as-received, as-deposited and annealed under pure H_2 atmosphere, on CP-Ti substrate and (b) those of as-received, as-deposited and annealed under pure H_2 atmosphere, on Ti6Al4V alloy substrate.*

As it was noted earlier in section 4.2 and 4.3 when discussing XRD results, the as-received CP-Ti and Ti6Al4V alloy display peaks corresponding to the hexagonal α-Ti phase (pattern no: 00-044-1294), and space group *P63/mmc (194)* with lattice parameters a = 2.95 Å and c = 4.68 Å. An additional peak corresponding to β-Ti phase (pattern no: 00-044-1288) with lattice parameters a = 3.31 Å was observed in Ti6Al4V. The as-deposited samples in both systems show, as expected, diffraction peaks corresponding to face-centered cubic (FCC) Pd (pattern no: 00-046-1043) with lattice parameters a = 3.89 Å.

However, upon annealing at 550 ^{o}C in the presence of pure H_2 gas, XRD spectra of system on both CP-Ti and Ti6Al4V alloy, showed the presence of Ti hydride, the face-centered cubic (FCC) TiH_2 (pattern no: 00-025-0982) with lattice parameters a = 4.45 Å, in addition to Pd,

α- and β-phases observed on the as-deposited samples. No observation of the Pd-Ti phase as previously noted in the H_2(15%)/Ar(85%) gas mixture, indicating the absence of atomic inter-diffusion. To further investigate the absence of the inter-diffusion and the absence of the formation of compounds, RBS was used.

4.4.3 RBS spectral analysis.

As mentioned earlier in section 4.2, the probed depth was 4.7 μm following SRIM simulations. Figure 4.14 shows RBS spectra of the 550 °C annealed Pd(50 nm)/Ti(25 nm)/Pd(50 nm) multilayer stack on CP-Ti and on Ti6Al4V alloy for one hour under pure H_2 gas. A noticeable beneficial effect of annealing in pure H_2 is the preservation of the integrity of the deposited catalyst layers; this is essential if the system has to be used in many cycles of loading and releasing hydrogen. As a consequence, the only new phase formed was TiH_2 as it was observed by XRD in figure 4.13.

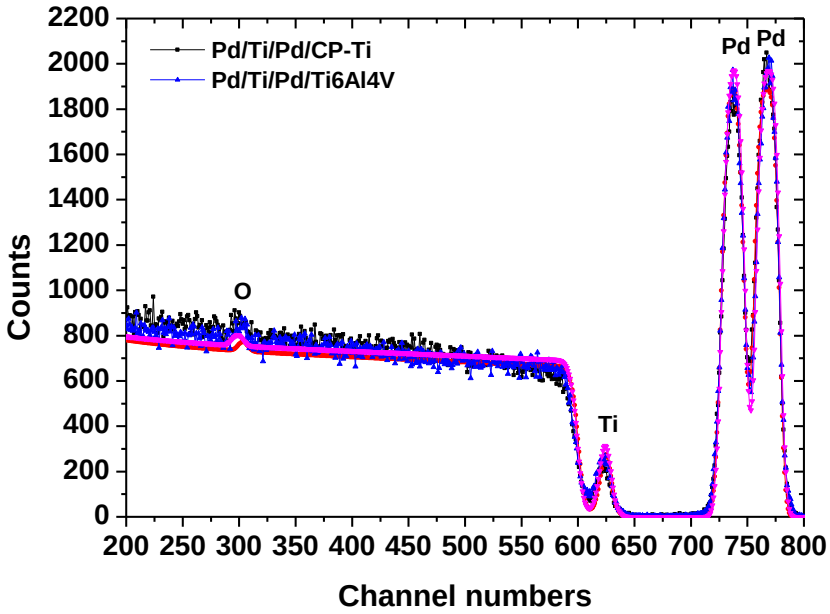

Figure 4.14: *RBS spectra of samples thermally annealed under pure H_2 at 550 °C for one hour on CP-Ti and on Ti6Al4V alloy substrates. simulated spectra are also overlaid.*

It appears that the split and abundant atomic hydrogen diffuse in the interstitial sites of the Ti and/ or passivates the available dangling Ti bonds; ultimately under pure H_2 atmosphere, the nature of diffusion is such that the formed TiH_2 acts as a diffusion barrier of the catalyst Pd. These results are pointing directly to the negative impact of hydrogenating under hydrogen gas mixture as observed in the previous section 4.3. They further show the stability of the catalyst during hydrogenation under pure hydrogen since there was no structural transformation.

To confirm the absence of the inter-diffusion, in-situ real-time, RBS was carried out using 3 MeV He^{++} ions on one sample. The sample was mounted on the flat copper surface heating stage with a thermocouple mounted at the back. The thermal annealing was carried out with linear temperature ramping from 160 to 600 °C at 3 °C per minute. Figure 4.15 displays in-situ real-time RBS spectra showing a colour coded plot of total spectra monitored through a temperature ramp from 160 ^oC to 600 ^oC at the rate of 3 ^oC/min; the spectra were recorded every 30 seconds. The dwell time at 600 ^oC was 10 minutes before cooling down back to room temperature.

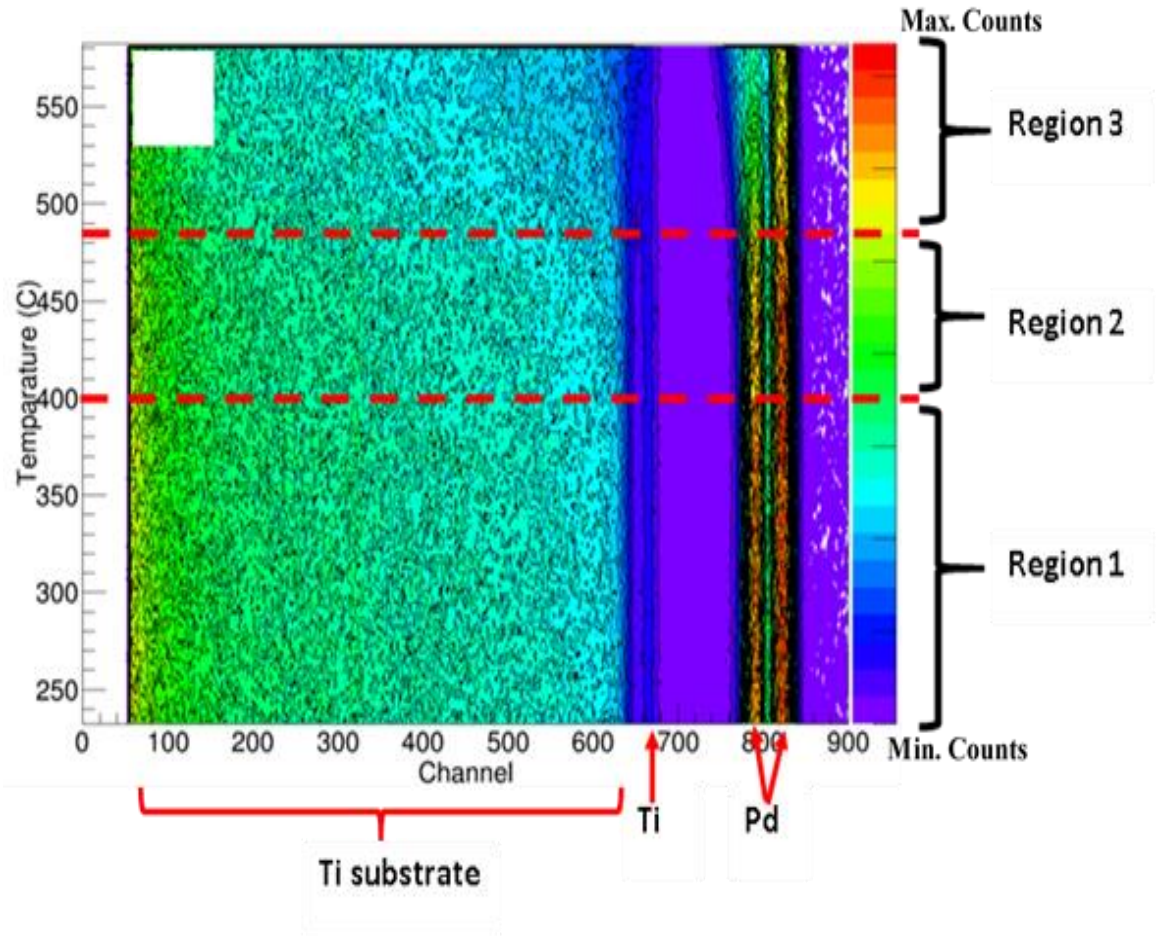

Figure 4.15: *In-situ real-time RBS results showing a colour coded plot of the total spectra collected from room temperature to 600 ^{o}C on Pre-annealed sample in presence of pure hydrogen. Right vertical axis shows time regions (1-3).*

As earlier in similar studies, for better discussion of the results, figure 4.15 has been divided into three regions; the following conclusion was drawn.

Region (1): the sample did not show any reaction up to 400 ^{o}C; the system was thus stable in this temperature range.

Region (2): There is evidence of the decrease in counts of Pd in the layer in contact with the substrate; the top Pd layer at the surface was not affected in this temperature range.

Region (3): The reaction on the Pd buried layer is seen to accelerate; at the same time the surface Pd layer also dropped in counts but at a lesser extent. It was noticed also that the signal in the sandwiched deposited Ti layer is spreading without any noticeable drop in counts. The reactions in region 3 can be summarized and interpreted as follows:

(i) There is a gradual change in color code and spreading of the signal of the Pd buried layer towards the substrate. At the same time, the sub-interface region in the Ti substrate changes in the color code towards lower counts.

(ii) The counts in the sandwiched deposited Ti layer are unaffected.

These observations suggest that there is an interfacial mixing between the buried Pd layer and the Ti substrate across the interface. Our XRD results had indicated the formation of TiH_2 phase that acted as a diffusion barrier hindering Pd atoms from the Pd layer on the surface from diffusing inward as reported by Fujimoto et al [4.16]. The little drop in counts that was observed above 550 ^oC in the Pd surface layer coupled with a stable count in the Ti deposited layer suggest that the Ti layer behaved like a permeable membrane to Pd atoms in this temperature range.

4.4.4 ERDA studies.

As it was noted previously in section 4.3.5, the probed depth could be only limited to a depth less than 1.92 μm. Figure 4.16 shows ERDA spectra of samples annealed under pure H_2 at 550 ^oC for one hour on Pd/Ti/Pd/CP-Ti and on Pd/Ti/PdTi6Al4V multilayer system. The spectra display an enhancement of H absorption on Ti6Al4V as seen by an increase in counts

to 250 from CP-Ti. This enhancement shows the beneficial effect of pure H_2 into Ti6Al4V with α+β phase than CP-Ti with only α-phase.

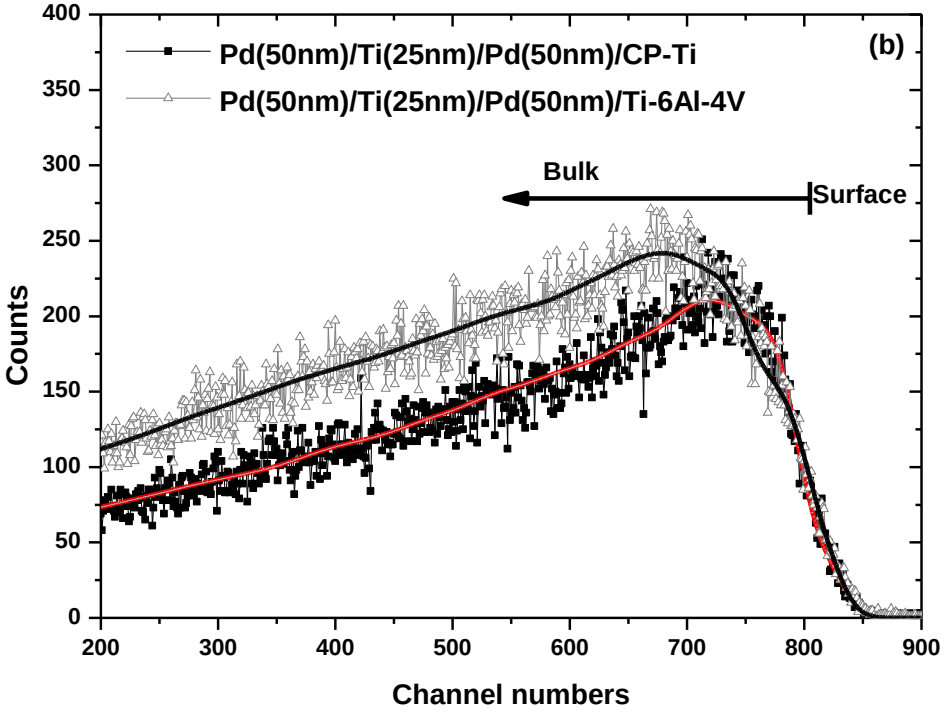

Figure 4.16: *ERDA spectra of annealed samples under pure H_2 atmosphere. Square solid points refer to Pd/Ti/Pd/CP-Ti; triangle solid points referees to Pd/Ti/Pd/Ti6Al4V. The simulated spectra are overlaid.*

Figure 4.17 displays the hydrogen depth profiles in both samples. the average content of absorbed H over the first ~750 $\times 10^{15}$ atoms/cm^2 depth was found to be ~ 33 at.% in both multilayer system. The average content in the bulk beyond 750×10^{15} atoms/cm^2 was found to be ~19.5 at.% H on CP-Ti system and ~25.7 at.% H on Ti6Al4V system. The reason for higher hydrogen in the Ti-6Al-4V is due to the fact that it is composed of β-phase (BCC structure) which are surrounding the α-phase (HCP). The advantage of BCC structure in the Ti-6Al-4V makes it easier for hydrogen atoms to enter the crystalline structure and fit in the interstitial sites of the crystal [4.21]. The BCC structure has six octahedral sites and 12

tetrahedral site per unit cell where hydrogen can fit, and these sites are three times more than the ones found in HCP and FCC lattice [4.22, 4.23].

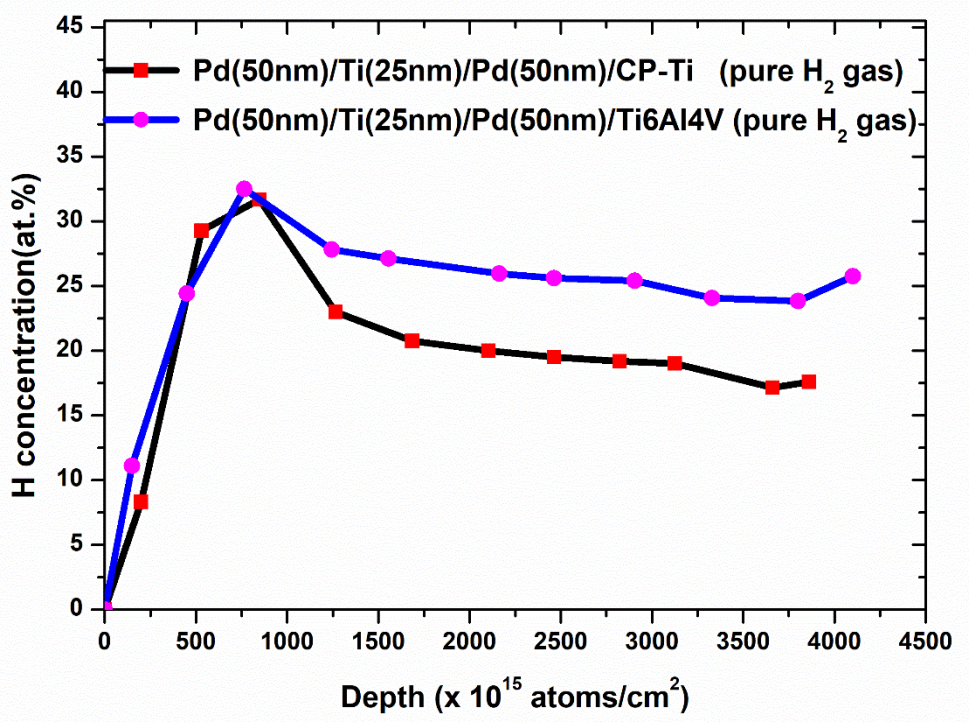

Figure 4.17: *H profile from the sample hydrogenated with pure hydrogen.*

4.5 Effect of the thickness of catalyst on hydrogen capacity of Ti-Pd systems.

Palladium plays a very crucial role in the hydrogenation process. As per previous reports [4.15, 4.16, and 4.19], it acts as a catalyst to split molecular to atomic hydrogen. Therefore, it was crucial to investigate the effect of varying Pd thickness in these systems. The samples of Pd(100 nm)/Ti(25 nm)/Pd(100 nm) multilayer stack on CP-Ti and on Ti6Al4V were prepared and annealed at 550 ^{o}C for one hour under pure H_2 gas. ERDA results were compared to those of Pd(50 nm)/Ti(25 nm)/Pd(50 nm) multilayer stack on CP-Ti and on Ti6Al4V annealed under pure H_2 for one hour.

4.5.1 ERDA studies.

As it was noted previously in section 4.3.5, the probed depth was limited to a depth less than 1.92 μm. Figure 4.18 shows ERDA spectra of (a) Pd(100 nm)/Ti(25 nm)/Pd(100 nm) multilayer stack on CP-Ti and on Ti6Al4V compared to (b) Pd(50 nm)/Ti(25 nm)/Pd(50 nm) multilayer stack on CP-Ti and on Ti6Al4V. The system with thicker Pd catalyst showed a decrease in counts compared to the thinner ones in both CP-Ti and Ti6Al4V, which means less hydrogen into the bulk material.

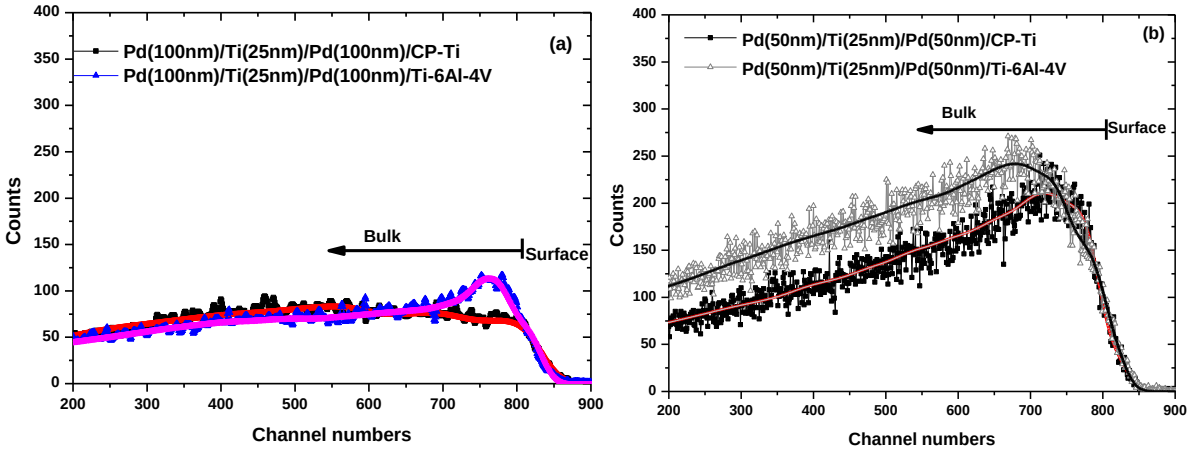

Figure 4.18: *ERDA spectra of samples hydrogenated with pure H_2 at 550 °C for one hours; (a) Pd(100 nm)/Ti(25 nm)/Pd(100 nm) on CP-Ti and Ti6Al4V substrates; (b) Pd(50 nm)/Ti(25 nm)/Pd(50 nm) on CP-Ti and Ti6Al4V substrates.*

Figure 4.19 shows H concentration profile plots extracted from the simulated spectrum in figure 4.18. The average H content probed over depth of 750×10^{15} atoms/cm^2 from the surface was found to be ~10.3 at.% in CP-Ti and to be ~15.1 at.% in Ti6Al4V. In the bulk beyond 750×10^{15} atoms/cm^2 the average H content was found to be ~12.5 at.% in CP-Ti and ~11.2 at.% in the Ti6Al4V.

Figure 4.19 (a) shows the profiles of hydrogen content for stacks grown with thicker Pd catalyst layer. The average H content probed over depth of 750×10^{15} atoms/cm^2 from the surface was found to be ~10.3 at.% in CP-Ti and to be ~15.1 at.% in Ti6Al4V. In the bulk

beyond 750×10^{15} atoms/cm^2 the average H content was found to be ~12.5 at.% in CP-Ti and ~11.2 at.% in the Ti6Al4V. Figure 4.19 (b) displays corresponding profiles for stacks grown with thinner Pd layers. It was noted that almost twice H content was stored when the catalyst was thinner. Although this study is not systematic, since only two thicknesses of the catalyst were probed, our results are consistent with other published reports [4.24] that conclude that the reduction of the thickness catalyst layer in the growth of carbon nanotubes results in faster growth rate.

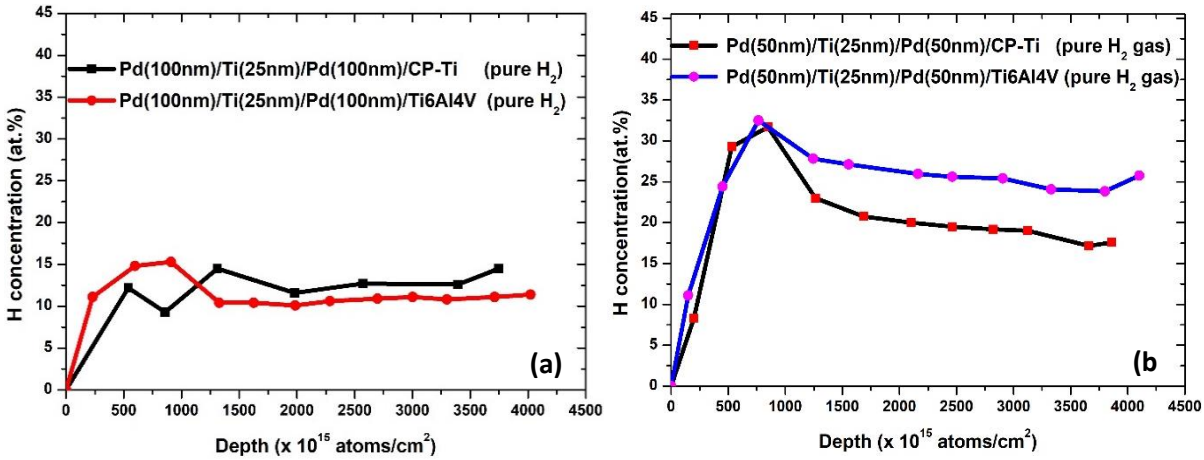

Figure 4.19: *H profile of the samples hydrogenated with pure H_2; (a) Pd(100 nm)/Ti(25 nm)/Pd(100 nm) on CP-Ti and Ti6Al4V compared to those of (b) Pd(50 nm)/Ti(25 nm)/Pd(50 nm) on CP-Ti and Ti6Al4V.*

Poor performance of the systems coated with multilayers of Pd(100 nm)/Ti(25 nm)/Ti(100 nm) could be due to reduced mobility of H atoms permeating the sandwiched the Ti deposited layer. It can be argued also that, given a much longer path before diffusion in the Ti layer, some of the split atomic H have more probability to recombine into molecular H_2 gas and diffuse out of the system.

4.5.2 Microstructural changes' analysis.

Figure 4.20 shows micrographs of Pd(100 nm)/Ti(25 nm)/Pd(100 nm) multilayer stack; (a) the as-deposited films on CP-Ti, (b) the as-deposited films on Ti6Al4V alloy, (c-d) annealed samples for one hour under pure H_2 gas at 550 ^oC on CP-Ti and on Ti6Al4V alloy. The as-deposited films on both substrates showed a smooth and homogeneous surface. As in the case of thinner Pd films in figure 4.12, the hydrogenated thicker Pd films under pure hydrogen, showed sign of etching but the surface modification seems more pronounced. It is not clear, at this stage, if this can be attributed to the blistering by the escaping molecular H_2.

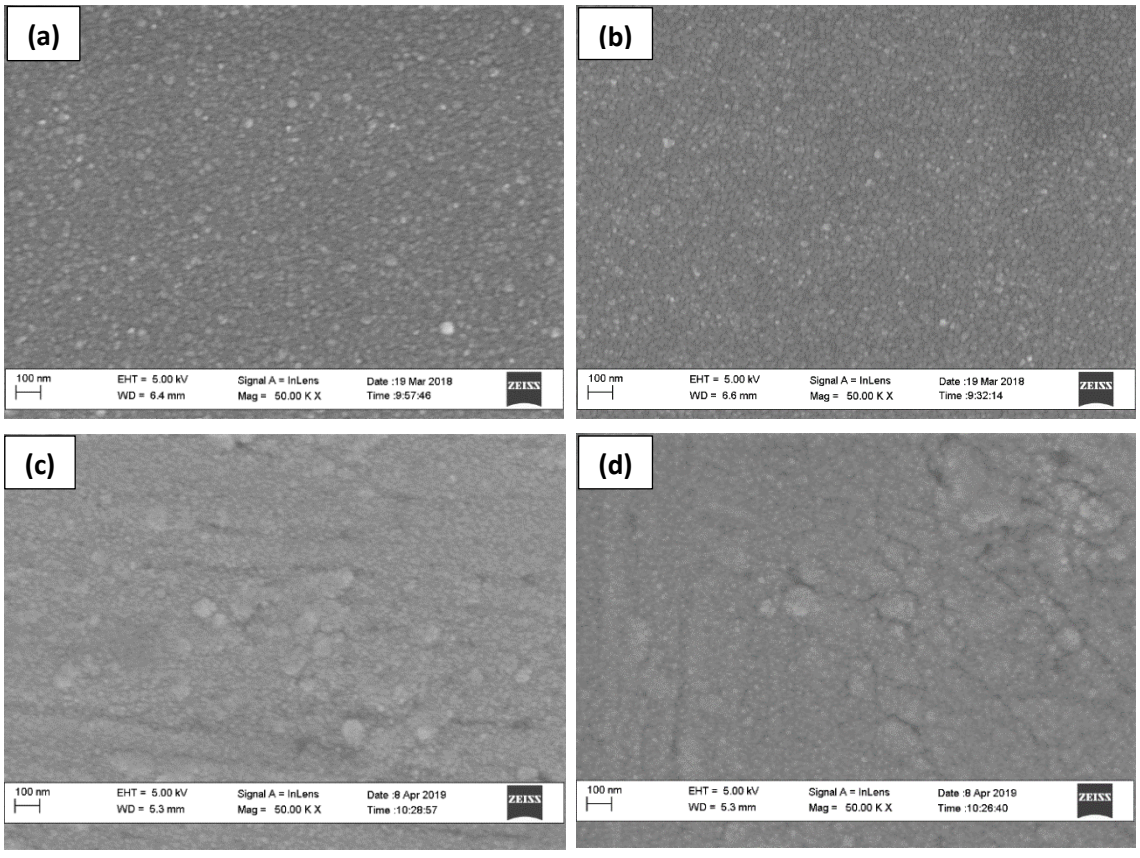

Figure 4.20: *SEM micrographs of (a-b) as deposited samples, (c-d) thermally annealed sample under pure H_2 on CP-Ti and on Ti6Al4V substrates.*

In order to correlate the morphological and structural transformations to phase formation, XRD studies were conducted.

4.5.3 Crystal structure and phase transformation.

Figure 4.21 displays the XRD patterns of the as-deposited Pd(100 nm)/Ti(25 nm)/Pd(100 nm) multilayer stack; (a) on CP-Ti and (b) on Ti6Al4V alloy, plotted together with the annealed samples for one hour under pure H_2 gas at 550 ^oC on CP-Ti and on Ti6Al4V alloy. For comparison, the patterns of the Ti and Ti6Al4V substrates as-received are given on the figure.

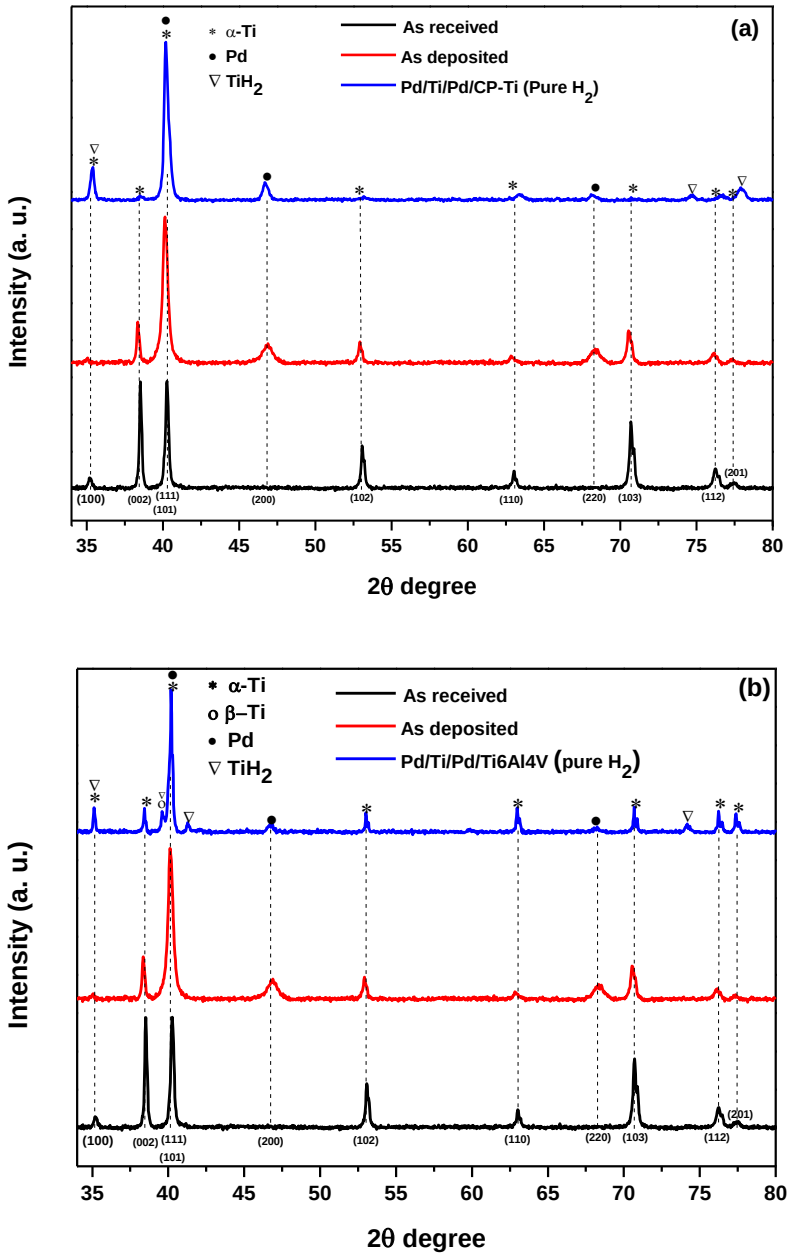

Figure 4.21: *XRD patterns of (a) as-received, as-deposited and annealed under pure H_2 atmosphere, on CP-Ti substrate; (b) those of as-received, as-deposited and annealed under pure H_2 atmosphere, on Ti6Al4V alloy substrate.*

As it was noted earlier in sections 4.2 and 4.3 when discussing XRD results, the as-received CP-Ti and Ti6Al4V alloy display peaks corresponding to the hexagonal α-Ti phase (pattern no: 00-044-1294) with lattice parameters a = 2.95 Å and c = 4.68 Å. An additional peak corresponding to β-Ti phase (pattern no: 00-044-1288) with lattice parameters a = 3.31 Å was observed in Ti6Al4V. The as-deposited samples in both systems show also, as expected, diffraction peaks corresponding to face-centered cubic (FCC) Pd (pattern no: 00-046-1043) with lattice parameters a = 3.89 Å.

However, upon annealing at 550 ^{o}C in the presence of pure H_2 gas, XRD spectra of system on both CP-Ti and Ti6Al4V alloy, showed the presence of Ti hydride, the face-centered cubic (FCC) TiH_2 (pattern no: 00-025-0982) with lattice parameters a = 4.45 Å. There was no observation of the Ti-Pd interdiffusion under pure H_2 annealing, indicating the stability of the catalyst layers up to a temperature of 550 ^{o}C. To further investigate the absence of the inter-diffusion, RBS was used.

4.5.4 RBS spectral analysis.

As mentioned earlier in section 4.2, the probed depth was 4.7 μm following SRIM simulations. Figure 4.22 shows RBS spectra of Pd(100 nm)/Ti(25 nm)/Pd(100 nm) multilayer stack on CP-Ti and on Ti6Al4V alloy for samples annealed under pure H_2 gas at 550 ^{o}C for one hour. The thickness of the deposited Pd films was simulated to be ~108 nm (surface layer) and ~110 nm (at the interface with the substrate). The sandwiched Ti thin film between the Pd layers was found to have reacted with oxygen with a stoichiometry of 80 at.% Ti and 20 at.% O. The simulated thickness shows disagreement with that obtained by the deposition quartz crystal monitor which recorded 103 nm on both Pd thin film. Curiously, the

buried Pd layer seems to be overestimated while the one on the surface seemed to be underestimated. The samples annealed under pure H_2 showed no intermixing of the films; thus, the RBS spectra will be similar in multilayer stacks for both substrates, so only the CP-Ti spectra are given as a typical example.

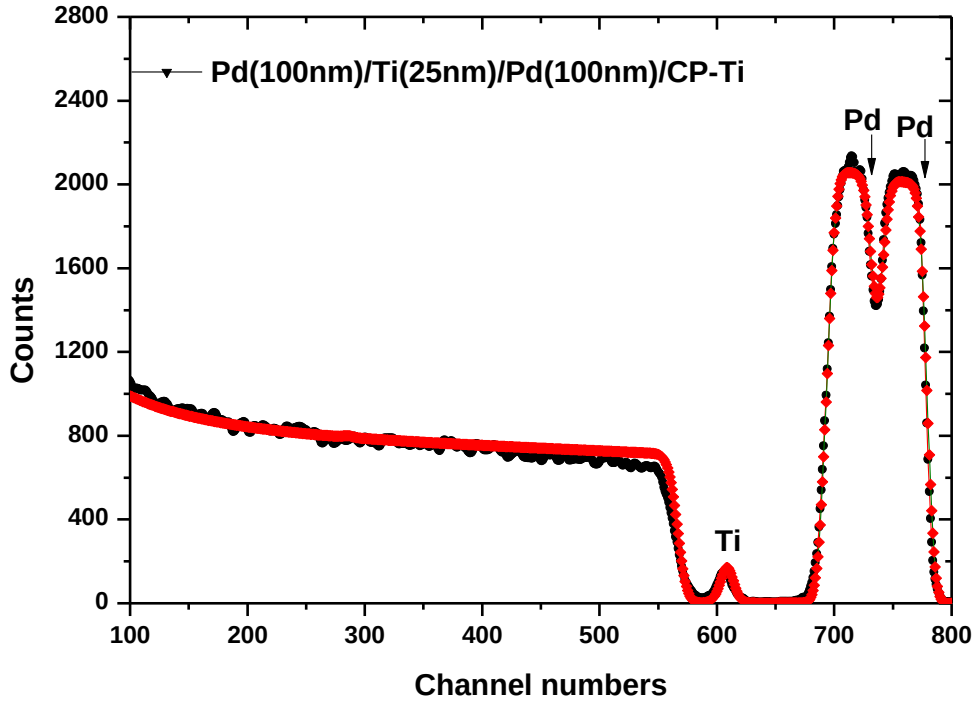

Figure 4.22: *RBS spectra of samples thermally annealed under pure H_2 at 550 ^oC for one hour on CP-Ti and on Ti6Al4V alloy substrates. Simulated spectra are also overlaid.*

Regardless of the thickness of the catalyst layer as seen from figure 4.22, no intermixing of layers was noted. It can be observed that the Pd layers were preserved upon annealing. This shows once more that the ambient under which the annealing process takes place, plays an important role on the thermal stability of the layers deposited. As it was highlighted before, the stability of the catalyst layer on H loading and release is essential for the system to be used efficiently in many cycles.

4.6 References

[4.1] E. Raub, E. Rǒschel. *Z Metallk*, 59, 112–4, (1968).

[4.2] P .Krautwasser, S. Bahn, K. Schubert, Structural investigations in systems Ti-Pd and Ti-Pt. *Zeitschrift fur Metallkunde*, 59 (9), 724–729, (1968).

[4.3] H. Okamoto, Pd-Ti (palladium-titanium). *Journal of phase equilibria*, 14, 128-129 (1993).

[4.4] V.N. Eremenko, T.D. Shtepa, Phase diagram of titanium–palladium system. *Poroshk. Metall*, (3), 75-81, (1972).

[4.5] J. L. Murray, the Pd-Ti (Palladium-Titanium) System, *Bulletin of alloy phase diagrams*, 3, 321-239, (1982).

[4.6] R.C. Bowman, A. Attalla Jr, G.C. Abell, J.S. Cantrell, A.J. Maeland, *Journal of the Less Common Metals*, 172–174:643 - 648, (1991).

[4.7] A. J. Maeland, G. G. Libowitz, Hydrogen absorption in some A_2B intermetallic compounds with the $MoSi_2$-type structure (C11b). Journal of the Less Common Metals, 74 (2), 295-300, (1980).

[4.8] N.P. Barradas, C. Jeynes, Advanced physics and algorithms in the IBA DataFurnace. Nuclear Instruments and Methods in Physics Research Section B: Beam Interactions with Materials and Atoms, 266 (8), 1875 - 1879, (2008).

[4.9] T.C. Tisone, J. Drobek, Diffusion in thin film Ti–Au, Ti–Pd, and Ti–Pt couples. *Journal of Vacuum Science and Technology*, 9 (1), 271-275, (1972).

[4.10] S. Mazwi, Hydrogen storage in Ti-based coatings and Ti6Al4V alloy, unpublished master's thesis, *university of the Western Cape*, Cape Town, South Africa, (2016).

[4.11] A. Lopez-Suarez, J Rickards, R. Trejo-Luna, Analysis of hydrogen absorption by Ti and Ti–6Al–4V using the ERDA technique. *International journal of hydrogen energy*, 28 (10), 1107-1113, (2003).

[4.12] Y. Baoguo, W. Yujie, Z. Yubin, G. Longqing, Hydrogenation Behaviour of Ti6Al4V Alloy, *Rare metal Materials and Engineering*, 46 (6), 1486-1490, (2017).

[4.13] F. Favier, E.C. Walter, M.P. Zach, T. Benter, R.M. Penner, . Hydrogen sensors and switches from electrodeposited palladium mesowire arrays. *Science*, 293, 2227-2231, (2001).

[4.14] E. Antolini, Palladium in fuel cell catalysis. *Energy & Environmental Science*, 2, 915-931, (2009).

[4.15] S.M. Tadayyon, Y. Fujimoto, K. Tanaka, M. Doi, M. Matsui, Solid-State Amorphization in Palladium/Titanium Multilayer Films during Sputter Deposition and Post deposition Annealing, *Japanese journal of applied physics,* 33, 4697-4702, (1994).

[4.16] Y. Fujimoto, S.M. Tadayyon, O. Yoshinari, K. Tanaka, Effect of hydriding on structural stability of Ni/Ti and Pd/Ti multilayers. *Materials Transactions*, 38 (9), 780-786, (1997.).

[4.17] M. Topić, S. Halindintwali, C. Mtshali, S. Nsengiyumva, Z.M. Khumalo, Hydrogen storage in Ti-based metal hydrides investigated by elastic recoil detection analysis (ERDA). *Nuclear Instruments and Methods in Physics Research Section B: Beam Interactions with Materials and Atoms*, 450, 239-243, (2019).

[4.18] Y. Fukai, The metal-hydrogen system: basic bulk properties (Vol. 21). *Springer Science & Business Media*, (2006).

[4.19] B.D. Adams, A. Chen, The role of palladium in a hydrogen economy. *Materials today*, 14 (6), 282-289, (2011).

[4.20] M. Topic, L. Pichon, S. Nsengiyumva, G. Favaro, M. Dubuisson, S. Halindintwali, S. Mazwi, J. Sibanyoni, C. Mtshali, K. Corin, The effect of surface oxidation on hydrogen absorption in Ti-6Al-4V alloy studied by elastic recoil detection (ERD), X-ray diffraction and nanohardness techniques. *Journal of Alloys and Compounds*, 740, 879-886, (2018).

[4.21] A. López-Suárez, Influence of surface roughness on consecutively hydrogen absorption cycles in Ti–6Al–4V alloy. *International journal of hydrogen energy*, 35 (19), 10404-10411, (2010).

[4.22] H. Shao, K. Asano, H. Enoki, E. Akiba, Correlation study between hydrogen absorption property and lattice structure of Mg-based BCC alloys. *International Journal of Hydrogen Energy*, 34 (5), 2312-2318, (2009).

[4.23] X.B. Yu, Z.X. Yang, H.K. Liu, D.M. Grant, G.S. Walker, The effect of a Ti-V-based BCC alloy as a catalyst on the hydrogen storage properties of MgH2. *International journal of hydrogen energy*, 35 (12), 6338-6344, (2010).

[4.24] S. Hofmann, M. Cantoro, B. Kleinsorge, C. Casiraghi, A. Parvez, J. Robertson and C. Ducati, Effects of catalyst film thickness on plasma-enhanced carbon nanotube growth, *Journal of applied physics*, 98, 034308, 1-8, (2005).

Summary and Conclusion

This study focussed on the use of Ti-Pd multilayer as a light metal system for hydrogen storage and the stability of the catalyst Pd layer under different atmospheres during hydrogenation. Pd/Ti/Pd system on CP-Ti and Ti6Al4V alloy substrates was studied; the thickness of the Pd layers was varied to investigate its effect on both the storage capacity and the stability of the system.

In the first part of this work, the thermal stability of the system at the chosen hydrogenation temperature (of 550 ^{o}C) was studied. For this purpose, the system was annealed in vacuum. While the multilayer system on both substrates showed a relatively smooth and uniform surface in the SEM, the annealed system under vacuum resulted in the formation of crystals as evidenced on the surface topology of the samples. XRD highlighted the formation of $PdTi_2$ phase upon annealing, suggesting thus the intermixing of deposited layers. RBS results are in agreement with XRD findings; indeed RBS spectra of the annealed samples showed clear intermixing of layers and the results of our simulations showed a stoichiometry of 33 at.% Pd and 67 at.% Ti which corresponds on the $PdTi_2$ phase observed by XRD. In- situ real-time RBS studies were conducted to monitor the inter-diffusion and intermixing of layers; it revealed that the yield of Pd starts to drop at 350 ^{o}C but clear intermixing of deposited layers was noted at around 550 ^{o}C; this was correlated to the findings of XRD where the metastable Pd_3Ti phase forms at ~350 ^{o}C and completely disappears at ~550 ^{o}C in favour of the stable $PdTi_2$ phase.

In the second part of the investigations, the studied multilayer system deposited on CP-Ti and Ti6Al4V alloy substrates was hydrogenated under the H_2 (15%) / Ar (85%) ambient and study the hydrogen storage capacity and the elemental diffusion between deposited layers. The second part of the thesis consisted in hydrogenating the studied multilayer systems deposited on both substrates at the chosen temperature of 550 ^{o}C; in addition to the Pd_2Ti

phase, the TiH_2 phase was also seen in XRD. The substrates used had no preferential influence in the elemental diffusion across different interfaces in the system. RBS spectra of the annealed samples showed intermixing of layers and the results of our simulations showed a stoichiometry of 65 at.% Pd and 35 at.% Ti which corresponds on the $PdTi_2$ phase observed by XRD. ERD studies, after hydrogenation in this ambient showed a substantial absorbed surface hydrogen but a relatively low hydrogen content stored in the multilayer system deposited on both substrates.

The third part of this work consisted in studying the effect of pure hydrogen gas ambient during hydrogenation on both the elemental diffusion across layers as well as the stored hydrogen profiles. The significant conclusion here is that the catalyst Pd layer was stable up to the 550 ^oC hydrogenation temperature; no Ti-Pd phase was observed upon hydrogenation under pure H_2 gas. Instead, TiH_2 phase was noted indicating the effective hydrogenation under the 100% H_2 atmosphere. There was no sign of Ti-Pd diffusion upon hydrogenation; saturation of TiH_2 available sites made the formation of this phase as a diffusion barrier against Pd atoms up to high temperatures. While the stored bulk H content under the H/Ar mixed gas was only under 10 at.%, the bulk H content under pure hydrogen hydrogenation was found to be around and higher than 20 at. % in the system deposited on CP and Ti alloy substrates respectively.

The last part of this thesis dealt with the effect of thickness of the catalyst layer on the hydrogen storage capacity by the system. In the layers stack, two thicknesses of the Pd layers were considered (50 nm and 100 nm) while keeping unchanged the thickness of the deposited Ti layer. It was noticed that by increasing the thickness of the catalyst, lower hydrogen content was absorbed in the system and this was found to be consistent regardless of the substrate the layer stack was deposited on. The surface catalytic activity increases then with the decrease of the thickness and moreover the dissociated hydrogen is swiped away quickly

in the storage material, decreasing thus the probability of recombination into molecular hydrogen.

Appendix

Table 5.1 and table 5.2 give a tabular summary of the crystallographic information of the different phases observed and the hydrogen content recorded in different Ti-Pd multilayer systems used respectively.

Table 5.1: *Crystallographic information of different phases observed.*

Phase	**Pattern no.**	**Lattice parameters**
HCP (α-Ti)	00-044-1294	a = 2.95 Å; c = 4.68 Å
BCC (β-Ti)	00-044-1288	a = 3.31 Å
FCC (Pd)	00-046-1043	a = 3.89 Å
BCT ($PdTi_2$)	00-010-0057	a = 3.09 Å; c = 10.054 Å
BCT (Pd_2Ti)	00-021-0610	a = 3.24 Å; c = 8.480 Å
FCC (TiH_2)	00-025-0982	a = 4.45 Å

Table 5.2: *Comparison of hydrogen storage capacity of the Ti-Pd multilayer systems.*

Samples	**H_2/Ar (sccm)**	**Temperature (^oC)**	**Time (hours)**	***Concentration (at.%H)***
Pd(50 nm)/Ti(25 nm)/Pd(50 nm)/ CP-Ti	100	550	2	*3.5*
Pd(50 nm)/Ti(25 nm)/Pd(50 nm)/ Ti6Al4V	100	550	2	*6.2*

Samples	H_2(100%) (sccm)	Temperature (^oC)	Time (hour)	*Concentration (at.%H)*
Pd(50 nm)/Ti(25 nm)/Pd(50 nm)/ CP-Ti	100	550	1	*19.5*
Pd(50 nm)/Ti(25 nm)/Pd(50 nm)/ Ti6Al4V	100	550	1	*25.7*
Pd(100 nm)/Ti(25 nm)/Pd(100 nm)/ CP-Ti	100	550	1	*12.5*
Pd(100 nm)/Ti(25 nm)/Pd(100 nm)/ Ti6Al4V	100	550	1	*11.2*

Future Outlook

This project forms part of a long term project in the investigation of materials for H_2 storage. There is still parts of the investigation that will be done in the near future. These include:

i. The impact of the hydrogenation time
ii. The effect the of gas flow rate
iii. The effect of the gas pressure
iv. The co-evaporation of Ti and the catalyst in a single thin film layer on top of different absorbing substrates.